POLITECNICO
MILANO 1863

SCUOLA DI INGEGNERIA INDUSTRIALE E DELL’INFORMAZIONE
Laurea Magistrale In Ingegneria Meccanica

Development of Downscaling Multiscale Analysis System by Finite Element Method for Peri-implant Bone Considering Collagen Fibers Using Micro-CT and SHG Images

Supervisors: Prof. Naoki Takano
Prof. Laura Vergani

Fu You
872099

Academic year 2018/2019

Master's Thesis Academic Year 2019

Development of Downscaling Multiscale Analysis System by Finite Element Method for Peri-implant Bone Considering Collagen Fibers Using Micro-CT and SHG Images

Fu You
(Student ID No.: 81723933)

Advisor Professor Naoki Takano

September 2019

Keio University
Graduate School of Science and Technology
School of Open and Environmental Systems

Abstract

Bone is an anisotropic material with a hierarchical structure, which consists of mineralized collagen fibers with biological apatite (BAp), water and protein at the nano-scale. A system of downscaling multiscale analysis by finite element method (FEM) based on micro-CT and second harmonic generation (SHG) images has been developed to study the strain distribution considering the collagen fiber in the human mandible near the dental implant under different loading conditions. Models in three scale are created. Macroscopic model is constructed based on the micro-CT images and two types of Dirichlet loading conditions are imposed to macroscopic model. Mesoscopic model is also based on micro-CT images to bridge the large gap in mesh size between macroscopic model and microscopic model. To maintain the continuity of problem setting, the collagen fibers are filled in the vacant space of the bone in the mesoscopic model. The microscopic models of collagen fiber structure as well as bone are based on SHG images. This is so far the first attempt to create a FEM model based on a combination of both micro-CT and SHG images. The microscopic results indicate that the high strain level occurs in the collagen-rich regions and the strain level is relatively lower in the fibrous region. Under two loading conditions, the compression direction is almost parallel to fiber orientation in ROI 3 in the fibrous region. However the connection between fiber orientation and loading direction is not clearly observed in the fibrous region in ROI 1 and ROI 2. Besides, the nonlinear analysis indicates that the geometrical nonlinear effects can be neglected.

Keywords: Bone; Collagen Fibers; SHG Images; Downscaling Multiscale Analysis; Micro-CT images; FEM

Sommario

Il tessuto osseo è un materiale anisotropo caratterizzato da una struttura gerarchica che consiste in fibre di collagene mineralizzate che su scala nanometrica sono composte da Apatite Biologica (BAp o idrossiapatite), acqua e proteine. Il lavoro si concentra sulla realizzazione di un modello che consenta di studiare la distribuzione delle deformazioni in una mandibola umana, sottoposta a diverse condizioni di carico, nella zona prossima a un impianto dentale. A questo proposito è stato sviluppato un codice che consenta una simulazione agli elementi finiti (FEM) delle deformazioni tramite un'analisi multi-scala del tessuto osseo che viene ricostruito basandosi su immagini micro-CT e SHG. Il modello è composto di tre diversi livelli. Il modello macroscopico è costruito sulla base di immagini micro-CT ed è sottoposto a due tipologie di condizioni di carico di Dirichlet. Il modello mesoscopico è anch'esso costruito sulla base di immagini micro-CT e, per mantenere la continuità delle condizioni del problema, è caratterizzato dal riempimento delle vacanze del tessuto osseo, artefatti derivanti dalle immagini, tramite fibre di collagene. Il modello microscopico della struttura delle fibre di collagene e dell'osso è basato su immagini SHG. Questo è il primo tentativo di creare un modello FEM bastato sulla combinazione di immagini micro-CT e SHG. I risultati microscopici indicano che elevati livelli di sforzo si concentrano delle zone ricche di collagene, mentre in quelle di matrice fibrosa presentano sforzi relativamente più bassi. Sottoposto a due condizioni di carico, il modello rivela una direzione di compressione quasi parallela all'orientamento delle fibre nella zona fibrosa ROI3, mentre nelle zone fibrose ROI1 e ROI2 non è chiaramente osservabile una connessione tra l'orientamento delle fibre e la direzione di carico. Inoltre, l'analisi non lineare mostra che gli effetti geometrici non lineari sono trascurabili.

Acknowledgement

I would first of all thank Professor Naoki Takano from Departmemt of Mechanical Engineering in Keio University for introducing me to the biomechanical research and offering guidance in the research. Also, I would like to Professor Satoru Matsunaga and Doctor Kento Odaka from the Department of Anatomy in Tokyo Dental College for taking the micro-CT images and SHG images and offering the medical knowledge. Besides, I would like to express my thanks to Professor Laura Vergani from Department of Mechanical Engineering in Politechnico di Milano for offering me the valuable guidance and comments on my thesis.

Contents

List of figures and tables

1 Introduction

1.1 Dental implant and osseointegration

Missing natural tooth can affect the patient’s way of chewing and speaking. More severely the lost tooth makes the nearby teeth to move from their previous position and increase the difficulty to clean the teeth. The lost tooth should be replaced by the dental implant immediately otherwise the remaining natural teeth can suffer from severe decaying problem in the long term. A dental implant is placed in the jawbone to support a dental prosthesis (Figure 1.1). A dental implant consists of the implant, abutment and dental prosthesis. The implant directly interacts with the bone of skull. After the dental implant is placed into the bone, osseointegration process happens, which creates a direct connection between living bone and a load-carrying endosseous implant at the light microscopic level [1].

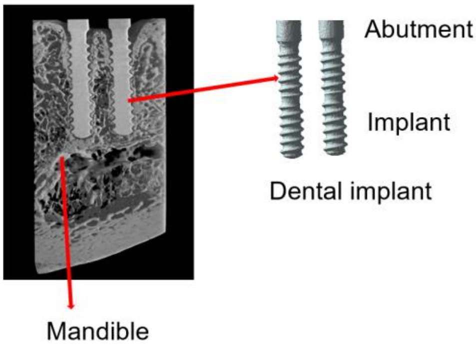

Figure 1.1 Dental implant in the mandible

Figure 1.2 shows the process of osseointegration [2]. In step 1, an implant bed is prepared through drilling surgery and the surgery causes the wound. In step 2, the implant is placed in the implant bed and the process of wound healing starts. In step 3, mesenchymal stem cells recruit on the surface of the implant, proliferate and differentiate into pre-osteoblast, which leads to osseointegration. In step 4, after a certain time, the wound is healed and the bone grows around the implant, which stabilizes the implant. The interface of the natural tooth and the bone is a group of specialized connective tissue fibers that essentially attach a tooth to the bone [3], which is different from the interface of bone and dental implant (Figure 1.3).

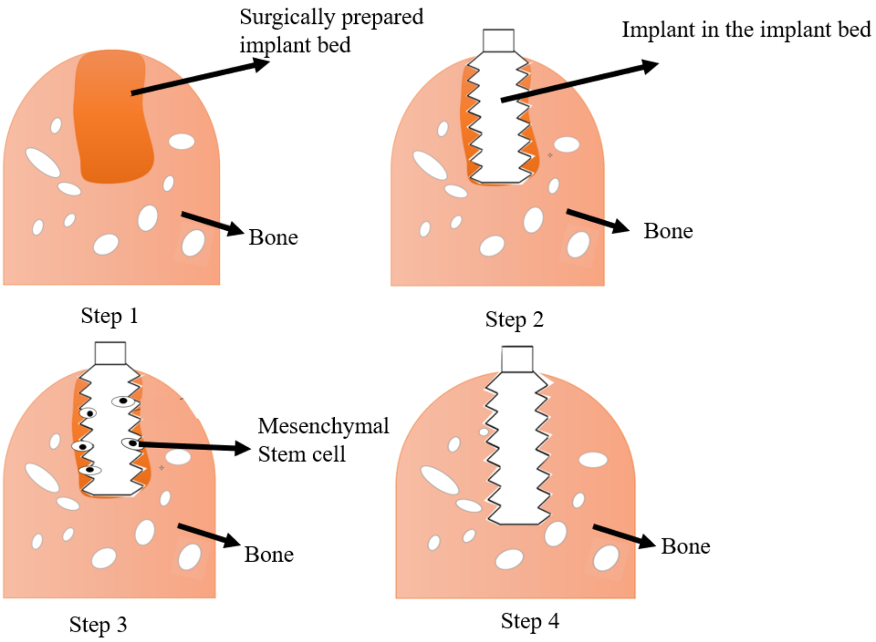

Figure 1.2 Steps of osseointegration

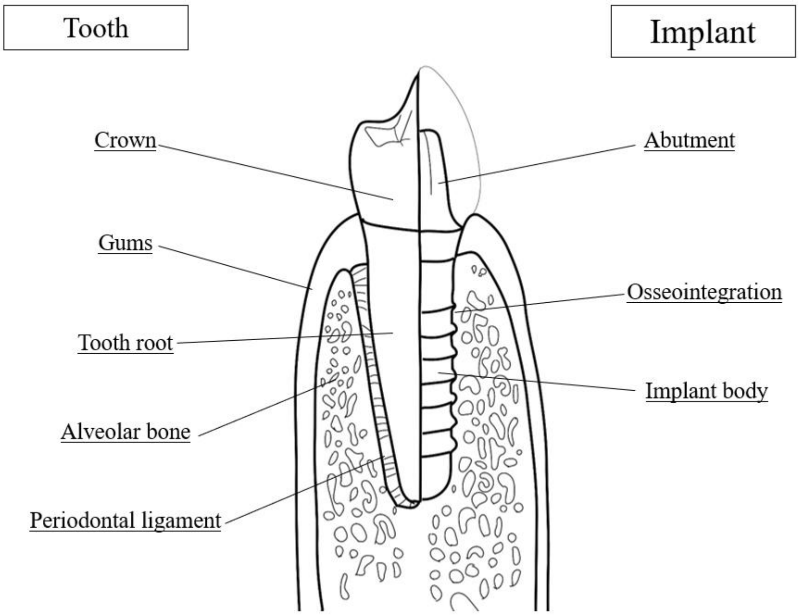

Figure 1.3 The tooth-bone interface and implant-bone interface

The nature of newly grown bone near the dental implant is not clearly known to dentists and this study attempted to study the mechanical behavior of the newly grown bone near the dental implant with the numerical approach based on FEM.

1.2 Hierarchical Structure of Bone

To study the mechanical behavior of the newly grown peri-implant bone, learning its hierarchical structure helps to model the bone and understand the simulation results. Bone has hierarchical structure at different length scales [4], which provides the bone with multiple mechanical capabilities, such as stiffness, weight-supporting and fracture resistance. To understand the anisotropy and inhomogeneity of the bone, it’s important to understand the architecture and mechanical properties at different scales [5].

Figure 1.4 shows the hierarchical structure of human’s mandible, which is the lower jaw bone of human skull. At the macroscale, the bone of mandible can be divided into two types of bone: the cortical bone which is compact and dense, and trabecular bone which is porous. The macroscale can be observed in the micro-CT images, whose resolution ranges from several micro-meters to hundreds micro-meters. At the microscale, osteons of cylinder shape with a blood vessel (Harversian cannel) in the center constitute of the cortical bone. The diameter of osteons ranges from 100μm to 500μm. At the sub-micro scale, layers of lamella are concentrically arranged around Harversian canal and each layer has an alternating direction of collagen fiber to form the osteon. The thickness of lamella ranges from 3μm to 8μm. At nanoscale, collagen fiber is of a cylinder shape, inside which are water, mineralized particles, protein and collagen fibrils arranged parallel to the axis of collagen fibers. The diameter of collagen fiber is smaller than 0.6μm. With micro meter resolution, SHG imaging technique allows to observe the collagen fibers, lamella layers and osteons. At sub-nano scale, inside each collagen fibril, collagen molecules are connected with crosslinks and arranged parallel to the axis of collagen fiber and plantlet biological apatites are distributed within the fibril.

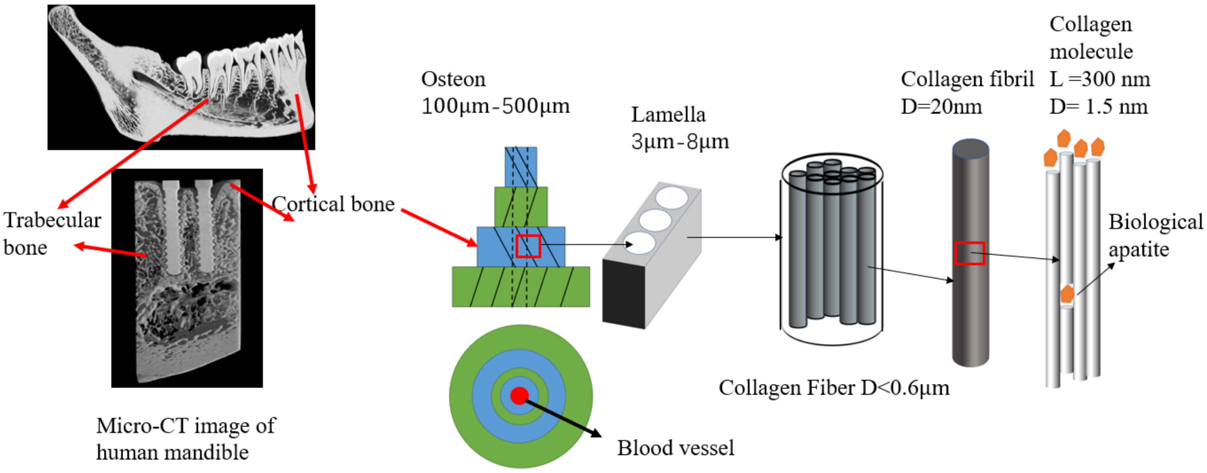

Figure 1.4 Hierarchical structure of the mandible

1.3 Purpose of this Study

According to the observation under SHG microscope, the newly grown bone near the dental implant is supposed to be the cortical bone because osteons with blood vessels can be observed. The arrangement of collagen fibers near the dental implant is different from the natural tooth. So the effect of the dental implant on the collagen fiber near the interface between bone and dental implant is of great interest to dentists. The collagen fiber at the interface zone between the living bone and the dental implants changes due to osseointegration process [6]. Circularly polarized light (CPL) and scanning electron microscopy (SEM) were used to investigate the density and orientation of the collagen fiber near the dental implants after loading [7]. Similarly, pigs were inserted dental implants and the behavior of collagen fibers is studied with SEM and profilometric analysis to compare the effects of different dental implants on the collagen fiber [8]. These researches studied the distribution of collagen fibers by observing different medical images using statistics.

There are also researches on the mechanical properties of collagen fiber. The elastic modulus of collagen fiber in bone is estimated by determining Debye–Waller factor through the diffracted X-ray intensity [9]. Direct homogenization procedure using the finite element method is used to estimate the elastic modulus of collagen fiber as a function of the volumetric mineral content [10].

However, no numerical approach has combined both micro-CT images and SHG images to study the nanostructure of the collagen fiber with the dental implants. To explore the correlation between the observed nanostructure of collagen fibers and strain distribution under different loading conditions, a semi-automatic system of downscaling multiscale analysis has been developed by the author to pass the result of micro-CT image-based model to the SHG image-based model. A mandible with two dental implants of a human cadaver is scanned with micro-CT, to which the loading condition is imposed. Meanwhile the collagen fibers near the implants are scanned with SHG imaging technique, whose resolution is about 100 times higher than the micro-CT images. Based on the image resolutions, the 3D structures of mandible with implants are created using micro-CT images. The 3D structure of collagen fibers is created using the stitched SHG images, in which three ROIs are extracted and used for analysis.

The purpose is to connect the model of mandible and collagen fiber with the downscaling multiscale analysis. The mesoscopic model is proposed to reduce the computational error because the gap in the resolution of mandible and collagen fiber is large. Also the mechanical behavior of collagen fibers will be studied when the implants in the mandible are subjected to different loads in the multiscale analysis. The semi-automatic system has been implemented in VOXELCON.

2 Literature Review

2.1 SHG histological studies

2.1.1 Mechanism of SHG

SHG is a powerful imaging technique in many biological studies. SHG relies on a nonlinear optical process in which two incident low energy photons with same frequency are combined to form a new photon with twice the incident frequency (Figure 2.1). It happens after the two incident photons interact with a nonlinear material. The nonlinear optical interaction can provide contrast and optical sectioning capability for high-resolution imaging [11].

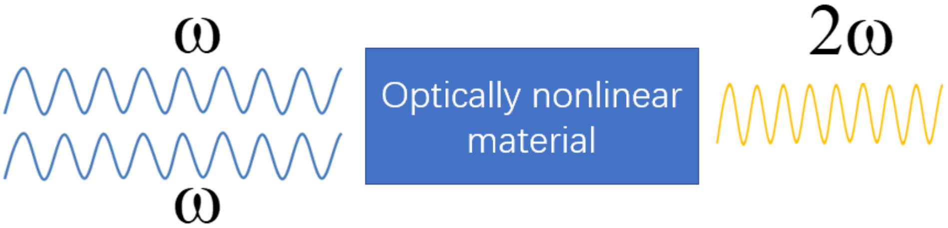

Figure 2.1 Nonlinear optical process of SHG

So far, there are a number of SHG microscopes in the market. Different SHG microscopes adopt different laser sources, optical path, detection geometry, and detection electronics to fully exploit SHG's contract mechanism [12]. An example of SHG microscope is shown in Figure 2.2. A multi-photon femto-second pulse laser is essential as an excitation source. The laser light passes an optical path to reach the sample and generate a SHG wave, which is reflected back to the photomultiplier tubers, where the SHG signals are analyzed to generate SHG images.

SHG imaging technique is an ideal tool to visualize tissues in situ with several advantages. Firstly photobleaching and phototoxicity can be greatly reduced because in SHG imaging process an induced polarization rather from absorption [12]. Also the wavelength of laser source is in the near infrared spectral range, high resolution, deep tissue imaging to depths of several hundred microns can be readily achieved [13]. Besides, SHG has high specificity for collagen, to enable quantitative scoring and the ability to distinguish between fibrillar and non fibrillar collagens [14]. And one of the main advantage of SHG microscope is its unique capability to provide 3D images of the organization of collagen fibers with micrometer resolution.

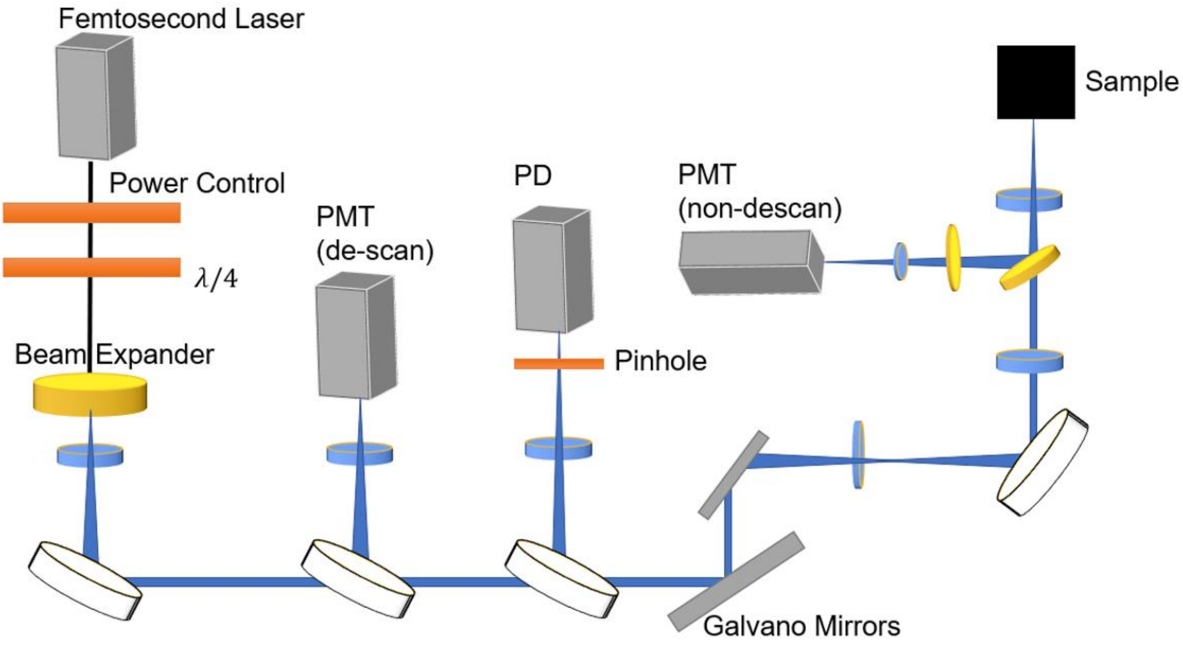

Figure 2.2 A schematic of SHG microscope. PMT: photomultiplier tuber; PD: photodetector

2.1.2 Histological application of SHG

With the advantageous features, SHG imaging technique has been widely used in histological application. By visualizing the collagen fibers in the tissues, new information about collagen fibers can be obtained to help medical researchers diagnose diseases and understand the role of collagen fibers in different tissues. The applications of SHG are introduced in the following.

SHG allows to observe the collagen fibers in both normal and disease state to understand the alternation caused by diseases. In the skin tissues, the morphology of collagen and elastin and their biochemical variations in skin tissue were analyzed by SHG [15]. Comparison of normal skin tissues and skin with scars was made to understand the pathophysiology of hypertrophic scars. In the cardiovascular tissues, SHG imaging has been performed to observe collagen structure inside an artery wall of healthy samples and region affected by atherosclerosis [16]. The observation indicates that a disorder of the organization in collagen is affected by the disease. Also, by observing the structure of collagen in tissues with SHG, the functions and capabilities of the collagen are explored. In the eye tissues, SHG imaging revealed that corneal collagen fibrils function as the transparency of cornea. Meanwhile scleral fibrils possess inhomogeneous, tube-like structures with thin hard shells, maintaining the high stiffness and elasticity of the sclera [17]. In the dental research, SHG is also used to investigate the structural characteristics of the human jawbone with the long - term implant and the location and direction of the osteon [18].

2.1.3 SHG apparatus in this study

In this study, the SHG images were acquired with a multiphoton confocal microscopy system (A1R+MP, Nikon, Japan) (Figure 2.3 and Figure 2.4) with an excitation laser (Mai Tai eHP, wavelengths: 690-1040 nm; repetition rate: 80 MHz; pulse width: 70 fs; Spectra-Physics, Tokyo, Japan) and a water-immersion objective lens (CFI75 Apo 25´W MP, numerical aperture: 1.1; Nikon, Tokyo, Japan). The excitation wavelength for the observation of collagen fibers was 880 nm. Image acquisition, processing for orthogonal views and cropping were performed using NIS-Elements version 4.0 (Nikon). The minimum dimension of the observed objective is about $350\mu\mathrm{m}$, which allows to observe osteons, lamellas and collagen fibers. The resolution of discrete SHG images is $0.83\mu\mathrm{m} \times 0.83\mu\mathrm{m} \times 20\mu\mathrm{m}$. The meaning of image resolution is as follows: one discrete SHG image consists of 1024×1024 pixels on the 2D plane and the area of each pixel is $0.83\mu\mathrm{m} \times 0.83\mu\mathrm{m}$ (Figure 2.5). The discrete SHG images are stacked in the normal direction of the 2D plane and the interval of two continuous images is $20\mu\mathrm{m}$ (Figure 2.6).

Figure 2.3 SHG system in this study (A1R+MP, Nikon, Japan)

Figure 2.4 Table of SHG apparatus

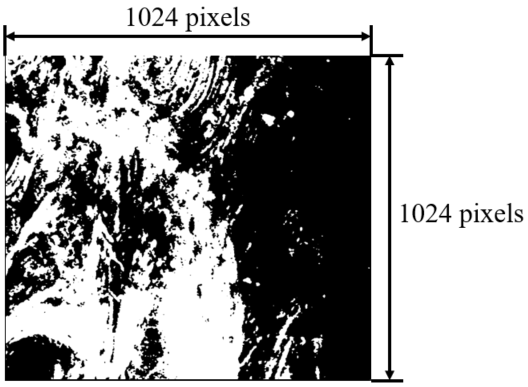

Figure 2.5 Pixel number of a discrete SHG image in this study

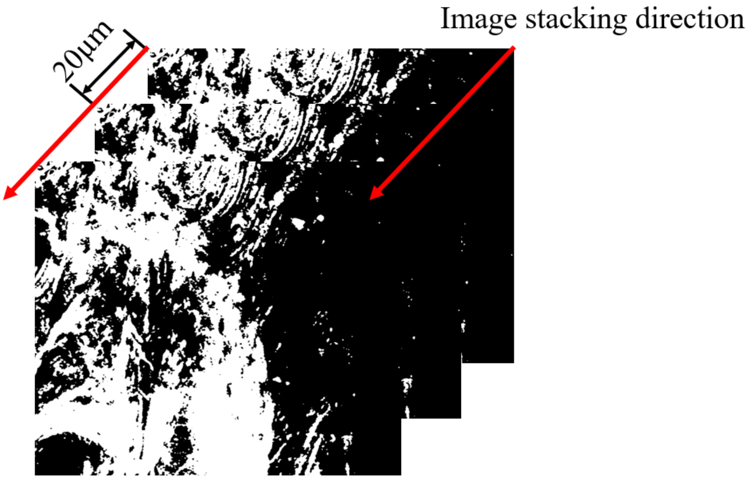

Figure 2.6 Image stacking of discrete SHG images to create 3D model

2.2 Micro-CT image-based FEM

2.2.1 Previous micro-CT image-based numerical studies

In the biomechanical researches, micro-CT images has been widely used to construct the three-dimensional structure of bone parts. Micro-CT images of 50μm resolution is used to construct the 3D structure of human mandible of a cadaver with two dental implants [19] (Figure 2.7). 3D FEM were performed to compute the peri-implant loading path of the trabecular bone near the implants and explore the correlation between the trabecular architecture and its biomechanical role. The bones of animal were also scanned by micro-CT images to study their functions. The maxilla of a young beagle dog after implant surgery was resected and imaged with micro-CT images of 50μm resolution [20] (Figure 2.8). 3D FEM model revealed that when the implant is under vertical loading, the trabecular bone functioned as a load buffer and bone trabeculae supporting load transfer from implants undergo remodeling.

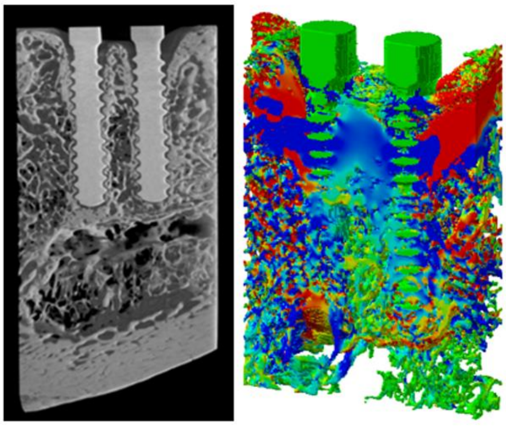

(a) Reconstructed structure of mandible with implants

(b) Loading path of FEM results

Figure 2.7 Modelling of human mandible with two dental implants based micro-CT image whose resolution is $50\mu\text{m}$

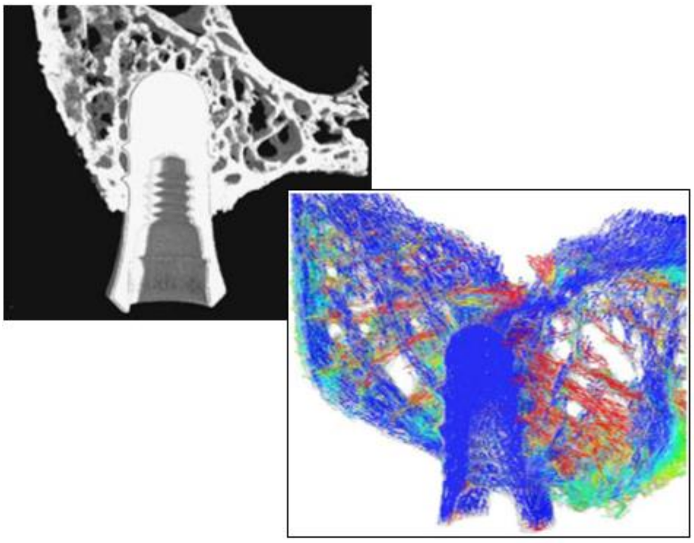

Figure 2.8 Load transfer path in the modelling of maxilla of beagle dog based micro-CT image whose resolution is $50\mu\text{m}$

2.2.2 Micro-CT imaging technique in this study

In this study, the specimen is a mandible with two screw-vent 4×10mm implants planted for 22 years. The mandible and two implants were scanned by micro-CT imaging technique separately (Figure 2.11), whose resolution is $90\mu\text{m} \times 90\mu\text{m} \times 50\mu\text{m}$. One micro-CT image consists of 1024×1024 pixels on the 2D plane in this study (Figure 2.9) and the area of each pixel is $90\mu\text{m} \times 90\mu\text{m}$.

The micro-CT images are stacked in the normal direction of the 2D plane and the interval of two continuous images is $50\mu\text{m}$ (Figure 2.10).

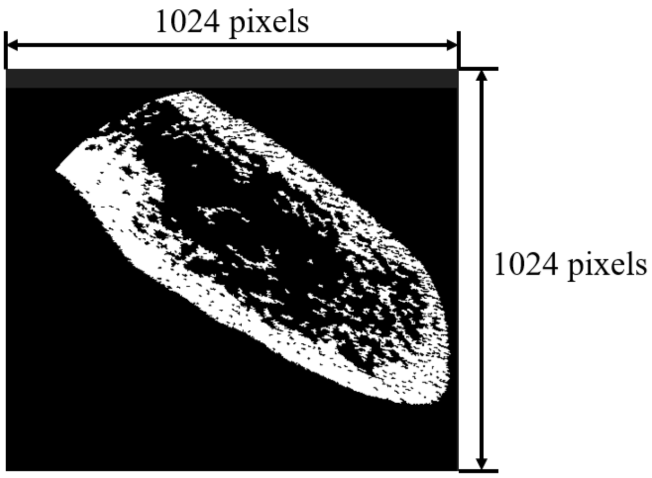

Figure 2.9 Pixel number of a micro-CT image in this study

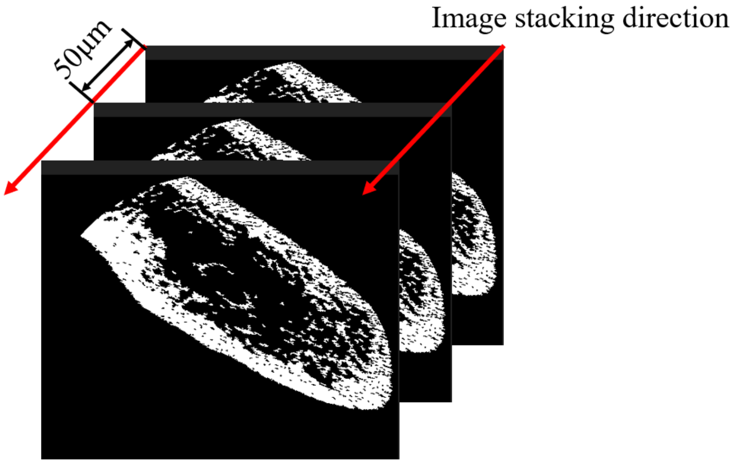

Figure 2.10 Image stacking of micro-CT images to create 3D model

In this study, each micro-CT image covers region of 45$\mathrm{mm}^2$and totally 512 images were obtained for both mandible and implants (Figure 2.11 (a) and (b)). In the micro-CT image of mandible, the white region represents the mandible and black region represents the empty space. Meanwhile, in the micro-CT images of dental implant, the white region represents the dental implant and the black region is the empty space. In this study, micro-CT images were also binarized with software of Image-J.

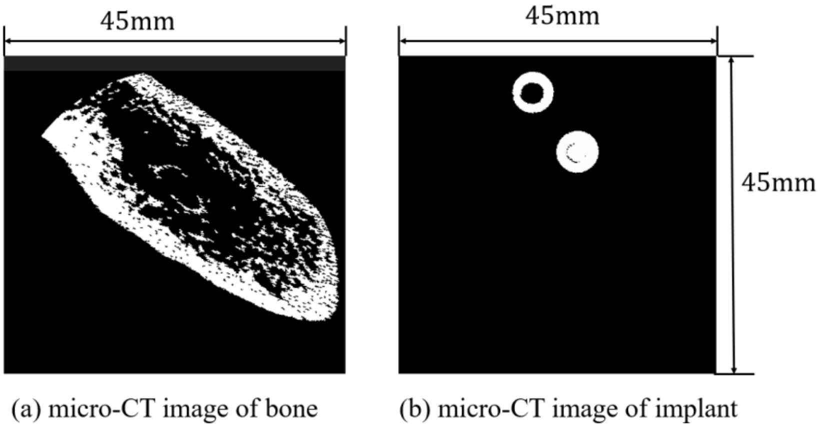

(a) micro-CT image of bone (b) micro-CT image of implant

Figure 2.11 Micro-CT image samples of bone and implant

2.3 Review of multiscale analysis

2.3.1 Homogenization method

Homogenization method is one typical upscaling method in the computational solid mechanics. The heterogeneous composite material is substituted with equivalent material model computed in the homogenized modelling. Based on the homogenization theory, attempt was made to determine the effective average elastic constants of linear elasticity of general composite materials by considering their microstructure[21]. The theory of homogenization method is introduced briefly as following.

Assume the whole domain Ω is a heterogenous composite material which consists of basic cell arranged periodically (Figure 2.12). The traction boundary is denoted as Γ_t. The macroscale and the microscale are defined a *X* and *Y* and the scaling ratio $\varepsilon = X/Y$. The microscopic equation (2.1) consider the periodic boundary condition of microscopic structure where *E* is the elastic tensor. And χ is a periodic function, called the characteristic displacement, which expresses the mismatch of the mechanical properties of the constituents and the geometrical configuration.

$$\int_Y E_{ijmn} \frac{\partial \chi_m^{kl}}{\partial y_n} \frac{\partial \delta u_i^1}{\partial y_i} dY = \int_Y E_{ijkl} \frac{\partial \delta u_i^1}{\partial y_j} dY \quad \forall \delta u_i^1 \tag{2.1}$$

The macroscopic elastic tensor can be computed in (2.2) based on (2.1).

$$E_{ijkl}^H = \frac{1}{|Y|} \int_Y (E_{ijkl} - E_{ijmn} \frac{\partial \chi_m^{kl}}{\partial y_n}) dY \tag{2.2}$$

where E^H is the homogenized maro-properties and *Y* is the region of microscale and $|Y|$ is the volume of microscale. Not only the macroscopic homogenized properties but also the microscopic mechanical behavior can be obtained. The microscopic stress σ can be computed in (2.3),

$$\sigma_{ij} = \left(E_{ijkl} - E_{ijmn} \frac{\partial \chi_m^{kl}}{\partial y_n} \right) e_{kl} = \left(E_{ijkl} - E_{ijmn} \frac{\partial \chi_m^{kl}}{\partial y_n} \right) (E_{klpq}^H)^{-1} \Sigma_{pq} \tag{2.3}$$

where e is the macroscopic strain and Σ is the macroscopic stress. The detailed formula deviation can be found in [22].

Homogenization method has been widely used in biomechanical research to compute the homogenized mechanical properties and microscopic stress. The structure of trabecular in the human lumbar vertebra was modelled based on micro-CT images and the macroscopic homogenized properties for healthy and osteoporotic bones were computed to make a comparison [23]. In the dental research, a homogenization material model of trabecular bone is used to recover the lost region due to the saw thickness of 0.3 mm [24]. Besides the application in biomechanical, homogenization method is also applied in 3D printing manufacturing. The homogenization method is used to predict the elastic mechanical properties of the carbon fiber-reinforced lamina [25], which were manufactured using an innovative process based on the fused filament fabrication and the result of computed mechanical properties matches the experiment measurement.

There is also limitation of homogenization method. If the heterogenous material is dispersed in the whole domain, homogenization method can work well by choosing a periodic cell. However, when the heterogenous material only exists in a small region in the whole structure, the homogenization method will fail to work because such a periodic cell is impossible to be chosen. In this case, mesh superposition [26] is adopted to solve this kind problem.

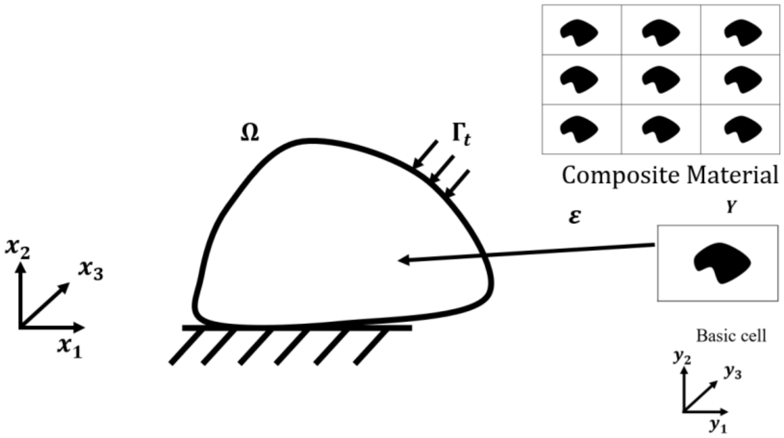

Figure 2.12 A two-scale problem

2.3.2 Mesh superposition method

Homogenization method is impossible to work on problems with respect to non-uniformity of macroscopic fields. And in this case, mesh superposition was developed to predict the microscopic stress with higher accuracy. Mesh superposition method is also a multiscale computational method, in which both macroscopic stress and microscopic stress can be computed.

The brief theory of mesh superposition is introduced as follows. In the Figure 2.13, the global domain and its boundary are defined as Ω^G and Γ^G. The boundary of Γ_t is subjected to the traction. In the local model, the domain and its boundary are defined as defined as Ω^L and Γ^L. The displacement vector {u} in the local domain Ω^L is defined in (2.4).

$$\{\mathrm{u}\} = \{u^G\} + \{u^L\} \tag{2.4}$$

where $\{u^G\}$ is the displacement vector in the global mesh and $\{u^L\}$ is the displacement vector in the local mesh. At the boundary Γ^{GL}, (2.5) has to be achieved to maintain the continuity of displacement.

$$\{u^L\} = 0 \tag{2.5}$$

The strain vector can be defined based on (2.4).

$$\{\varepsilon\} = [\mathrm{B}]\{\mathrm{u}\} = \begin{cases} [B^G]\{u^G\} + [B^L]\{u^L\} & \text{in } \Omega^L \\ [B^G]\{u^G\} & \text{in } \Omega^G \end{cases} \tag{2.6}$$

where [B] is the strain-displacement matrix. Then the governing equation can be summarized in (2.7):

$$\begin{bmatrix} [K^G] & [K^{GL}] \\ [K^{GL}]^L & [K^L] \end{bmatrix} \begin{Bmatrix} \{u^G\} \\ \{u^L\} \end{Bmatrix} = \begin{Bmatrix} \{f\} \\ \{0\} \end{Bmatrix} \tag{2.7}$$

where

$$[K^G] = \int_{\Omega^G} [B^G]^T\,[E^G][B^G]d\Omega + \int_{\Omega^L} [B^G]^T\,[E^L][B^G]d\Omega \tag{2.8}$$

$$[K^L] = \int_{\Omega^L} [B^L]^T\,[E^L][B^L]d\Omega \tag{2.9}$$

$$[K^{GL}] = \int_{\Omega^L} [B^G]^T\,[E^L][B^L]d\Omega \tag{2.10}$$

$$\{f\} = \int_{\Gamma_t} [N^G]^T\,\{t\}d\Gamma \tag{2.11}$$

Here $[K^G]$ and $[K^L]$ are the stiffness matrix with respect to the global mesh and local mesh. And $[K^{GL}]$ expresses the coupling of local mesh and global mesh. (2.7) can be solved to obtain the $\{u^G\}$ and $\{u^L\}$. The detailed formula deviation can be found in [22].

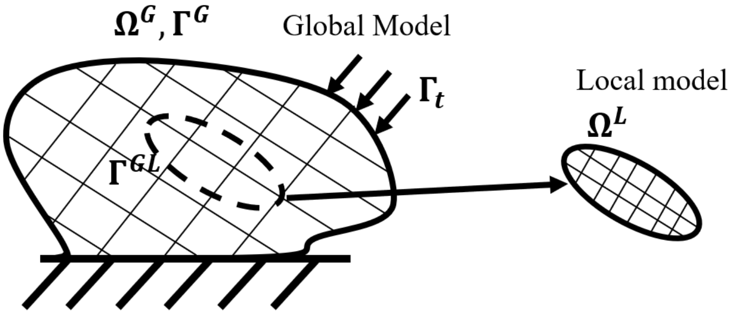

Figure 2.13 Definition of global model and local model

There are some applications of mesh superposition method. For example, mesh superposition method was used to compute the microscopic stress in the trabecular bone around acetabular cup implant in total hip arthroplasty under non-uniformity of macroscopic strain [27]. Attempt had been made to study crack propagation for large scale or complicated geometry structures using mesh superposition method [28]. Mesh superposition allows to study the effects of local heterogeneity on the global structure. However, in this study, only the mechanical behavior in the local structure is of interest so mesh superposition is not applied. Instead, downscaling multiscale analysis based on zooming method is applied to study the mechanical behavior of collagen fibers in the nanostructure. The mesh size of each scale will be introduced in Chapter 2.4.

3 Computational method and its implementation

In this study, downscaling multiscale analysis was executed to study the mechanical behavior of collagen fibers. The theory of the downscaling multiscale analysis and the implementation in the software VOXELCON are as follows.

3.1 *Theory of downscaling method*

3.1.1 Interpolation with shape function

In FEM, the continuous region is discretized with elements and the interpolation within the elements is achieved through shape function. Assume there is one voxel element (Figure 3.1). A local $\xi-\eta-\mu$ coordinate is created, whose origin point is placed at the center of the element. The length of each side is normalized. And the coordinate of each node is noted as ξ_i, η_i, μ_i and can be easily obtained (Table 3-1). The displacement in the ξ, η and μ directions of each node is already known as: u_i, v_i, w_i, where i=1,2,3⋯,7,8 . The red point is assumed to be a random point inside the element: ξ_0, η_0, μ_0. Its displacement is unknown: u_0, v_0, w_0.

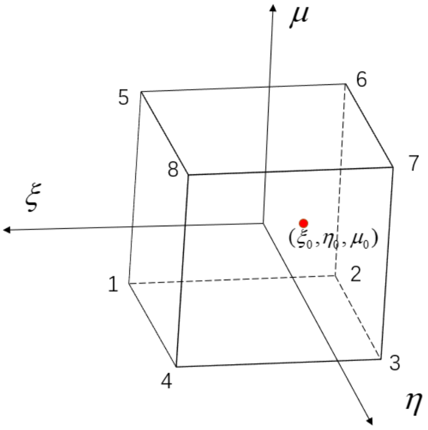

Figure 3.1 A voxel element

Table 3-1 Coordinate of each node

Node	Coordinate (ξ,η,μ)	Node	Coordinate (ξ,η,μ)
1	(1,-1,-1)	2	(-1,-1,-1)
3	(-1,1,-1)	4	(1,1,-1)
5	(1,-1,1)	6	(-1,-1,1)
7	(-1,1,1)	8	(1,1,1)

The eight shape functions are defined according to the coordinate of each node:

$$N_i=\left(\frac{\xi-\xi_{For\ node\ i,\ \xi-axis\ node}}{\xi_i-\xi_{For\ node\ i,\ \xi-axis\ node}}\right)\left(\frac{\eta-\eta_{For\ node\ i,\eta-axis\ node}}{\eta_i-\eta_{For\ node\ i,\eta-axis\ node}}\right)\left(\frac{\mu-\mu_{For\ node\ i,-axis\ node}}{\mu_i-\mu_{For\ node\ i,\eta-axis\ node}}\right) \tag{3.1}$$

To expand (3.1):

$$\begin{cases} N_1 = -\frac{1}{8}(\xi_1+\xi_0)(\eta_1+\eta_0)(\mu_1+\mu_0) = -\frac{1}{8}(1+\xi_0)(-1+\eta_0)(-1+\mu_0) \\ N_2 = -\frac{1}{8}(\xi_2+\xi_0)(\eta_2+\eta_0)(\mu_2+\mu_0) = -\frac{1}{8}(-1+\xi_0)(-1+\eta_0)(-1+\mu_0) \\ N_3 = -\frac{1}{8}(\xi_3+\xi_0)(\eta_3+\eta_0)(\mu_3+\mu_0) = -\frac{1}{8}(-1+\xi_0)(1+\eta_0)(-1+\mu_0) \\ N_4 = -\frac{1}{8}(\xi_4+\xi_0)(\eta_4+\eta_0)(\mu_4+\mu_0) = -\frac{1}{8}(1+\xi_0)(1+\eta_0)(-1+\mu_0) \\ N_5 = -\frac{1}{8}(\xi_5+\xi_0)(\eta_5+\eta_0)(\mu_5+\mu_0) = -\frac{1}{8}(1+\xi_0)(-1+\eta_0)(1+\mu_0) \\ N_6 = -\frac{1}{8}(\xi_6+\xi_0)(\eta_6+\eta_0)(\mu_6+\mu_0) = -\frac{1}{8}(-1+\xi_0)(-1+\eta_0)(1+\mu_0) \\ N_7 = -\frac{1}{8}(\xi_7+\xi_0)(\eta_7+\eta_0)(\mu_7+\mu_0) = -\frac{1}{8}(-1+\xi_0)(1+\eta_0)(1+\mu_0) \\ N_8 = -\frac{1}{8}(\xi_8+\xi_0)(\eta_8+\eta_0)(\mu_8+\mu_0) = -\frac{1}{8}(1+\xi_0)(1+\eta_0)(1+\mu_0) \end{cases} \tag{3.2}$$

And the interpolated displacement can be computed using the shape function:

$$\begin{cases} u_0 = u_1N_1 + u_2N_2 + u_3N_3 + u_4N_4 + u_5N_5 + u_6N_6 + u_7N_7 + u_8N_8 \\ v_0 = v_1N_1 + v_2N_2 + v_3N_3 + v_4N_4 + v_5N_5 + v_6N_6 + v_7N_7 + v_8N_8 \\ w_0 = w_1N_1 + w_2N_2 + w_3N_3 + w_4N_4 + w_5N_5 + w_6N_6 + w_7N_7 + w_8N_8 \end{cases} \tag{3.3}$$

(3.3) can be written in the matrix form:

$$\begin{Bmatrix} u_0 \\ v_0 \\ w_0 \end{Bmatrix} = \begin{bmatrix} N_1 & 0 & 0 & N_2 & 0 & 0 & \cdots \\ 0 & N_1 & 0 & 0 & N_2 & 0 & \cdots \\ 0 & 0 & N_1 & 0 & 0 & N_2 & \cdots \end{bmatrix} \begin{Bmatrix} u_1 \\ v_1 \\ w_1 \\ u_2 \\ v_2 \\ w_2 \\ \vdots \end{Bmatrix} \tag{3.4}$$

For simplicity, (3.4) can be written as:

$$\{d_0\} = [N]\{\bar{d}\} \tag{3.5}$$

Where $\{d_0\}$ is the interpolated displacement vector of the unknown point; $\{\bar{d}\}$ is the displacement vector of the nodes of one element; $[N]$ is the shape function matrix. In this way, the displacement of any point inside an element can be obtained.

In the multiscale analysis, the solution in the global mesh is interpolated in this way to create the boundary condition for the local mesh. Because VOXELCON doesn't have the interpolation capability, the interpolation process is achieved in python code and the result is imported into VOXELCON automatically afterwards also in python code.

3.1.2 Theory of the downscaling multiscale method

The concept of global model and local model was firstly introduced in the zooming method [29]. The basic procedure of zooming method is that an approximate solution is firstly computed over the entire region with the coarse global mesh. Then a zoomed region is separated from the entire region and meshed with finer local mesh. The boundary condition of local mesh utilized the results of global analysis. The accuracy and efficiency were tested in ([29] and [30]).

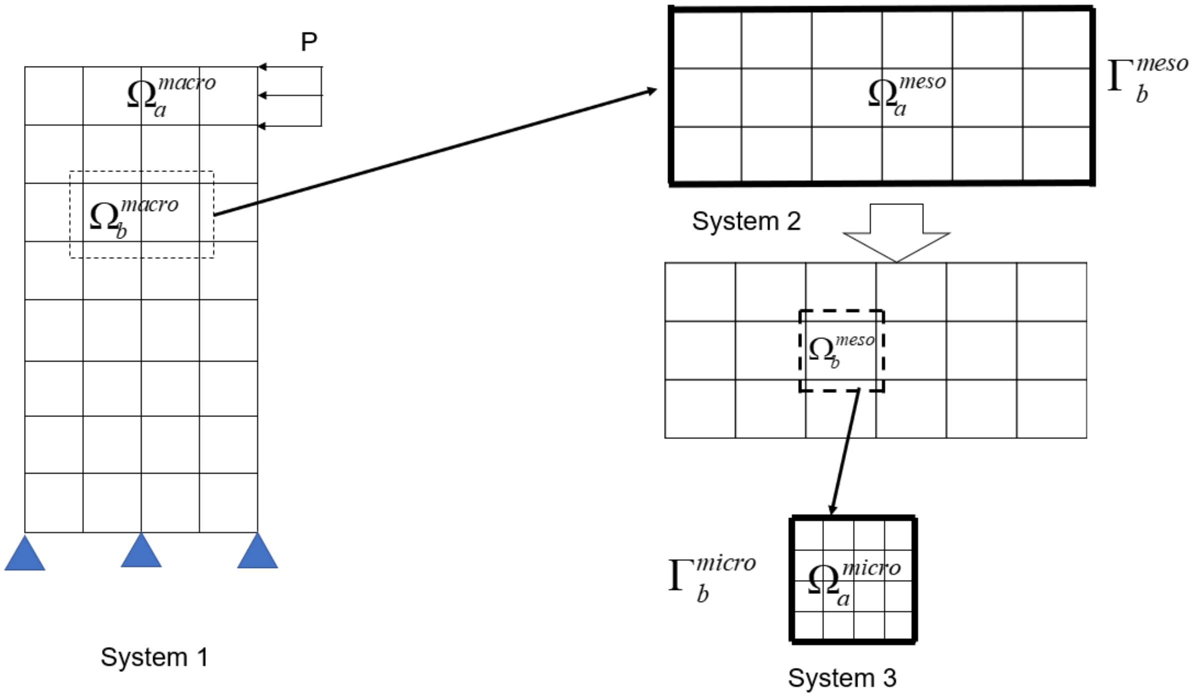

Figure 3.2 Zooming method in the three-scale problem. System 1: the macroscopic model; System 2: the mesoscopic model; System 3: the microscopic model

In this case, the problem is assumed to be three-scale: macroscale, mesoscale and microscale (Figure 3.2). Γ represents the boundary of the model and Ω represents the region. $\{u^{macro}\}$, $[K^{macro}]$ and $\{F^{macro}\}$ are defined to be the displacement vector, stiffness matrix and loading vector of the macroscopic model. Partition all the nodes in the macroscale into two sets, $\{u_a^{macro}\}$ which has n_a^{macro} nodes outside the mesoscopic region, $\{u_b^{macro}\}$ which has n_b^{macro} nodes inside the mesoscopic region. The total number of the nodes in the macroscale is n^{macro}, which is the summation of n_a^{macro} and n_b^{macro}.

The displacement equation for system 1 is:

$$[K^1]\{u^1\} = \{F^1\} \tag{3.6}$$

Where $\{u^1\} = \{u^{macro}\}$, $[K^1] = [K^{macro}]$ and $\{F^1\} = \{F^{macro}\}$.

Expand (3.6) we obtain:

$$\begin{bmatrix} K_{aa}^{macro} & K_{ab}^{macro} \\ K_{ba}^{macro} & K_{bb}^{macro} \end{bmatrix} \begin{bmatrix} u_a^{macro} \\ u_b^{macro} \end{bmatrix} = \begin{Bmatrix} F_a^{macro} \\ F_b^{macro} \end{Bmatrix} \tag{3.7}$$

The displacement equation for the system 2 includes both the nodes of macroscopic and mesoscopic model:

$$[K^2]\{u^2\} = \{F^2\} \tag{3.8}$$

or

$$\begin{bmatrix} K_{aa}^{meso} & K_{ab}^{meso} \\ K_{ba}^{meso} & K_{bb}^{meso} \end{bmatrix} \begin{Bmatrix} u_a^{meso} \\ \bar{u}_b^{meso} \end{Bmatrix} = \begin{Bmatrix} 0 \\ f_b^{meso} \end{Bmatrix} \tag{3.9}$$

Where $\{f_b^{meso}\}$ is the unknown reaction force on the boundary; $\{\bar{u}_b^{meso}\}$ is the displacement vector on the boundary (Γ_b^{meso}); $\{u_a^{meso}\}$ is the displacement vector of nodes in the rest of region of mesoscopic model (Ω_a^{meso}). $\{\bar{u}_b^{meso}\}$ can be computed by interpolating the macroscopic displacement using (3.5):

$$\{\bar{u}_b^{meso}\} = [N]_{meso}\{u_b^{macro}\} \tag{3.10}$$

$\{u_a^{meso}\}$ can be solved:

$$[K_{aa}^{meso}]\{u_a^{meso}\} + [K_{ab}^{meso}]\{\bar{u}_b^{meso}\} = 0 \tag{3.11}$$

From (3.11) we can compute:

$$\{u_a^{meso}\} = -[K_{aa}^{meso}]^{-1}[K_{ab}^{meso}]\{\bar{u}_b^{meso}\} \tag{3.12}$$

Then the result of mesoscopic model is obtained.

Now isolate the mesoscopic model and the system 3 is obtained, whose displacement equation is:

$$[K^3]\{u^3\} = \{F^3\} \tag{3.13}$$

or

$$\begin{bmatrix} K_{aa}^{micro} & K_{ab}^{micro} \\ K_{ba}^{micro} & K_{bb}^{micro} \end{bmatrix} \begin{Bmatrix} u_a^{micro} \\ \bar{u}_b^{micro} \end{Bmatrix} = \begin{Bmatrix} 0 \\ f_b^{micro} \end{Bmatrix} \tag{3.14}$$

Where $\{\bar{u}_b^{micro}\}$ can be computed by interpolation in the same way as (3.10):

$$\{\bar{u}_b^{micro}\} = [N]_{micro}\{u_b^{meso}\} \tag{3.15}$$

And $\{u_a^{micro}\}$ can be computed by substituting (3.15) into (3.14):

$$\{u_a^{micro}\} = -[K_{aa}^{micro}]^{-1}[K_{ab}^{micro}]\{\bar{u}_b^{micro}\} = -[K_{aa}^{micro}]^{-1}[K_{ab}^{micro}][N]_{micro}\{u_b^{meso}\} \tag{3.16}$$

After the microscopic displacement vector is solved, the strain and stress in the microscopic mesh can be easily solved:

$$\{\varepsilon\}_{micro} = [B]\{u_a^{micro}\} \tag{3.17}$$

$$\{\sigma\}_{micro} = [D]\{\varepsilon\}_{micro} \tag{3.18}$$

Where $\{\varepsilon\}$ is the microscopic strain and $\{\sigma\}_{micro}$ is the microscopic stress. $[B]$ is the strain-displacement matrix and $[D]$ is the elastic matrix.

In our problem, models in three scales will be created. Specified Boundary Method (SBM) is one application of zooming method [31] and adopted in our three-scale problem. The procedure is described as follows:

(1) Create macroscopic, mesoscopic and microscopic mesh based on different images.

(2) Impose boundary condition to macroscopic model and compute its solution.

(3) Output the displacement of the macroscopic model and process it with linear interpolation. The interpolation process is achieved through python code. Impose the interpolated displacement on the boundary of mesoscopic mesh and compute the solution.

(4) Repeat outputting the displacement of the mesoscopic model, interpolating and imposing the interpolated displacement to the microscopic model.

There are criterions when selecting the mesoscopic ROI to reduce the errors. Firstly, the center of the mesoscopic model should be close to the position of microscopic model because it had been tested that the numerical errors in the region closer to center were usually smaller than the surface. Secondly, try to include as many nodes on the boundary as possible to increase the accuracy of interpolation.

3.2 Development of the analysis system

3.2.1 Implementation of mesoscopic analysis

VOXELCON doesn’t have the function to do interpolation. Moreover the interpolated displacement has to be assigned to the nodes at the boundary of mesoscopic model node by node manually. However, there are more than 60,000 nodes at the boundary if the volume of mesoscopic model is 1 mm^3, which is a huge work for human labor. Therefore, a system is developed to achieve the interpolation and set-up of boundary condition automatically to avoid human errors and reduce time cost. The principle of the system is to create command lines for VOXELCON to execute a series of operations. This system is written in python code.

The system of mesoscopic model is developed to be almost automatic with only some inputs so that the user can easily use the system for analysis. The flowchart of development of mesoscopic model is shown in Figure 3.3. After running Meso.py, the program will ask users to manually input the directory of micro-CT images of the mandible, installation directory of VOXELCON, coordinate of the ROI and the directory of macroscopic displacement obtained in macroscopic model. After gaining all the required inputs, multitask will be executed and eventually a VOXELCON mesh file will be created, which includes the boundary condition of interpolated displacement. The mesoscopic results can be obtained by clicking ‘running simulation’ in VOXELCON.

The multitasks includes the following subsequent sub-tasks:

1 Creating isotropic material models of bone and collagen fibers in VOXELCON.

2 Constructing the 3D model of the mandible. With the directory of micro-CT images, the images can be automatically imported into VOXELCON to create the 3D model. The image resolution is set to be a parameter in the program.

3 Extracting the mesoscopic ROI from the mandible according to the input data of position of the ROI and the length of each side. The ROI is a cube whose side length is L_R. Assume the global coordinate of the ROI origin is (x_R, y_R, z_R). Then all the nodes whose coordinates are within the range of $(x_R \le x \le x_R + L_R, y_R \le y \le y_R + L_R, z_R \le z \le z_R + L_R)$ are selected to create the unmeshed mesoscopic model.

4 Filling the vacant space of the bone in the mesoscopic model with fiber material. The bone structure is porous. By filling the vacant space to make the mesoscopic

model a complete solid, the interpolation accuracy for the microscopic model will be increased.

5 Remeshing both the bone and collagen fiber together with finer elements to create the mesoscopic mesh. The mesh size is 0.009mm as shown in Table 4-1.

6 Extract the coordinate of nodes and elements at the boundary of the mesoscopic model. The coordinate of the nodes at the boundary (x_b^i, y_b^i, z_b^i) should meet any one requirement in (3.19):

$$\begin{cases} x_b^i = x_R \; or \; x_b^i = x_R + L_R & (1) \\ y_b^i = y_R \; or \; y_b^i = y_R + L_R & (2) \\ z_b^i = z_R \; or \; z_b^i = z_R + L_R & (3) \end{cases} \tag{3.19}$$

7 Extracting result data from the macroscopic model

8 Interpolation based on the coordinate of nodes and elements and result data of macroscopic model to obtain the boundary condition of prescribed displacement for the mesoscopic model. The theory of interpolation is introduced in 3.1.1.

9 Assign the interpolated displacement to the nodes at the boundary of mesoscopic model.

10 Save the file of the mesoscopic mesh with boundary condition settled.

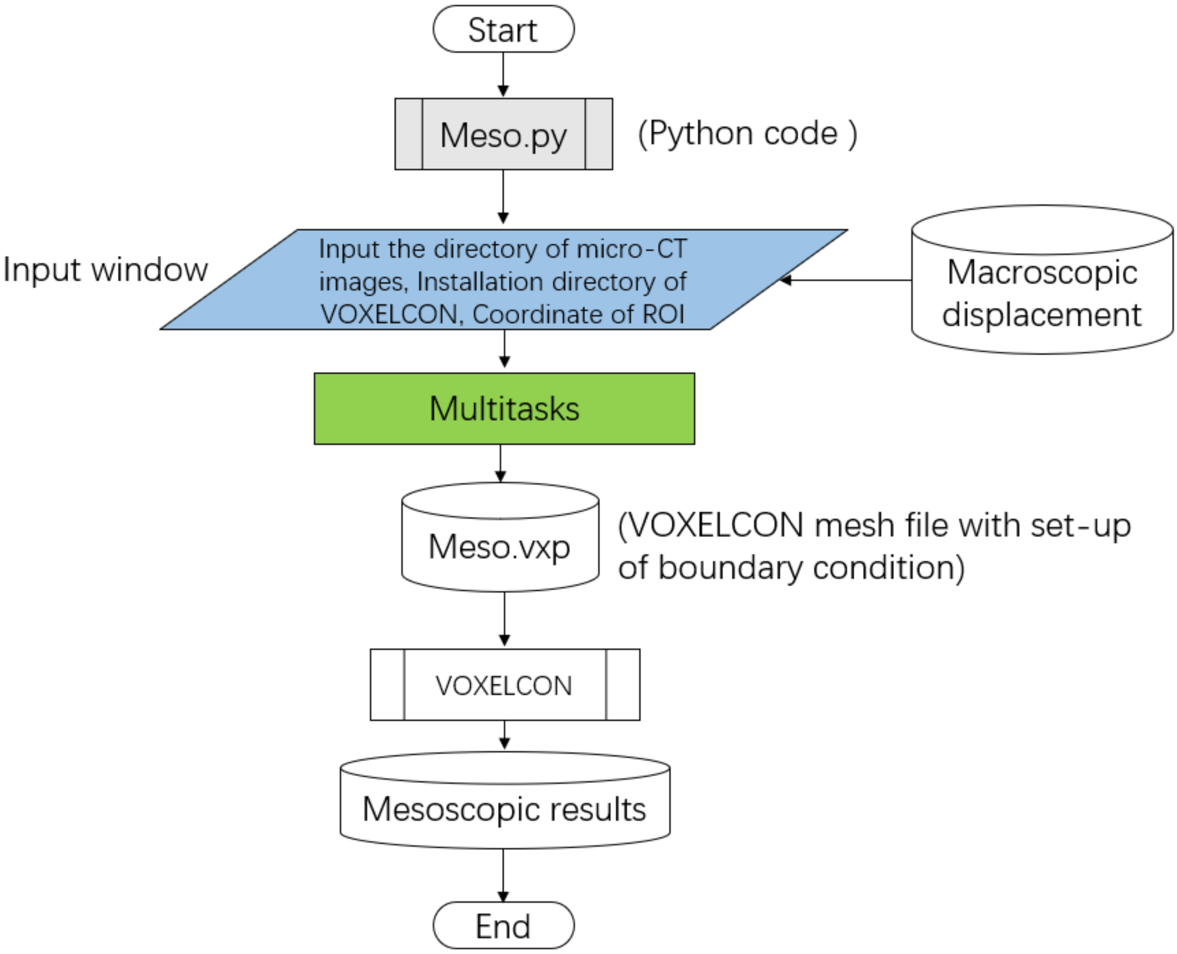

Figure 3.3 Flowchart of mesoscopic system

3.2.2 Implementation of microscopic system

The flowchart of microscopic system is shown in Figure 3.4. There are two python codes executed subsequently to obtain the microscopic results. The microscopic system is designed to be semi-automatic because the procedure to match the stitched model with macroscopic model is impossible to achieve automatically. After matching the stitched SHG image-based model with the macroscopic model, the global coordinate of the microscopic model can be output and used for interpolation.

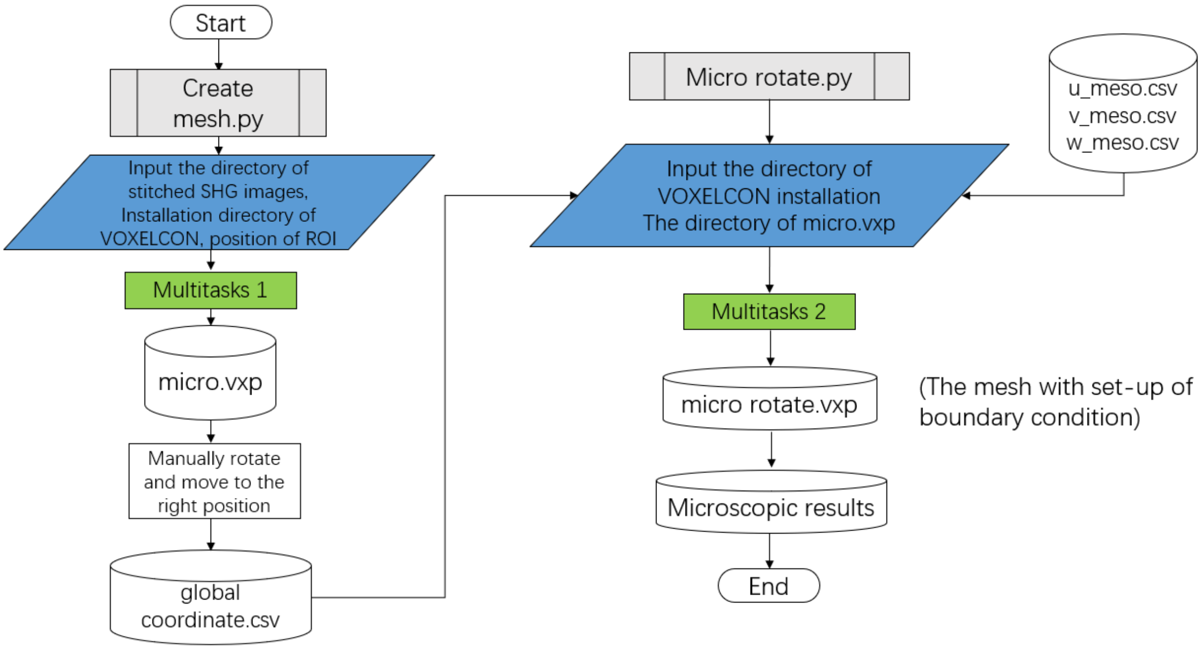

Figure 3.4 Flowchart of microscopic system

In the python code of Create mesh.py, firstly it asks the user to manually input the directory of stitched SHG images, installation directory of VOXELCON and coordinate of the ROI. Then the multitasks 1 is executed, which includes the following subsequent sub-tasks:

1 Creating isotropic material models of bone and collagen fibers in VOXELCON.

2 Constructing the complete 3D model from the stitched SHG images. The image resolution is set to be a parameter in the program.

3 Extract the ROI according to the input coordinate of the ROI from the complete 3D model and create the mesh of collagen fibers and assign the fiber material model to the mesh. The complete 3D model is remained.

4 Filling the vacant space in the ROI with bone material and mesh the bone and fibers together. The microscopic mesh is obtained after this step.

5 Save the microscopic mesh file and name it as ‘micro.vxp’.

After creating the microscopic mesh, we need to manually rotate and move the complete 3D stitched model to match it with the macroscopic model. The implant bed is used as the reference system for the matching. After matching the complete model, the global coordinate of the microscopic mesh is output, which is used in Micro rotate.py. In the Micro rotate.py, the user has to manually input the global coordinate data, directory of VOXELCON installation, the directory of micro.vxp (the mesh file format in VOXELCON) and the mesoscopic results of displacement.

Then the multitasks 2 is executed, which includes the following subsequent sub-tasks:

1 Extract the displacement from the mesoscopic results (u_meso.csv, v_meso.csv, w_meso.csv) and the global coordinate of all the nodes and elements.

2 Select all the nodes at the boundary of microscopic model and also extract their global coordinates.

3 Interpolation based on the global coordinate and result data of mesoscopic model to obtain the boundary condition of prescribed displacement for the microscopic model.

4 Assign the prescribed displacement to nodes at the boundary.

5 Save the microscopic mesh with boundary condition settled

The microscopic model with set-up of boundary condition (micro rotate) after the multitasks 2, with which the microscopic results can be obtained by click ‘running simulation’ in the microscopic model.

3.3 Verification of the downscaling analysis

3.3.1 Characteristics of VOXELCON

Zooming method is achieved in VOXELCON by python code developed by the author. VOXELCON is a powerful FEM Japanese commercial software from Quint company. VOXELCON has the following characteristics. For its advantages, this software is powerful to reconstruct the 3D structure from a large number of medical images and it can create a large number of elements (more than 10,000,000). However it also has some disadvantages. VOXELCON can only create voxel elements of the same mesh size in one study, so the zig-zag mesh is unavoidable. Meanwhile, only linear analysis can be achieved in VOXELCON. Besides, different material properties can’t be assigned to individual element, which inhibits the possibility to model the anisotropic material properties of collagen fibers.

VOXELCON is used in this study and multiscale system is implemented in this software. Considering the characteristics of this software, the verification is necessary.

3.3.2 Set-up of the Verification Example

One important parameter in the zooming method is the scaling ratio. Between two adjacent scales, large errors can occur if the scaling ratio exceeds the threshold. And in the multiscale analysis introduced in next chapter, the largest scaling ratio is 10, which is tested in this verification example.

Considering the mesh type of VOXELCON, the verification of zooming method in this software is necessary. And one simple verification example is tested for the zooming method and shown as follows.

Figure 3.5 shows a plate with a hole, whose diameter is *a* and much smaller than the dimension of the plate. The plate is subjected to uniaxial load of *s*. According to the analytical solution, the stress concentration occurs at point *A* and the stress concentration factor is 3.

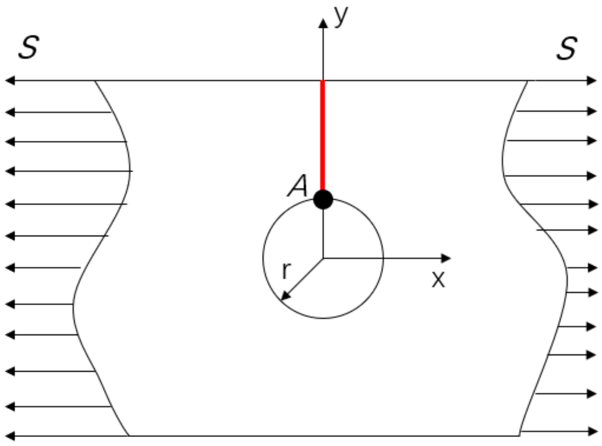

Analytical solution of $\frac{\sigma_x}{s}$ along x=0, $y \geq r$ (red path):

$$\frac{\sigma_x}{s} = 1 + \frac{1}{2}\left(\frac{r^2}{y^2} + \frac{3r^4}{y^4}\right)$$

Where $y \geq r$

Figure 3.5 Plate with a hole subjected to uniaxial load

The case in Figure 3.5 is simulated in VOXELCON and the accuracy of zooming method is tested. A rectangle plate with a small hole in the center is under uniaxial loading *s* at both ends (Figure 3.6 (a)). To reduce computational cost, only 1/8 of the plate is analyzed utilizing the symmetry of the plate (Figure 3.6 (b)).

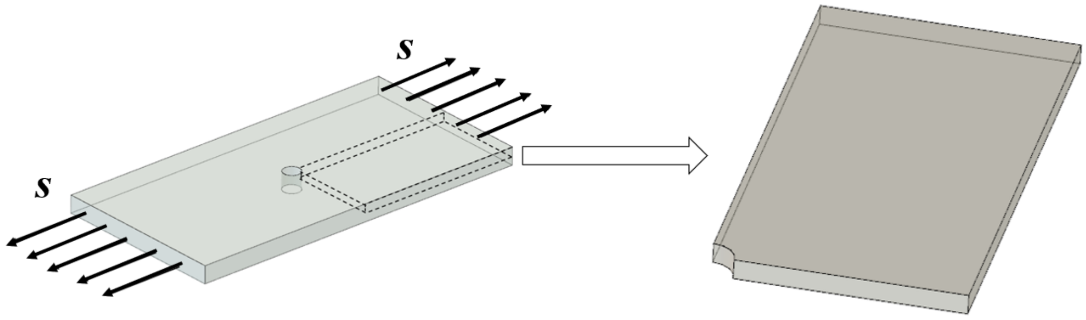

(a) A complete plate

(b) 1/8 of the plate

Figure 3.6 A rectangular plate with a hole under uniaxial loading. (a) a complete plate; (b)1/8 of the plate

The modelling of the 1/8 in VOXELCON is introduced as follows. Two macro models and one micro model will be created. For both macro model 1 and macro model 2, the plate size, hole size and boundary condition are the same (Figure 3.7 and Figure 3.8). The 1/8 of plate has length of 200 mm, width of 100 mm and thickness of 2 mm and it includes 1/4 of the hole. The radius of the hole is 10 mm. The boundary conditions of macro model 1 and 2 take advantages of geometrical symmetry of the plate: the movement in x direction of green surface, the movement in y direction of red surface and the movement in z direction of blue surface are constrained. However the mesh size of macro model 1 is 2 mm while the mesh size of macro model 2 is 0.2 mm. So the scaling ratio is set to be 10 in this case.

The micro model is a zoomed region of macro model 1. Its size is $20\text{mm} \times 20\text{mm} \times 2\text{mm}$ with 1/4 of hole at one corner. It’s meshed with elements the same as macro model 2, which is 10 times smaller than the macro model 1. All the plane surfaces on the boundary are imposed with boundary condition of interpolated displacement obtained from macro model 1 and the curve surface is subjected to no boundary condition. The stress concentration factors at the stress concentration point will be compared among the two macro models, micro model and the analytical solution.

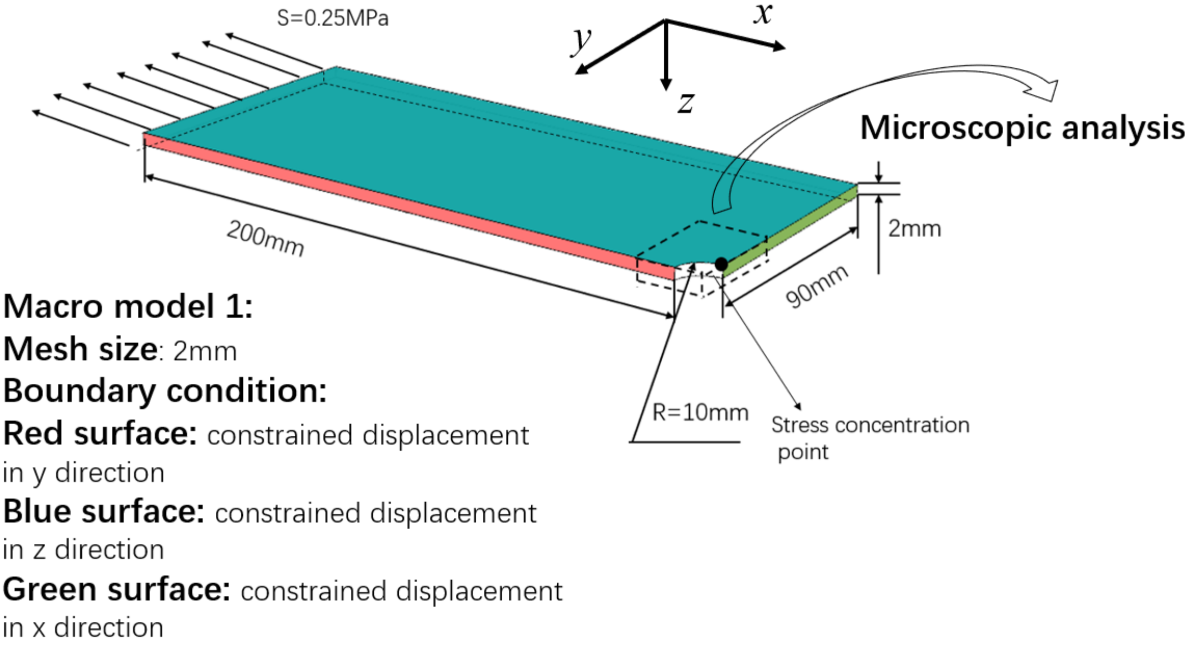

Figure 3.7 Setup of macro model 1

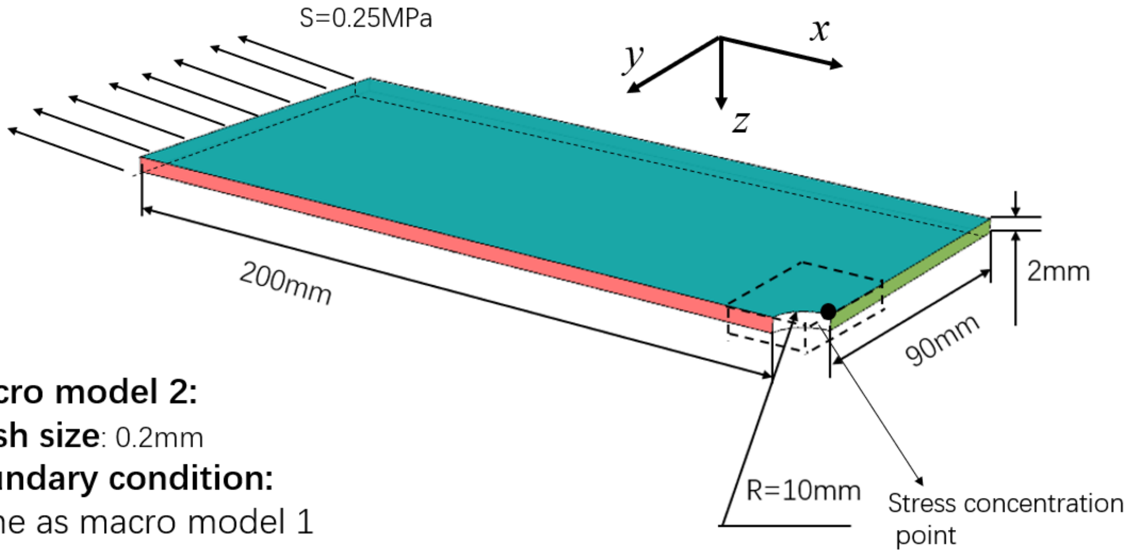

Macro model 2:
Mesh size: 0.2mm
Boundary condition:
Same as macro model 1

Figure 3.8 Setup of macro model 2

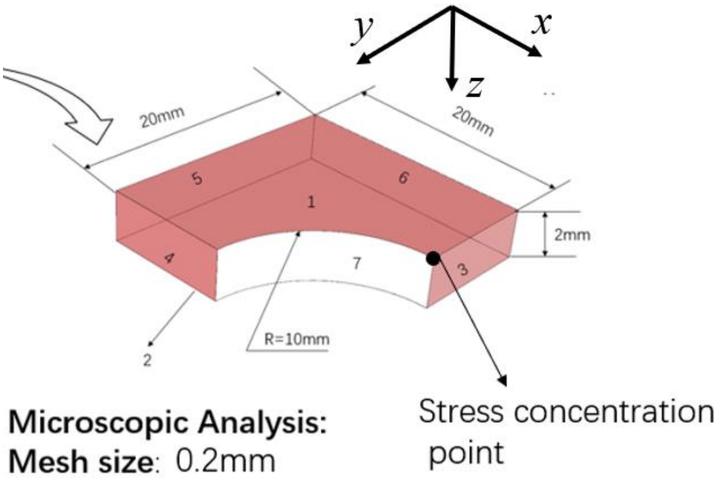

Microscopic Analysis:
Mesh size: 0.2mm
Boundary condition:
Surface 1-6: interpolated displacement
Surface 7: Free surface

Figure 3.9 Setup of micro model

4 Multiscale modelling of mandibular bone with dental implant

4.1 SHG image stitching technique

In this study, image stitching technique of SHG images is achieved. Each discrete SHG images allows to only observe a small region ranging from $0.5\mathrm{mm}^2$ to $1\mathrm{mm}^2$ depending on the image resolution. Locating the 3D structure based on such discrete SHG images is inaccurate without a reference system. Therefore image-stitching technique (Figure 4.1) is applied. each discrete image (Figure 4.1 (a)) covers region of $0.83\mathrm{mm}^2$. In the horizontal direction, 17 discrete images were stitched and in the vertical direction, 19 discrete images were stitched (Figure 4.1 (b)). The original image stitching process is automatically accomplished in the imaging process instead of postprocessing after obtaining all the discrete images. In the image postprocessing process, the original stitched is binarized (Figure 4.1 (c)) in the open-source software Image-J, after which the binarized image can be used in FEM modeling. After binarization, there are only two types of pixels in the image: white pixels and black pixels. The white region represents the collagen fibers and the black region is the bone.

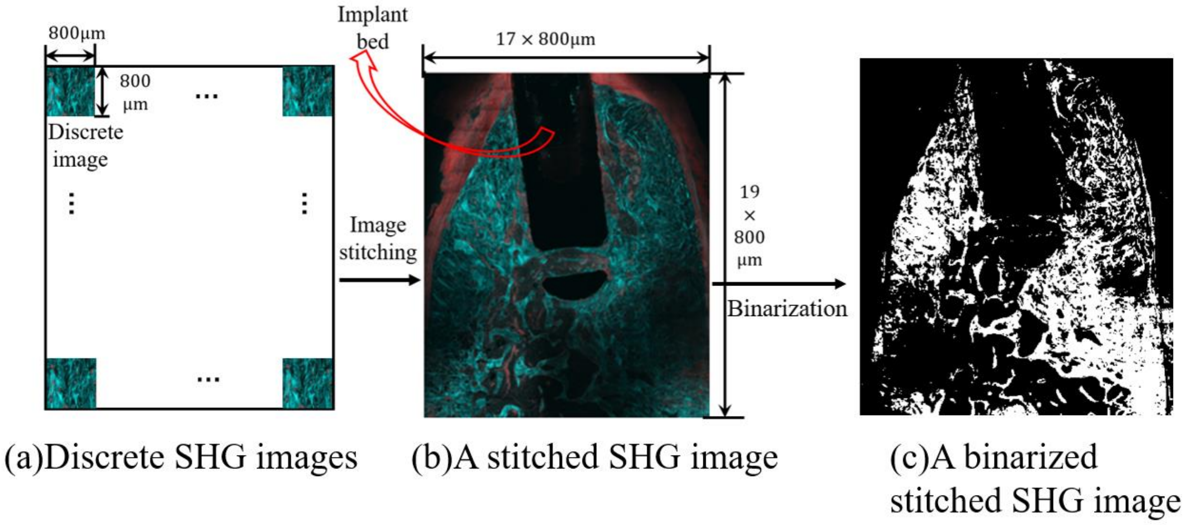

(a)Discrete SHG images (b)A stitched SHG image (c)A binarized stitched SHG image

Figure 4.1 Process to obtain a stitched SHG image

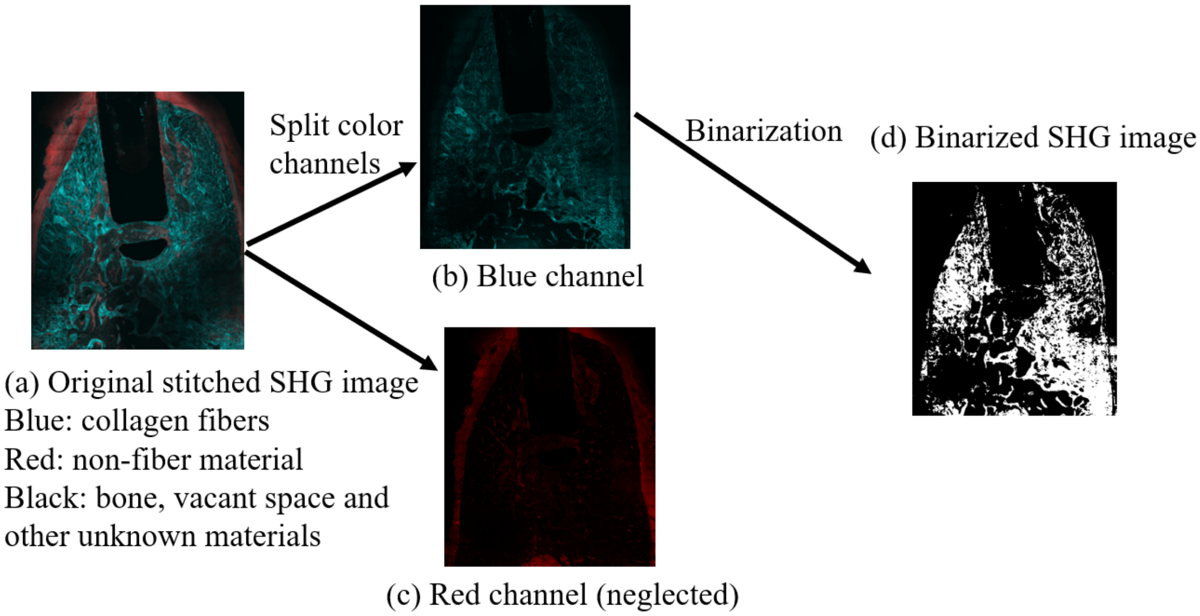

(a) Original stitched SHG image
Blue: collagen fibers
Red: non-fiber material
Black: bone, vacant space and
other unknown materials

(b) Blue channel

(c) Red channel (neglected)

(d) Binarized SHG image

Figure 4.2 Image binarization process

The SHG image binarization process is also important to understand the problem setting (Figure 4.2). In the original stitched SHG image, the whole structure of the bone near the implant can be seen. And three colours can be seen in the original image. The blue region is the collagen fibers and the red region represents the non-fibers material, such as water, protein. And the black region includes bone, vacant space and other unknown materials. We used image-postprocessing technique to split the colour channels so that we can extract images with only the collagen fiber. We neglect the red channel in our modelling to simplify the problem setting and we binarized only the blue channel. After binarization in the modelling, the white region is assigned with fiber material and all the black region is all assumed to be bone.

With the stitched SHG images, the implant bed can be used as the reference system to locate the region of interest (ROI) for analysis. One stitched SHG image consists of 323 discrete images and only five stitched images were obtained due to the large imaging time. Each stitched image covers area of $200\mathrm{mm}^2$. Totally, five stitched images were obtained. As for the imaging time, imaging each discrete SHG image takes 10 second and totally it takes 4.5 hours to obtain the five stitched images. The resolution in the image-stacking direction is about 25 times lower than the two other directions because obtaining one stitched image is highly time-consuming and saving the stitched image requires large amount of memory.

4.2 Meshing size and number in this study

In this downscaling multiscale analysis, models in three scale will be created: macroscopic model based on micro-CT images, mesoscopic model based on the same micro-CT images and microscopic model based on stitched SHG images.

Table 4-1 presents the meshing strategy and approximated number of elements for each model to estimate the computational cost. The scaling ratio of mesh size between macroscopic model and microscopic model is 45, which is large and can cause large errors. So the mesoscopic model is created to bridge the large gap in the mesh size between macroscopic and microscopic model. All these three models are meshed with only voxel elements and analyzed in the VOXELCON. The theory of the downscaling multiscale analysis will be introduced in Chapter 3 and the detailed modelling of the three-scale models will be introduced in Chapter 4.

Table 4-1 Meshing strategy of the three-scale analysis

	Resolution	**Mesh size**	**Volume**	**#Elements**	**Material**
Macroscopic	$0.09 \times 0.09 \times 0.05mm$	$0.09 \times 0.09 \times 0.09mm$	$4500mm^3$	**6,000,000**	Bone & impalnt
Mesoscopic	$0.09 \times 0.09 \times 0.05mm$	$0.009 \times 0.009 \times 0.009mm$	$1mm^3$	**1,300,000**	Bone & fibers
Microscopic	$0.0083 \times 0.0083 \times 0.02mm$	$0.002 \times 0.002 \times 0.002mm$	$0.05mm^3$	**6,000,000**	Bone & fibers

In this study, FEM models in three scales are constructed (Figure 4.3). The total volume of the macroscopic model is about 4500 mm^3 and the mesh size is 0.09mm (Figure 4.3 (a)). The mesoscopic model is a bone region of 1 mm^3 extracted from the macroscopic model, whose mesh size is 0.009mm (Figure 4.3 (b)). The microscopic model ranges from 0.015 mm^3 to 0.025 mm^3 due to some SHG images are not continuous and abandoned to use. And microscopic mesh size is 0.002mm (Figure 4.3 (c)).

Macroscopic model constructed with micro-CT images contains the mandible and implants. While the stress and strain distribution of collagen fibers are analyzed in the microscopic model based on the stitched SHG images. Because the scaling ratio between the resolution of macroscopic model and microscopic model depends on the image resolution of micro-CT images and SHG images. In this case, the scaling ratio in image resolution is 100 and the scaling ratio between the mesh size of microscopic model and macroscopic model is 45, which can cause large errors after testing. So, a mesoscopic model based on the same micro-CT images as the macroscopic model is introduced to bridge the gap in the image resolution and mesh size, which contains both collagen fibers and bone. The collagen fibers are included in the mesoscopic model to ensure the continuity of problem setting between mesoscopic model and microscopic model. The detailed model construction method is in this chapter.

Figure 4.4 shows the number of cases in the three scale. In the macroscopic model, two cases are computed, which includes two types of loading conditions. And for the mesoscopic analysis, three ROIs are computed for each macroscopic case and there are 6 mesoscopic cases in total. For the microscopic case, one ROI is computed for each mesoscopic case and there are 6 microscopic cases in total.

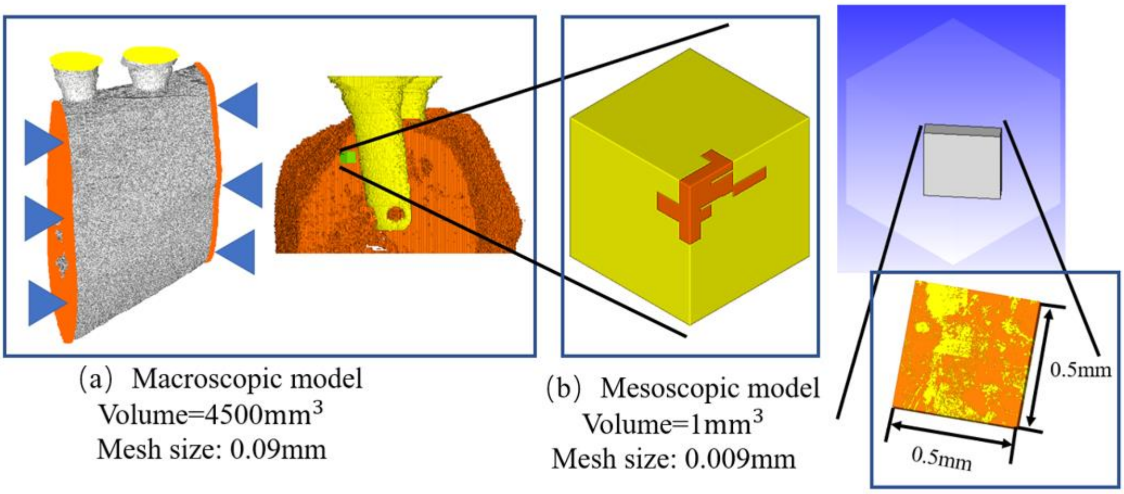

(a) Macroscopic model
Volume=4500mm^3
Mesh size: 0.09mm

(b) Mesoscopic model
Volume=1mm^3
Mesh size: 0.009mm

(c) Microscopic model
Volume: 0.015~0.025mm^3
Mesh size: 0.002mm

Figure 4.3 Volume and mesh size of the three-scale models

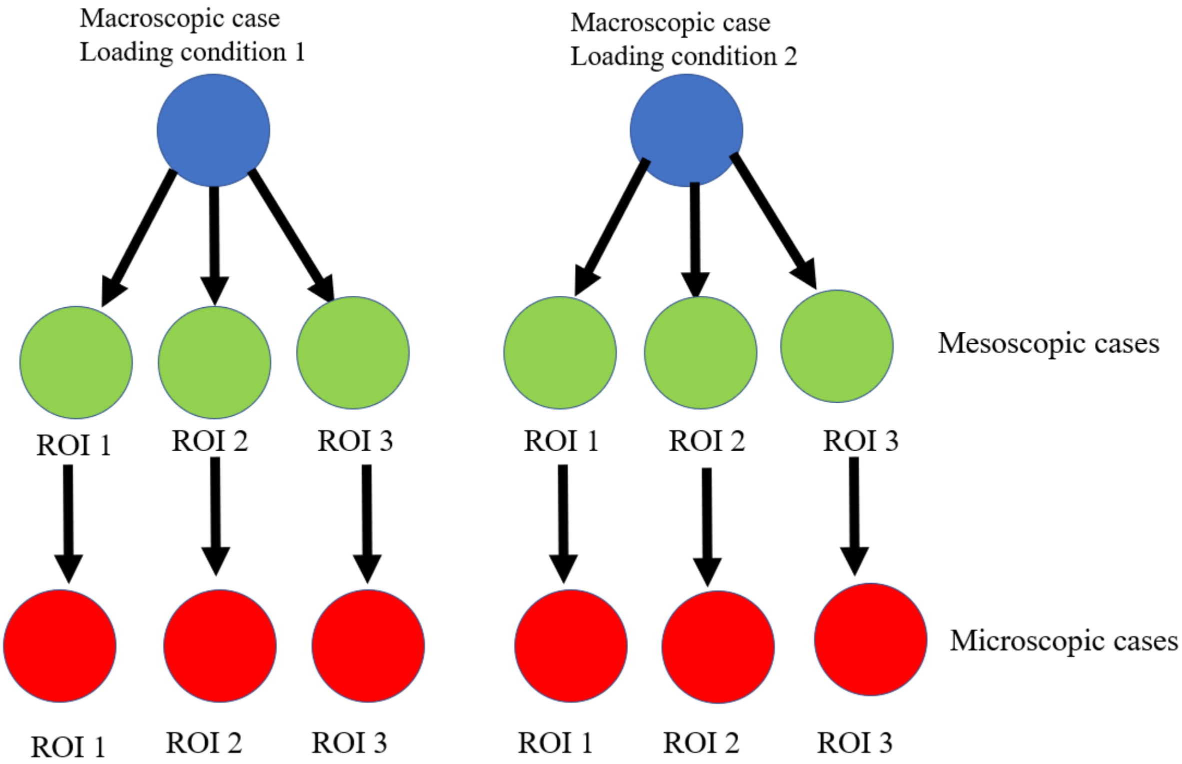

Figure 4.4 Number of cases in each scale

4.3 *Macroscopic Model*

In the macroscopic model, both the mandible and the implants are scanned separately by micro CT imaging technique of the same resolution of $90\mu\text{m} \times 90\mu\text{m} \times 50\mu\text{m}$ (Figure 4.5 (a) and (b)). The black region in the images represents empty space and the white region represents the bone of mandible and dental implants respectively. Image stacking (Figure 4.5 (c)) is firstly achieved to create the 3D structure of mandible and implant (Figure 4.5 (d) and (e)). Then the bone and implants are meshed together with the voxel elements of same size of 0.09mm (Figure 4.5 (f)). The region that is far away from the implants and some implant part is of no interest to the dentists so it is cut away to reduce computational cost. The macroscopic model is the remaining region (Figure 4.5 (i)). The dimension of the macroscopic model and the implant are shown in Figure 4.6 and Figure 4.7. About 9 mm of the implant is planted into the bone and the diameter for the implant is 4mm.

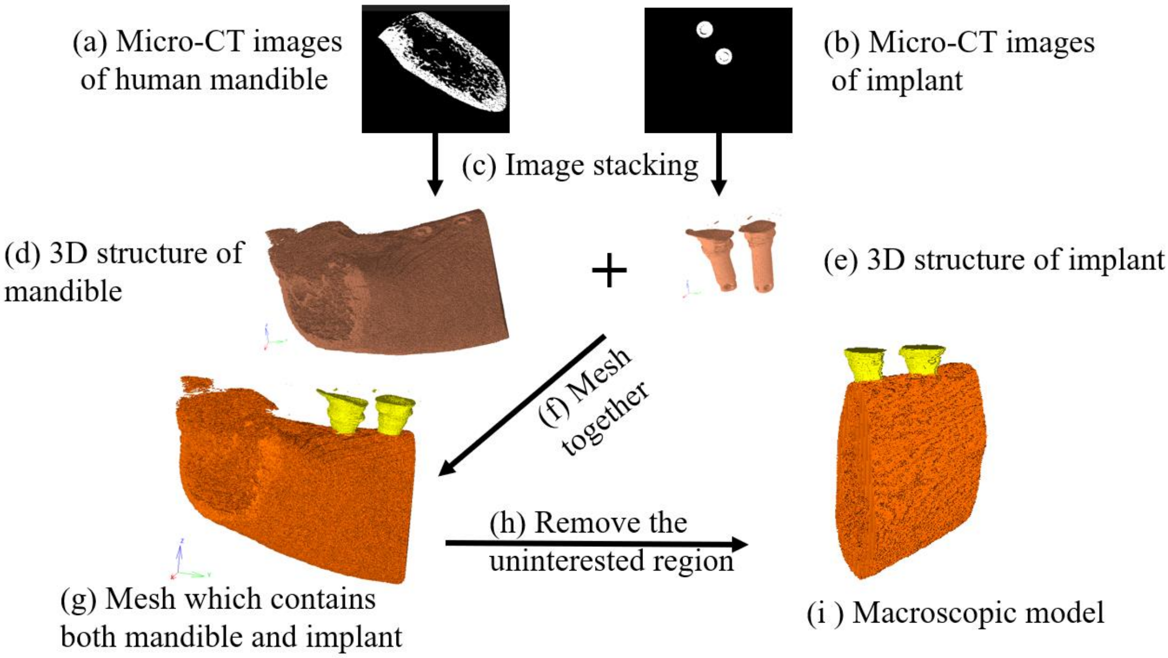

Figure 4.5 Construction of macroscopic model based on micro-CT images

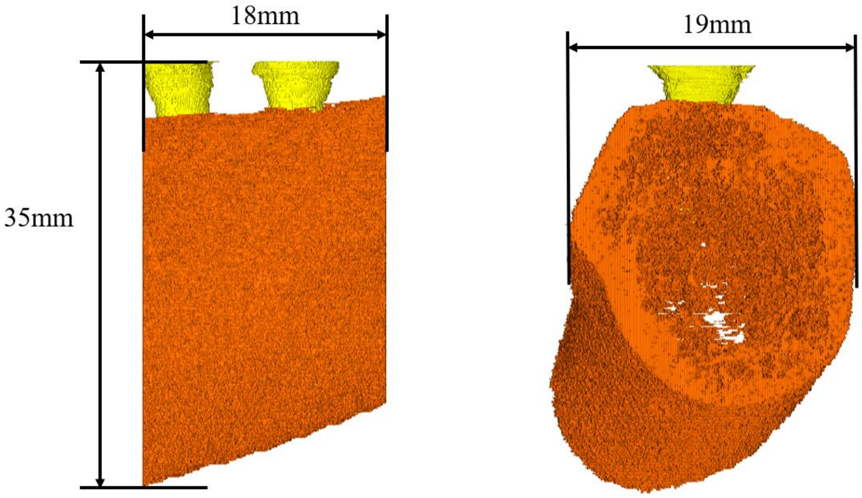

Figure 4.6 Dimension of the macroscopic model

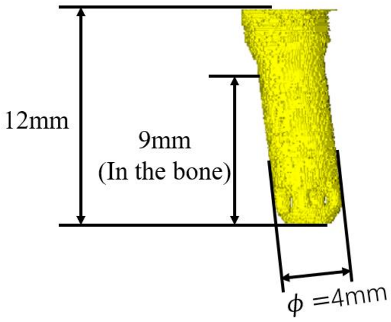

Figure 4.7 Dimension of the implant

The material properties for both the mandible and implants were set to be isotropic. The specific values of the mechanical properties were chosen from previous reference [32] and set as: $E_{bone} = 15\text{GPa}$, $v_{bone} = 0.3$ and $E_{implant} = 110\text{GPa}, v_{implant} = 0.3$. The two types of boundary condition are imposed (Figure 4.8): both the proximal surfaces are completely restrained. Two types of Dirichlet loading conditions are imposed to the macroscopic model separately: a prescribed displacement of 250nm is imposed on the top of both implants in the implant axial direction (loading condition 1) in the macroscopic model 1 and 30 degree from the axial direction (loading condition 2) in the macroscopic model 2. These values and the directions were adapted according to previous study [20].

Strain distribution of the bone around the dental implants was studied. Displacement was also output and processed using linear interpolation for the mesoscopic model.

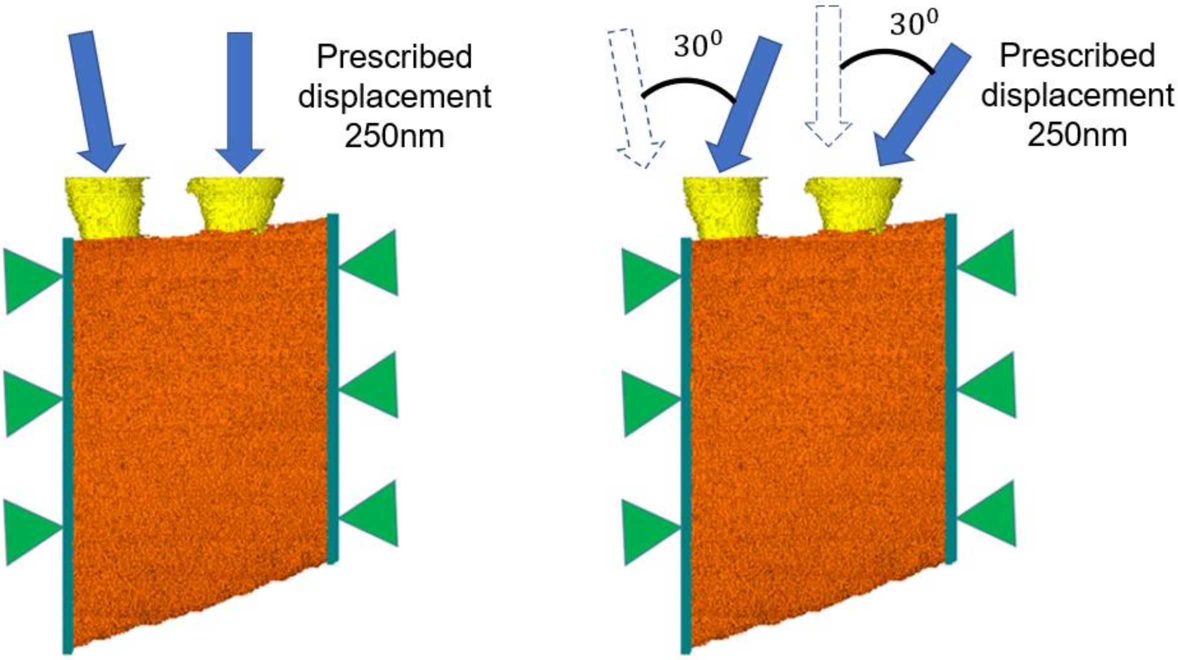

(a) Loading condition1 (Macroscopic model 1)

(b) Loading condition2 (Macroscopic model 2)

Figure 4.8 Two loading conditions for the macroscopic model

4.4 Mesoscopic Model

4.4.1 Creating mesoscopic model

The mesoscopic model is created based on the same micro-CT images as macroscopic model (Figure 4.9 (a)). Firstly the whole structure of mandible is constructed with the same micro-CT images (Figure 4.9 (c)). Then a bone region of $1\mathrm{mm}^3$ is extracted from the mandible and meshed with elements of 0.009mm (Figure 4.9 (e)). There is vacant space in the bone due to its porous structure. The vacant space is filled with collagen fibers, whose mesh size is the same as bone (Figure 4.9 (f)). Then the mesoscopic model is completely solid after filling the collagen fibers (Figure 4.9 (g)).

The material property for the mesoscopic model was set to be isotropic. The values of material property of collagen fibers followed previous research [33]. The collagen fibers are set to be isotropic: $E_{bone} = 15\mathrm{GPa},\ v_{bone} = 0.3$ and $E_{fiber} = 4.7\mathrm{MPa}, v_{fiber} = 0.3$. The mechanical property for the bone used the same value as macroscopic and mesoscopic model while the collagen fiber used the property of wet collagen fiber (about 100 times smaller than the dry collagen fiber) to simulate the situation in the living body.

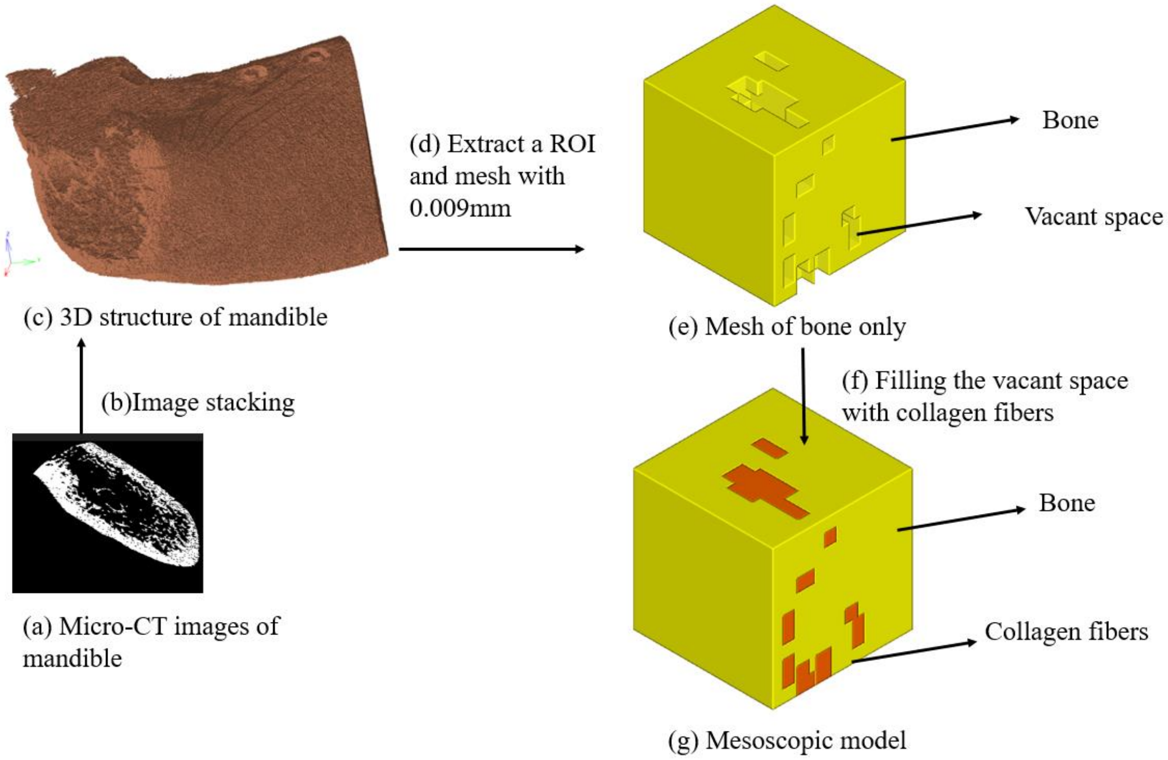

Figure 4.9 Create mesoscopic model based on same CT images as macroscopic model

4.4.2 Position of three ROIs

The position of extracting mesoscopic model depends on the region of collagen fibers which dentists are interested to study. In this study, three ROIs are selected for analysis: two ROIs near the neck of implants and one near the bottom (Figure 4.10). The reasons for selecting the two ROIs near the neck of the implant includes that the arrangement of collagen fibers near the neck of the implant is different from other regions according to the observation of dentists. Besides, the content of collagen fibers in the implant-neck region is high so that enough collagen fibers can be analyzed. A collagen-rich region near the bottom of the implant is chosen to make comparison with the two ROIs close to the implant neck.

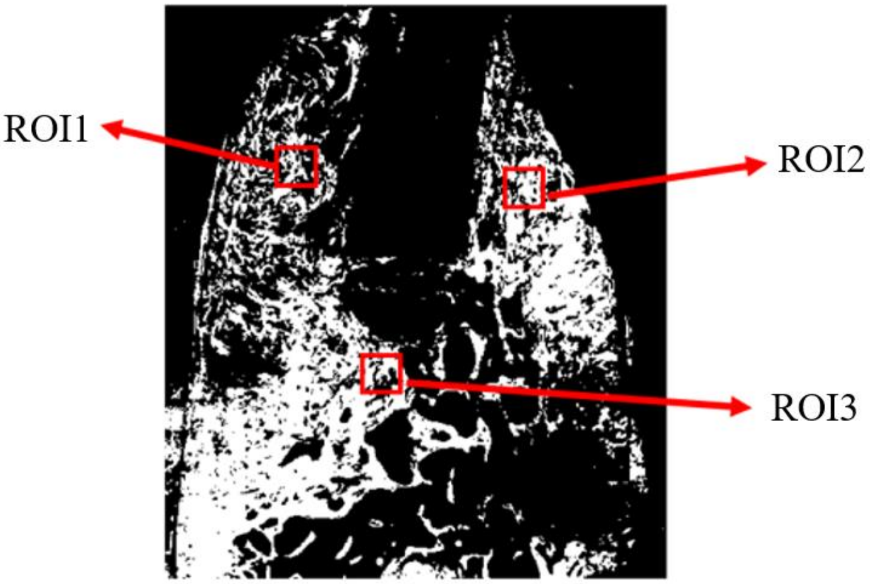

Figure 4.10 Position of the three ROIs

The exact positions of the three ROIs in the 3D view are shown in Figure 4.11, Figure 4.12 and Figure 4.13. The shortest distance of the surface of ROIs to the implant surface and the depth of the ROIs (the distance from the upper surface of the ROIs to the upper surface of the mandible) are summarized in Table 4-2. ROI 3 has a direct contact with the dental implant while the distance of ROI 1 to the implant is about two times of the diameter of an osteon and the distance of ROI 2 is close to the diameter of an osteon.

The bone volume fraction is defined as the ratio between the bone volume and total volume while fiber volume fraction is defined as the ratio between the fiber volume and total volume. They are important parameters in the biomechanical researches. The bone volume fraction and fiber volume fraction for the three ROIs are measured and shown in Table 4-3. The bone volume fraction is extremely high in the bone region near the implant neck (ROI 1 and ROI 2) and relatively lower in the implant bottom region.

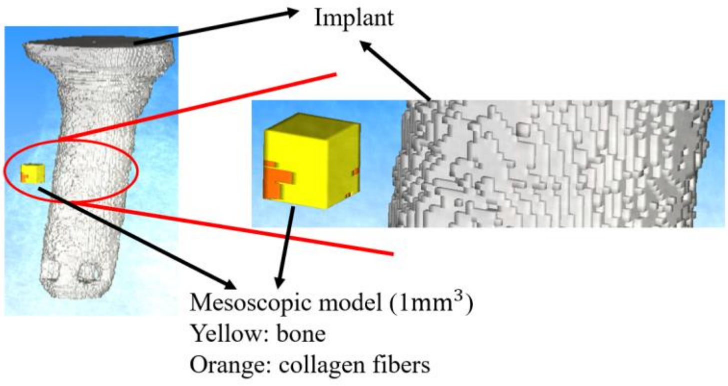

Figure 4.11 Position of mesoscopic model of ROI 1

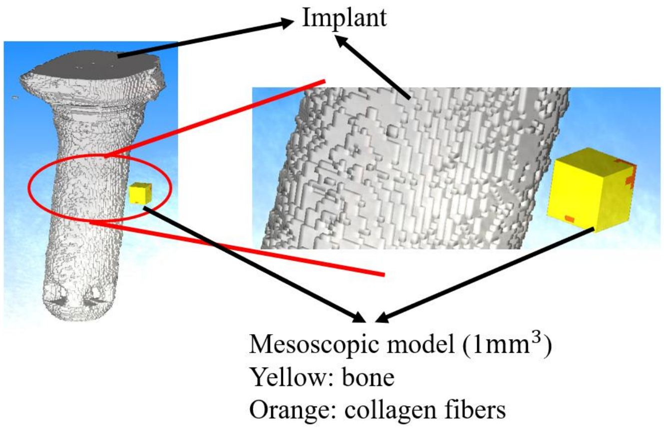

Figure 4.12 Position of mesoscopic model of ROI 2

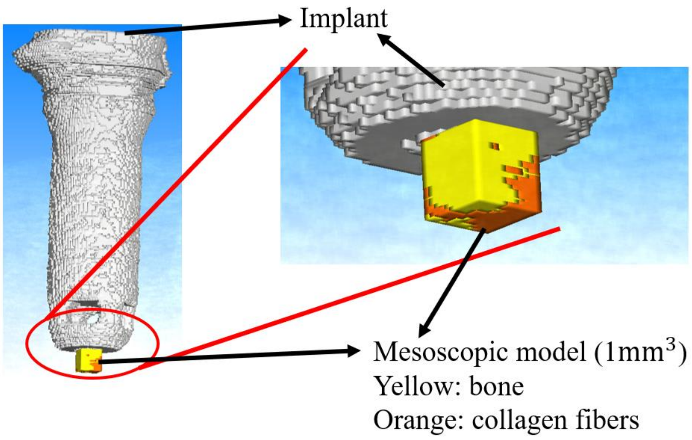

Figure 4.13 Position of mesoscopic model of ROI 3

Table 4-2 Distance of the mesoscopic ROIs to the implant and the depth of the mesoscopic ROIs

	Distance to the implant/mm	Depth /mm
ROI 1	0.8	2
ROI 2	0.4	1.5
ROI 3	0	9

Table 4-3 Bone volume fractions and fiber volume fraction of the three mesoscopic ROIs

	Bone volume fraction	Fiber volume fraction
ROI 1	97%	3%
ROI 2	95%	5%
ROI 3	63%	37%

4.4.3 Interpolation rules

The comparisons of macroscopic mesh with the mesoscopic mesh of the three ROIs are shown in Figure 4.14, Figure 4.15 and Figure 4.16. The macroscopic model is porous however the mesoscopic model is completely solid after the vacant space is filled with collagen fibers. Because the mesh size of mesoscopic mesh is 10 times smaller than the macroscopic mesh, some regions with different structures can be observed. and more structural details can be observed in the mesoscopic mesh than the macroscopic mesh. After comparison with the original medical images, the mesh of mesoscopic model is observed to be more accurate than macroscopic mesh.

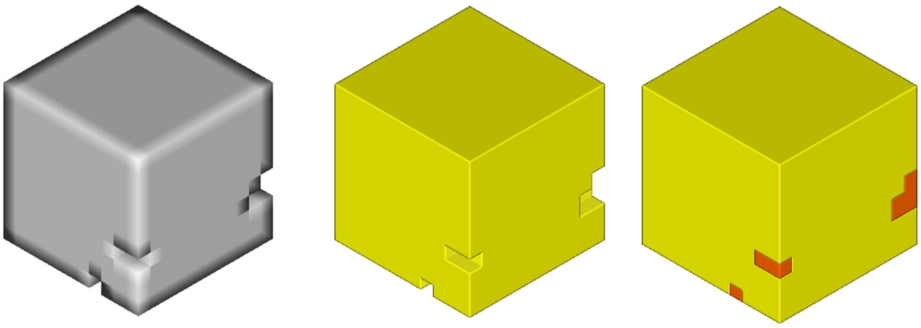
(a) Macroscopic mesh
(b) Bone part of mesoscopic mesh
(c) Complete mesoscopic mesh
Yellow: bone
Orange: collagen fibers

Figure 4.14 Comparison of macroscopic mesh with mesoscopic mesh of ROI 1

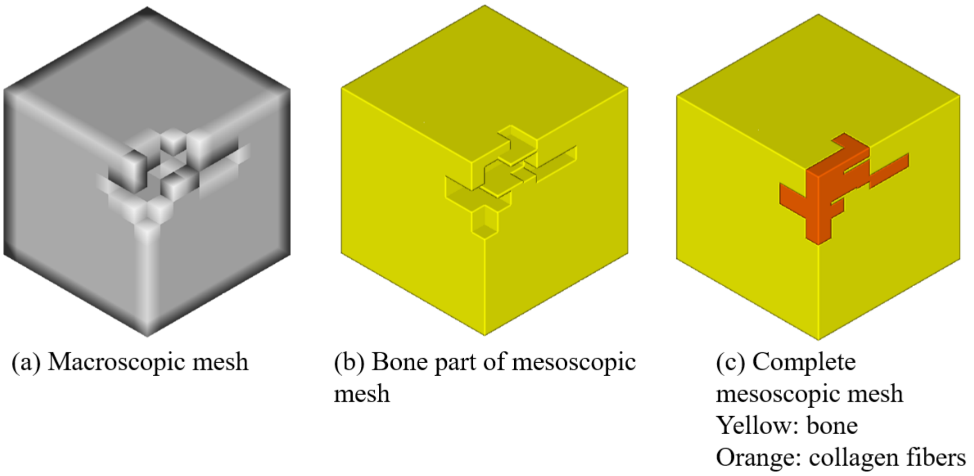
(a) Macroscopic mesh

(b) Bone part of mesoscopic mesh

(c) Complete mesoscopic mesh
Yellow: bone
Orange: collagen fibers

Figure 4.15 Comparison of macroscopic mesh with mesoscopic mesh of ROI 2

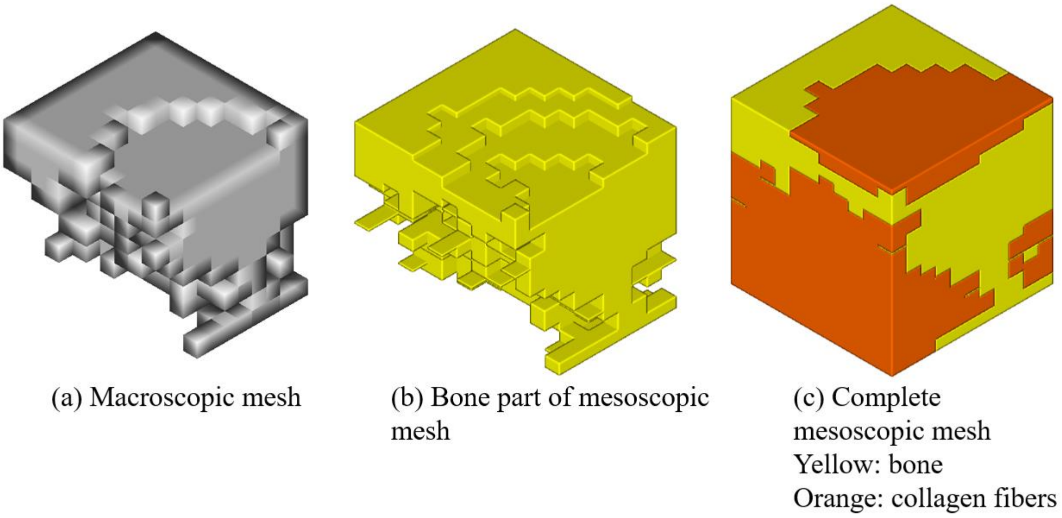
(a) Macroscopic mesh

(b) Bone part of mesoscopic mesh

(c) Complete mesoscopic mesh
Yellow: bone
Orange: collagen fibers

Figure 4.16 Comparison of macroscopic mesh with mesoscopic mesh of ROI 3

However, the different structures caused by the mesh sizes in the macroscopic mesh from the mesoscopic mesh can cause problems of interpolation using shape function introduced in 3.1.1. For example, in the same region, the mesoscopic elements and macroscopic elements can both exist (Figure 4.17 (a)). In this case interpolation can be executed because the displacement values at the eight nodes of macroscopic element are available. However, in the same region, the mesoscopic elements can exist while the macroscopic element doesn't (Figure 4.17 (b)). In this case, the macroscopic displacement at this element is unavailable and the mesoscopic displacement can't be computed with interpolation using the shape function. Therefore, a rule of interpolation has to be regulated (Figure 4.18). At the boundary of mesoscopic model, if the mesoscopic elements are not inside a macroscopic element (Figure 4.18 (a)), the interpolation is not executed and there is no boundary condition assigned to these mesoscopic elements. Meanwhile, if the mesoscopic elements are inside the macroscopic element, the interpolated displacement for the mesoscopic element is computed and used as the boundary condition of prescribed displacement.

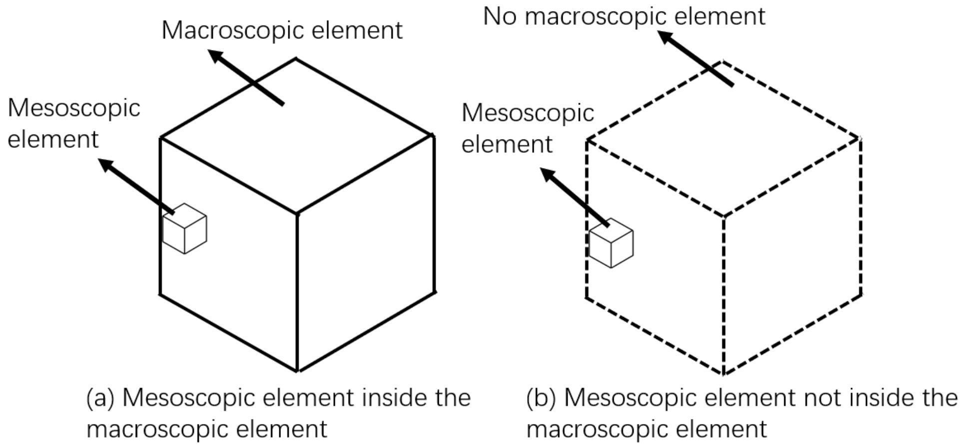

(a) Mesoscopic element inside the macroscopic element
(b) Mesoscopic element not inside the macroscopic element

Figure 4.17 Two cases of structural difference caused by mesh sizes in the macroscopic mesh and mesoscopic mesh

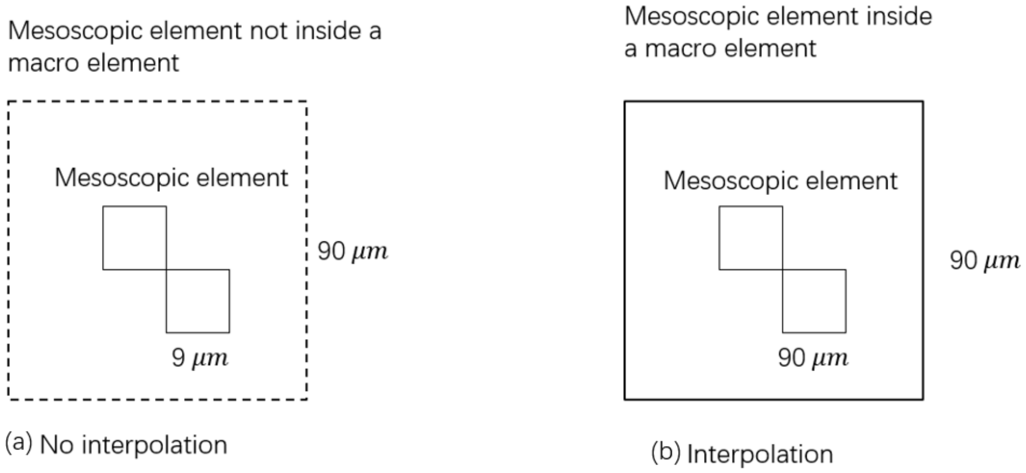

(a) No interpolation
(b) Interpolation

Figure 4.18 Rules of imposing boundary condition on the surface

After assigning the interpolated displacement to the boundary of mesoscopic model, the contours of macroscopic displacement and mesoscopic displacement can be used to ensure the correct set-up of boundary condition. For example, the comparison of macroscopic displacement and mesoscopic displacement in y direction for the ROI 1 under loading condition 1 has been made in Figure 4.19. Besides the structural difference between macroscopic model and bone part of mesoscopic model, a smoother displacement distribution can be observed in the mesoscopic model, which results from the interpolation. Also the displacement in y and z directions has to be compared in the same way to ensure the correct interpolation. Sometimes extreme values of displacement can be observed in the boundary of collagen fibers, which is caused by the interpolation rules because no displacement was assigned to the fiber nodes as a boundary condition. In the postprocessing of mesoscopic model, about 20% of total volume near the boundary will be abandoned because observable large errors.

After obtaining the mesoscopic results, the displacement of the mesoscopic model was then output and processed with linear interpolation for the boundary condition of microscopic model.

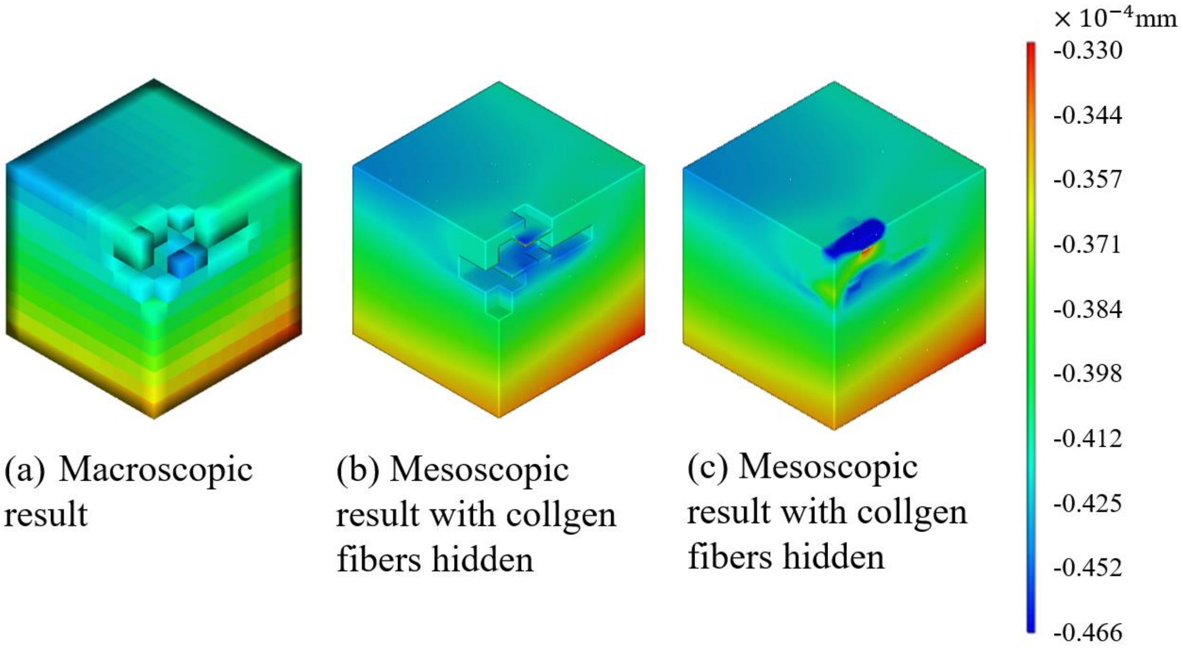

(a) Macroscopic result

(b) Mesoscopic result with collgen fibers hidden

(c) Mesoscopic result with collgen fibers hidden

Figure 4.19 Comparison of the contours of displacement in y direction between macroscopic model and mesoscopic model in ROI 2 under loading condition 1

4.5 Microscopic Model

4.5.1 Creating microscopic model

Microscopic model was based on the stitched SHG images (Figure 4.20 (a)). In the image, the white region represents the collagen fibers and the black region represents the bone. Firstly, the whole structure of collagen fibers is created using the stitched SHG images (Figure 4.20 (b)) through image stacking. Then the 3D structure of collagen fibers is moved and rotated to match with the coordinate of dental implant (Figure 4.20 (c)). Then the ROI of collagen fibers is extracted from whole structure for analysis (Figure 4.20 (d)). The vacant space in the collagen fibers is filled with bone material to make the microscopic model complete solid, after which the bone and collagen fibers are mesh together with elements of 0.002mm to create the microscopic model (Figure 4.20 (e)). The material properties for the bone and collagen fiber were both assumed to be isotropic and the values are. The values of mechanical properties for bone and collagen fibers are the same as mesoscopic model.

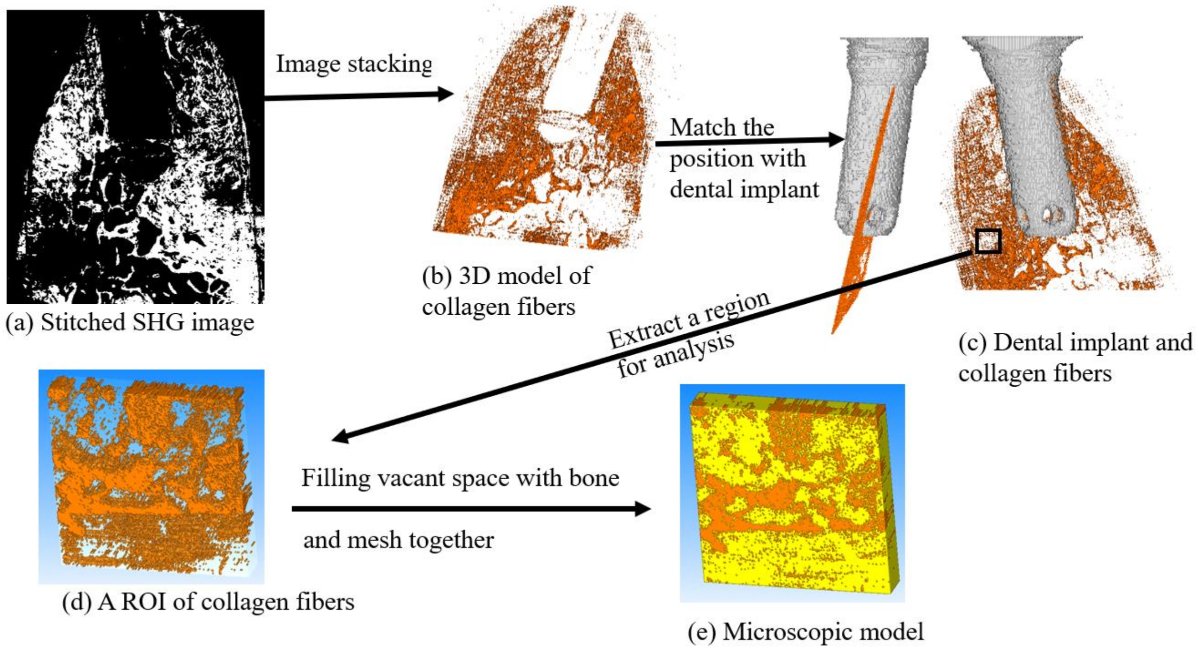

(a) Stitched SHG image

(b) 3D model of collagen fibers

(c) Dental implant and collagen fibers

(d) A ROI of collagen fibers

(e) Microscopic model

Figure 4.20 Construction of microscopic model with the stitched SHG images.

4.5.2 Rules of extracting microscopic model

A ROI image is the SHG image extracted from the stitched image and used to create the microscopic model. Even if in this study, the microscopic model is directly extracted from the 3D model of the whole structure of collagen fiber, the ROI image can be extracted according to the coordinate of the ROI and used to check if the microscopic mesh correctly matches the ROI image. The procedure to extract the ROI image is shown in Figure 4.21. The stitched image consists of $17{,}000 \times 19{,}000$ pixels (Figure 4.21 (a)), which can be converted into a $17{,}000\ \text{by}19{,}000$ matrix. Then a ROI matrix of 600 by 600 is extracted based on its coordinate and finally the matrix is converted back to the ROI image (Figure 4.21 (b)), whose pixel number is 600×600.

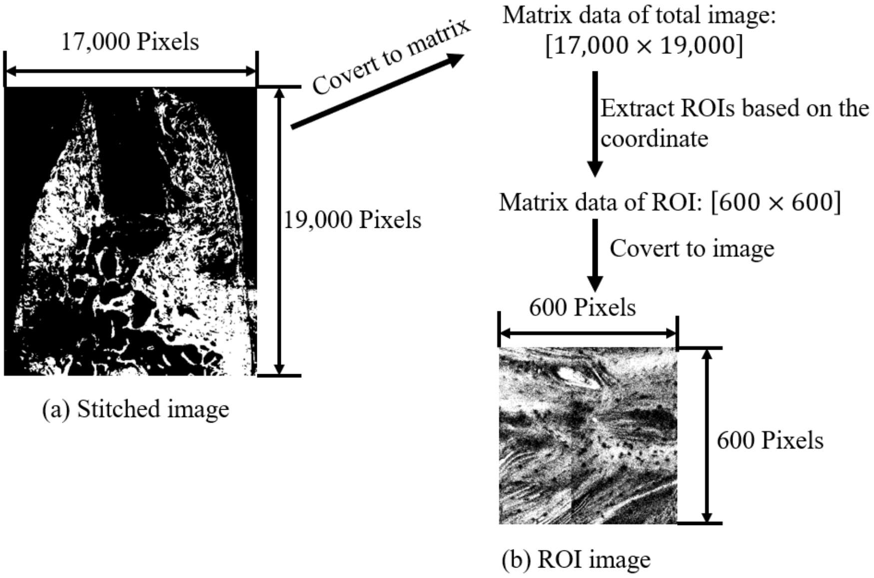

Figure 4.21 Procedures to extract the ROI image

To avoid computational errors and imaging errors, rules for selecting the exact position of microscopic model are proposed. Firstly, there are errors in the imaging caused by image-stitching (Figure 4.22 (b)). The straight line is visible at the stitching boundary of two discrete images, which results in the non-continuity of the 3D structures. And one discrete image contains 1024×1024 pixels and one ROI image contains 600×600 pixels. So when selecting the position of microscopic model, it's necessary to avoid the stitching boundary and place it close to the center of the discrete image because the size of ROI image is smaller than one discrete image.

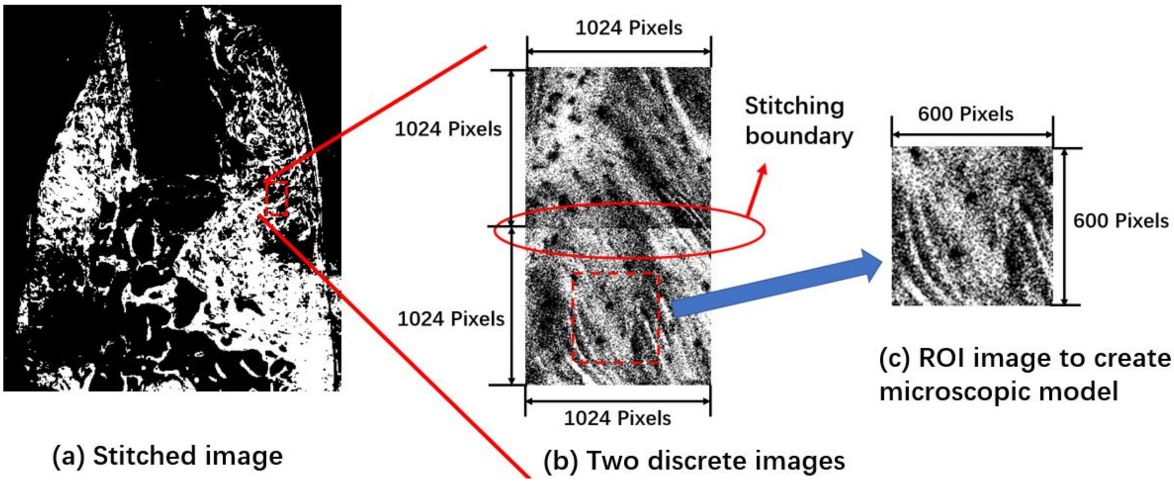

Figure 4.22 Stitching boundary of two discrete images

There are five slices of stitched images in total, which takes small effort to check the ROI images one by one. The ROI images for the three ROIs are displayed in Figure

4.23, Figure 4.24 and Figure 4.25. For the ROI images of ROI 1, the last two slices are not continuous compared with the first three slices, which contains little information about collagen fibers. Besides, last two slices of the stitched SHG images are not continuous in the neighboring region of left neck of the dental implant. So the last two slices are abandoned to construct the microscopic model of ROI 1. The reason is the same for ROI 2, in which the last slice is abandoned (Figure 4.24). And for the ROI 3, all the five slices are continuous and used to create the microscopic model (Figure 4.25).

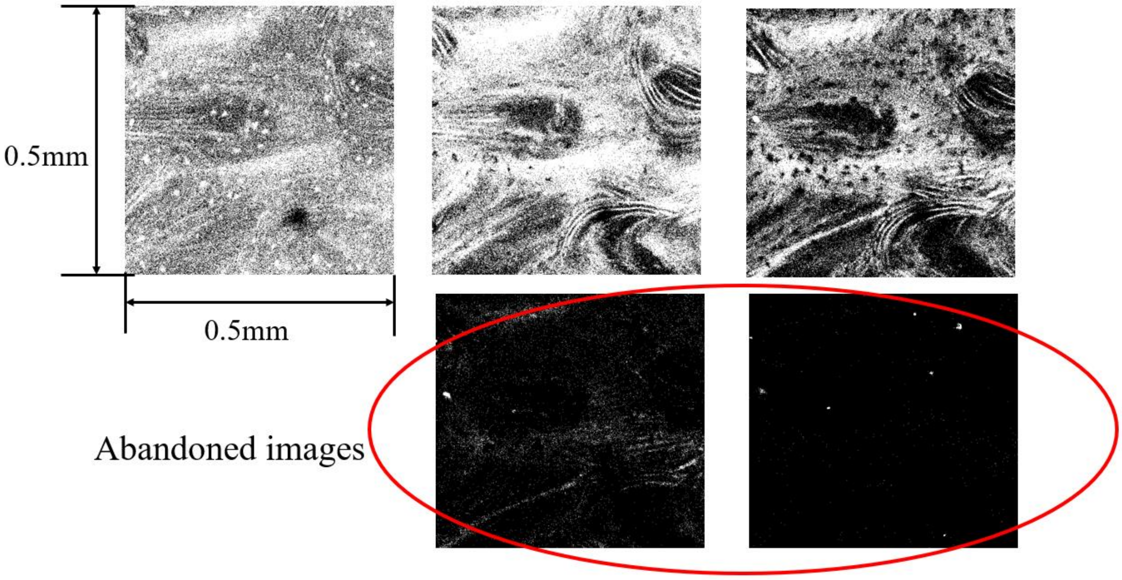

Figure 4.23 Five ROI images of ROI 1

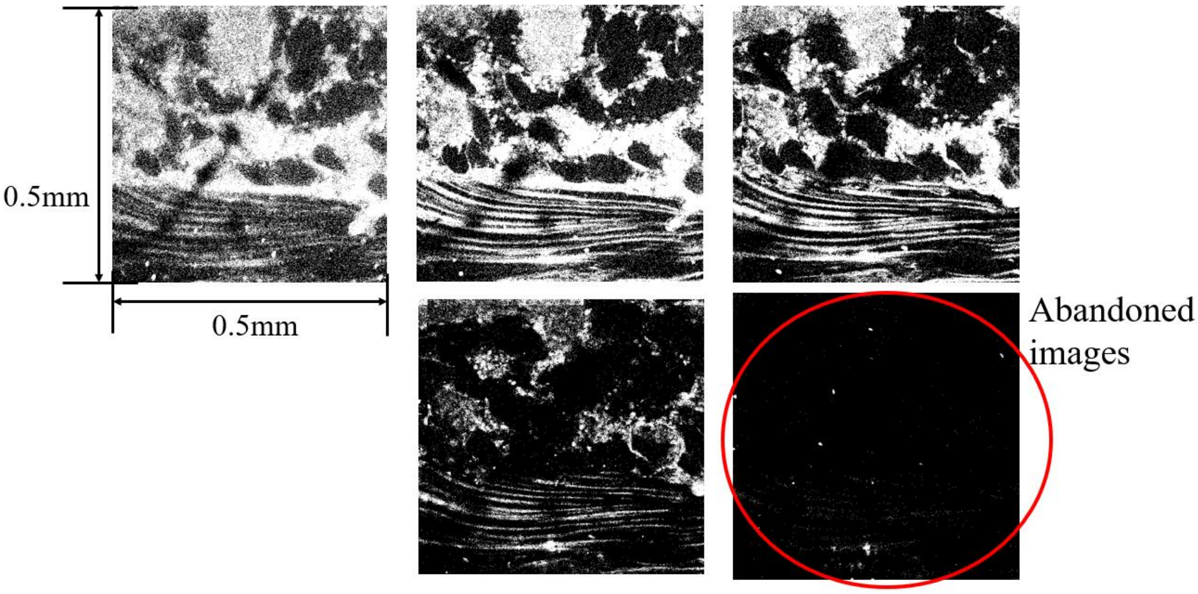

Figure 4.24 Five ROI images of ROI 2

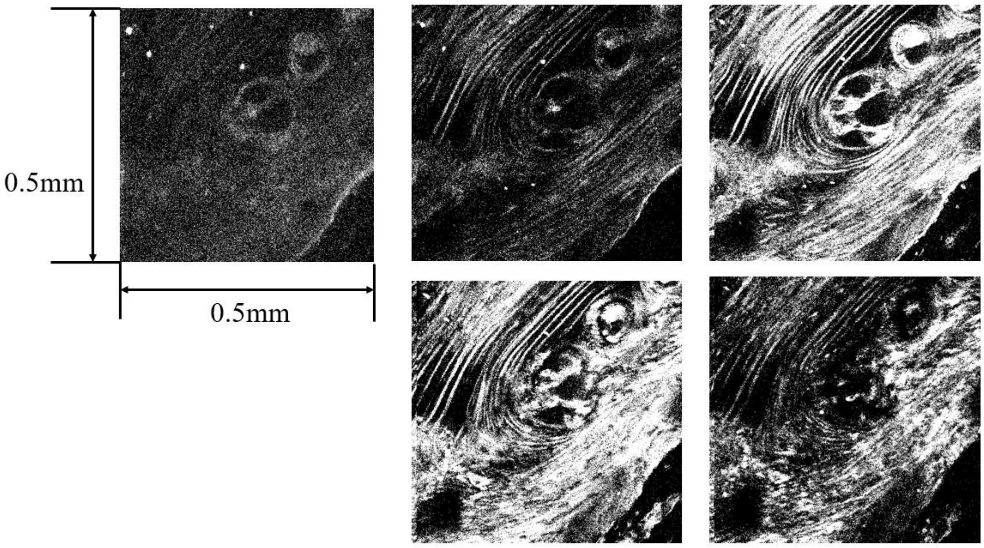

Figure 4.25 Five ROI images of ROI 2

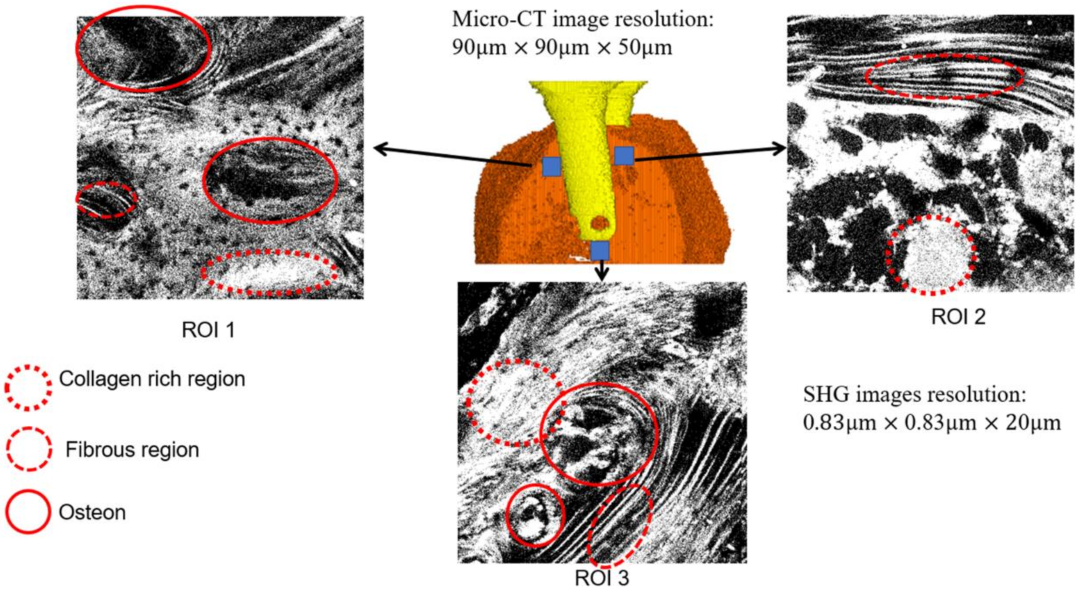

Figure 4.26 Explanation of the SHG images of the three ROIs

In the SHG images, there are mainly three types of region: collagen rich region, fibrous region and osteon (Figure 4.26). In the collagen rich region, the collagen fibers are distributed concentratedly. And in the fibrous region, the collagen fibers are scattered. In the osteon, a circled black region can be observed and the black region is the Harversian cannel.

The microscopic mesh of the three ROIs are shown in Figure 4.27, Figure 4.28 and Figure 4.29. The thickness for ROI 1 is 0.06mm, ROI 2 is 0.08mm and ROI 3 is

0.1mm because different number of slices are used. The bone volume fraction and fiber volume fraction for the three ROIs are measured and shown in Table 4-4. The fiber volume fraction of ROI 2 and ROI 3 are nearly equal while the fiber volume fraction of ROI 1 is twice as ROI 2 and ROI 3.

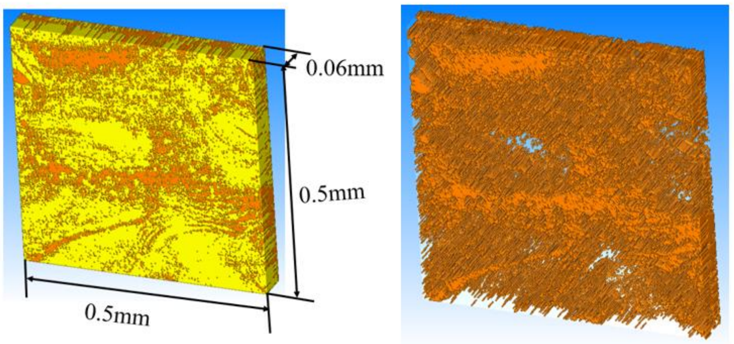

(a) Microscopic mesh of bone and fibers

(b) Microscopic mesh of fibers

Figure 4.27 Microscopic mesh of ROI 1. Yellow: bone; orange: collagen fibers

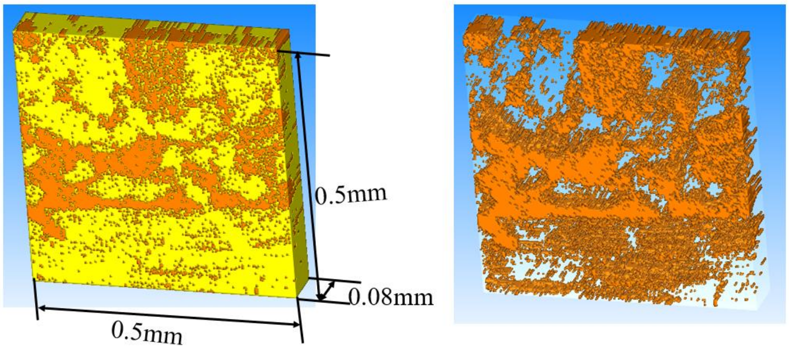

(a) Microscopic mesh of bone and fibers

(b) Microscopic mesh of fibers

Figure 4.28 Microscopic mesh of ROI 2. Yellow: bone; orange: collagen fibers

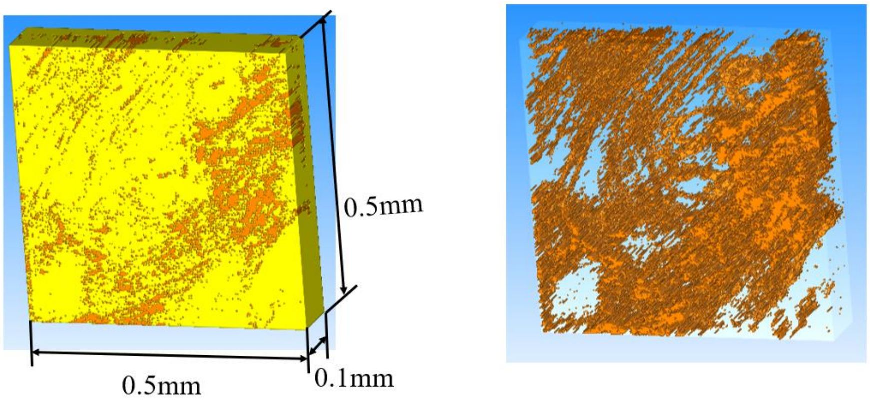

(a) Microscopic mesh of bone and fibers

(b) Microscopic mesh of fibers

Figure 4.29 Microscopic mesh of ROI 3. Yellow: bone; orange: collagen fibers

Table 4-4 Bone volume fraction and fiber volume fraction for the three microscopic ROIs

	Bone volume fraction	Fiber volume fraction
ROI 1	65%	35%
ROI 2	82%	18%
ROI 3	83%	17%

Finally, to reduce the computational errors, the position of microscopic model locates at the center of mesoscopic model because according to observation, the large computational error caused by interpolation.

4.5.3 Exact position of the three ROIs

The position of the three ROIs in the mesoscopic model is shown in Figure 4.30, Figure 4.31 and Figure 4.32. The mesoscopic models are made transparent to observe the exact position of the microscopic model. The microscopic model locates near the center of each mesoscopic model. And the relative position of the microscopic model and implant is shown in Figure 4.33. As it can be observed, the thickness direction of the three plate ROIs are almost perpendicular to the implant axis. Table 4-5 shows the measurement of the distance of the microscopic ROIs to the dental implant and their depth.

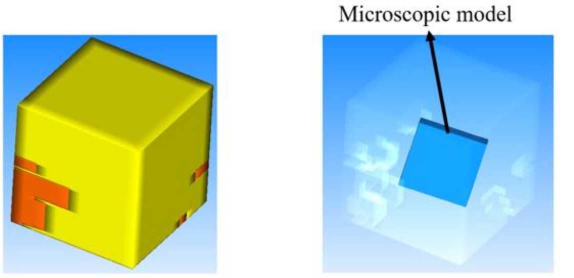

(a) Mesoscopic model
Orange: bone mesh
Yellow: fiber mesh

(b) Microscopic model in the mesoscopic model

Figure 4.30 Position of microscopic ROI 1 in the mesoscopic model

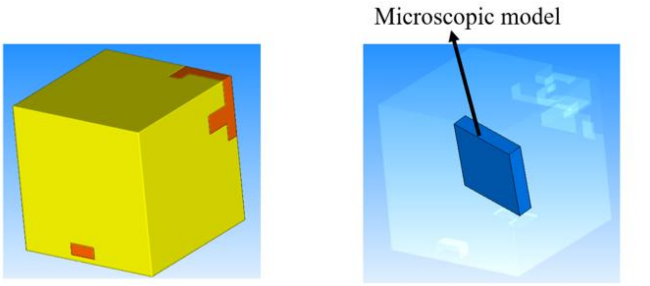

(a) Mesoscopic model
Orange: bone mesh
Yellow: fiber mesh

(b) Microscopic model in the mesoscopic model

Figure 4.31 Position of microscopic ROI 2 in the mesoscopic model

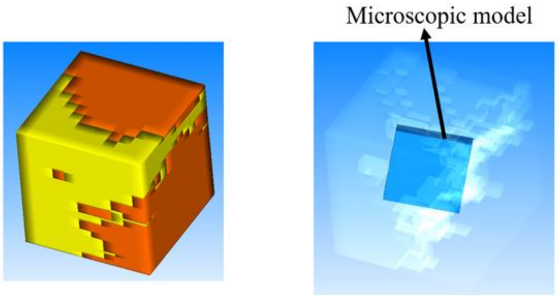

(a) Mesoscopic model
Orange: bone mesh
Yellow: fiber mesh

(b) Microscopic model in the mesoscopic model

Figure 4.32 Position of microscopic ROI 3 in the mesoscopic model

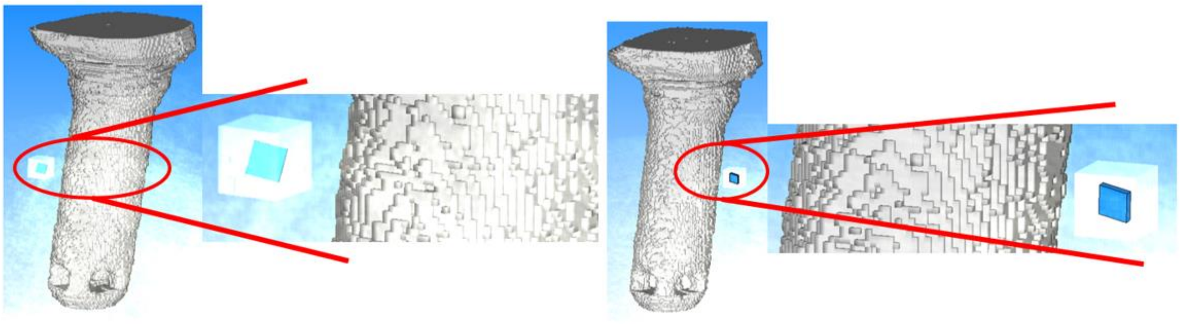

(a) Position of ROI 1

(b) Position of ROI 2

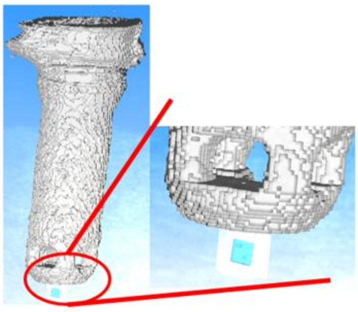

(c) Position of ROI 3

Figure 4.33 Exact position of the three ROIs in the global coordinate

Table 4-5 Distance of the microscopic models to the dental implant and the depth of the microscopic ROIs

	Distance to the implant/mm	Depth /mm
ROI 1	1.01	2.12
ROI 2	0.57	1.71
ROI 3	0.22	9.16

The displacement of the plate-shape ROI is computed through interpolation of mesoscopic displacement and used as the boundary condition for the microscopic model. All the nodes on the surface were imposed the interpolated displacement obtained from the mesoscopic model. The stress and strain distribution of the collagen fibers are analyzed and studied.

4.6 Geometrical nonlinear analysis of microscopic model

The macroscopic analysis, mesoscopic analysis and microscopic analysis are all neglecting the geometrical nonlinear effects. To explore if the geometrical nonlinear effect can be neglected, a region in the ROI 3 in the microscopic model (Figure 4.34) was selected for testing in COMSOL, which includes both bone and collagen fibers. Because the number of elements is exceeding the computational capability of the software, the geometrical nonlinear effect of the whole microscopic model can't be checked. As a result only a smaller region is selected for testing. The size of testing region is $0.13\mathrm{mm} \times 0.13\mathrm{mm} \times 0.05\mathrm{mm}$. The mechanical properties for both bone and collagen fibers adopts the same values as microscopic model. The mesh size is 0.002mm and the total number of elements is 100,000. The bone volume fraction is 65% and fiber volume fraction is 35%, which is higher than the fiber volume fraction of the microscopic model ROI 3.

One surface of the microscopic model is constrained completely and tension is applied on the opposite surface. Loading curves of *F* against the average displacement of the forced surface under linear and geometrical nonlinear analysis can be obtained. The strain distribution in the region of macroscopic model near dental implant can be obtained in the macroscopic model and the maximum strain value can be calculated. If the maximum strain value exceed the threshold, geometrical nonlinear effects will be caused. In the next chapter, the deformation of the geometrical nonlinear model will be compared with the threshold. Also, the discussion about the loading curve and the maximum strain value in the region near the dental implant will be made. And result of linear analysis and nonlinear analysis will be compared.

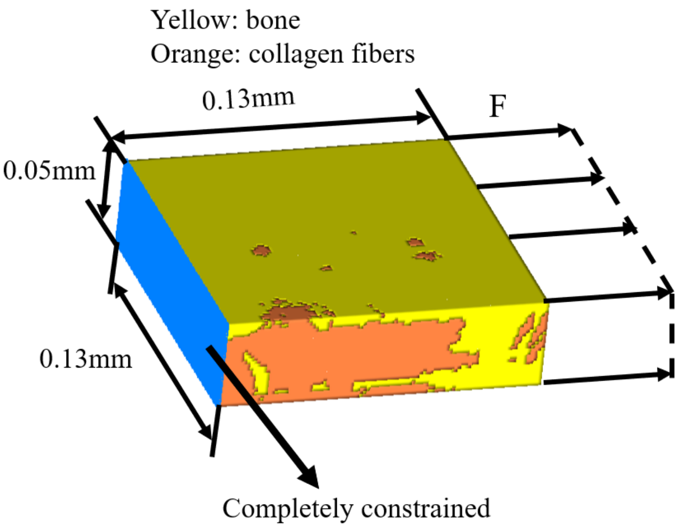

Figure 4.34 Set-up of geometrical nonlinear analysis for microscopic model

5 Results

5.1 Results of macroscopic model

Only the region near the implant is of interest to the author. So the rest of region is hidden and only the bone region near the dental implant is studied (Figure 5.1).

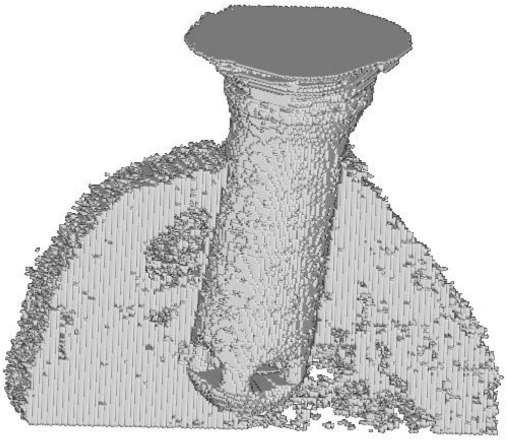

Figure 5.1 Region to observe

Under both boundary conditions, the implant is subjected to compression, so the minimum principal strain of implant is firstly observed (Figure 5.2). Under both boundary conditions, in most region of the implant, the strain level is higher than 6.7e-6. However, in the right bottom region of the implant under both boundary conditions, the strain level is relatively lower, which results from the relatively lower bone volume fraction near the right bottom region of the implant.

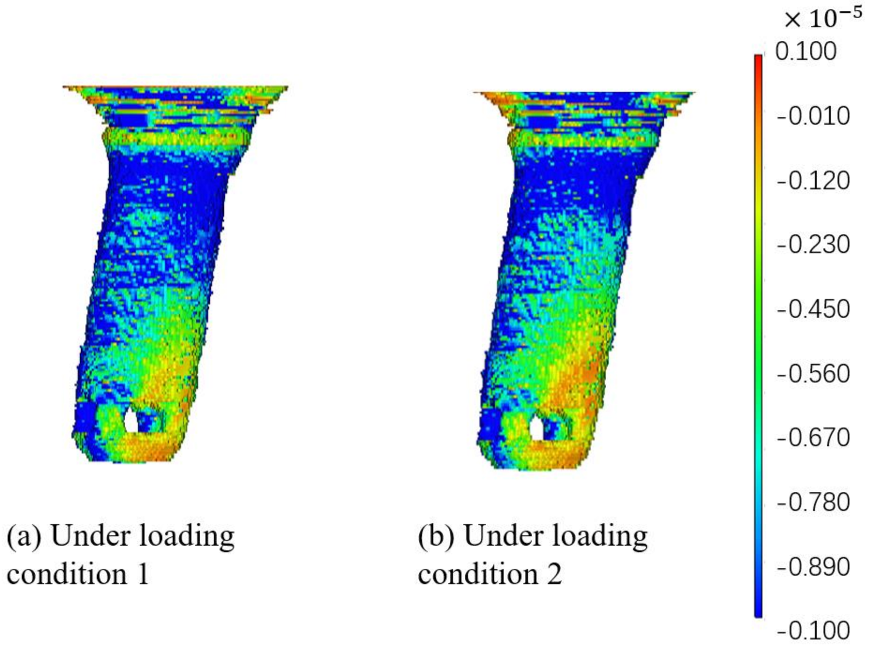

(a) Under loading condition 1

(b) Under loading condition 2

Figure 5.2 Minimum principal strain of the implant

The minimum principle strain of the bone and implant is shown in Figure 5.3, in which deformed shape is shown. From the deformed shape, the boundary conditions of different angled prescribed displacement can be ensured. The maximum principal strain of the bone is shown in Figure 5.4. And five cross-section views of the bone under two loading conditions are shown in Figure 5.5. First of all, the bone volume fraction is relatively low near the bottom of implant especially near the bottom right. And this is the reason why the right bottom region of implant is subjected to small compression. After comparing the strain values between the implant and bone, it can be observed that the strain level of the bone is higher than the implant because the implant is stiffer than the bone.

Combining the distribution of maximum principal strain, minimum principal strain and Von Mises strain, conclusion can be drawn that the bone region near the dental implant, the strain values are higher than the region which further away from the implant. And for this cadaver, in the left half regio, the region with a higher strain level is higher than the right region. Besides, under loading condition 2, the area with high strain is larger than the loading condition 1 in the left bone region of dental implant while in the right bone region near the dental implant, the area with high strain is smaller than the loading condition 1.

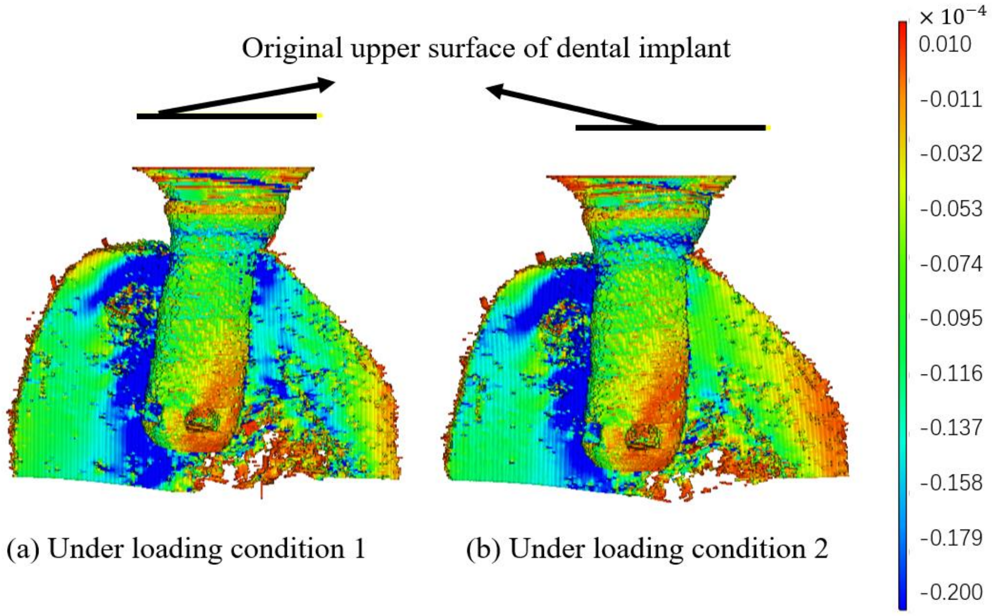

(a) Under loading condition 1

(b) Under loading condition 2

Figure 5.3 Minimum principal strain of implant and bone under both loading conditions with deformed shape

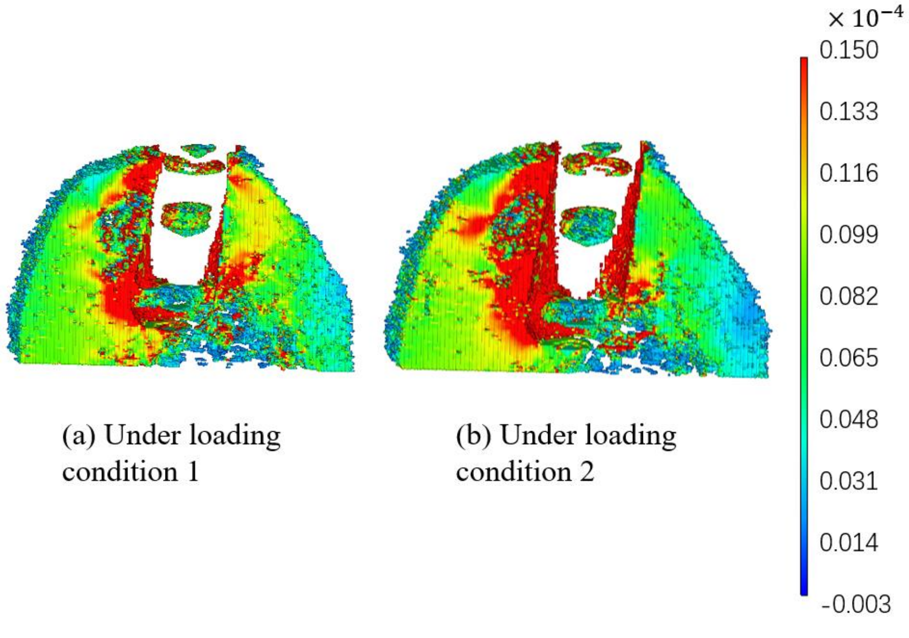

(a) Under loading condition 1

(b) Under loading condition 2

Figure 5.4 Maximum principal strain of the bone under both loading conditions

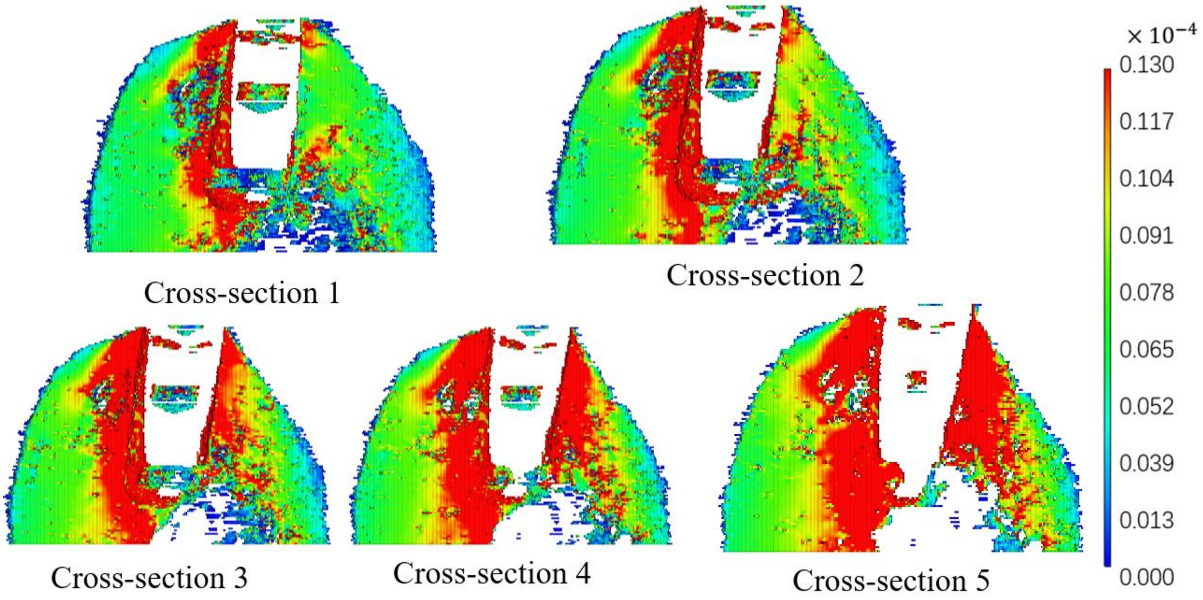

Cross-section 1 Cross-section 2 Cross-section 3 Cross-section 4 Cross-section 5

Figure 5.5 Cross-section view of Mises strain of the bone in the macroscopic model under loading condition 1

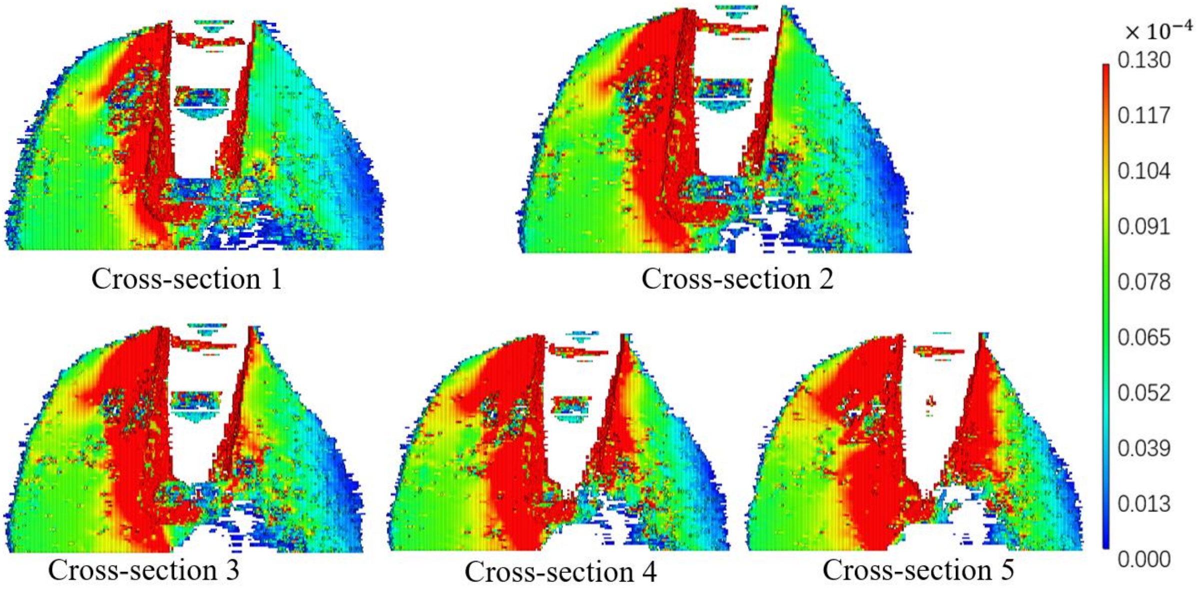

Cross-section 1 Cross-section 2 Cross-section 3 Cross-section 4 Cross-section 5

Figure 5.6 Cross-section view of Mises strain of the bone in the macroscopic model under loading condition 2

Finally, the maximum and minimum strain values of the bone near the dental implant is shown in Table 5-1.The strain values are all smaller than 0.04%, which is small enough to neglect the geometrical nonlinear effect of the bone. The Von Mises strain under both loading conditions are nearly equal while the compression and tension is larger under loading condition 1.

Table 5-1 Maximum values of maximum principal strain, minimum principal and Von Mises strain in the bone region near the dental implant under both loading conditions

	Loading condition 1			Loading condition 2		
	Maximum principal strain	Minimum principal strain	Von Mises Strain	Maximum principal strain	Minimum principal strain	Von Mises Strain
Max	3.04E-04	-3.60E-04	1.70E-04	2.66E-04	-3.32E-04	1.71E-04

5.2 Results of microscopic model

5.2.1 Microscopic mechanical environment

The mechanical environment of the microscopic models is determined by the macroscopic model in the ROI region, which helps us to understand the microscopic results. The averaged macroscopic strain tensors in the three ROIs under both loading conditions are computed (Figure 5.7). And the averaged and maximum strain values are presented in Table 5-2.

First of all, from the strain vectors, the change of loading conditions don’t change the averaged strain vectors dramatically. ROI 1 is under large shear stress under loading conditions. As for ROI 2, it’s also dorminated by shear strain but the strain level is lower than ROI 1 under both loading conditions. ROI 3 is dominanted by compression under both loading conditions. The strain level in ROI 3 region is not high because the bone volume fraction at the implant bottom region is low however the strain concentration occurs. These mechanical environonment matches previous research [19].

Comparison is made between the strain direction with the collagen fiber orientation in the fibrous region in Figure 4.11, Figure 4.12 and Figure 4.13. The compression direction is almost parallel to fiber orientation in ROI 3. However the connection between fibrous orientation and loading direction is not observed in ROI 1 and ROI 2.

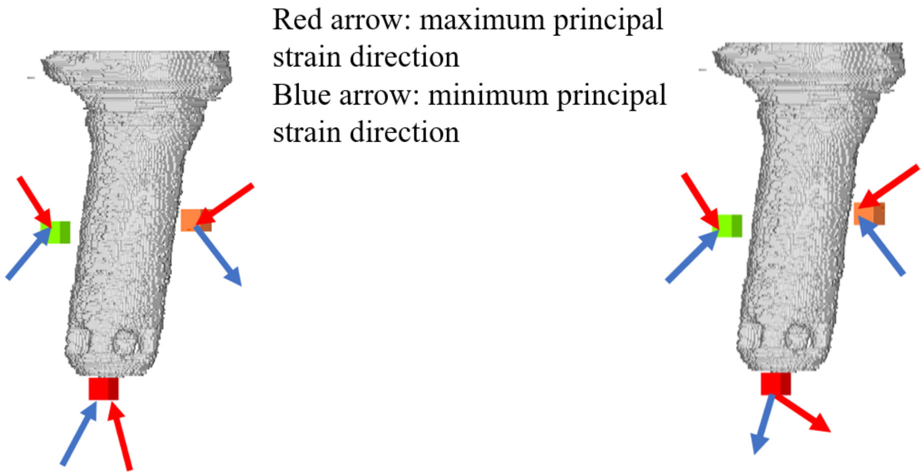

(a) Under loading condition 1 (b) Under loading condition 2

Figure 5.7 Average principal strain direction of the ROIs under both loading conditions

Table 5-2 The averaged and maximum strain values of the macroscopic ROI. $\langle\varepsilon_1\rangle$: averaged maximum principal strain; $\langle\varepsilon_3\rangle$: averaged minimum principal strain; $\langle\vec{\varepsilon}\rangle_{max}$: maximum strain.

	Loading condition 1		
	$\langle\varepsilon_1\rangle$	$\langle\varepsilon_3\rangle$	$\langle\vec{\varepsilon}\rangle_{max}$
ROI 1	2.8×10^{-5}	-2.9×10^{-5}	3.5×10^{-5}
ROI 2	1.5×10^{-5}	-2.3×10^{-5}	3.05×10^{-5}
ROI 3	7.6×10^{-6}	-1.83×10^{-5}	4.2×10^{-5}
	Loading condition 2		
	$\langle\varepsilon_1\rangle$	$\langle\varepsilon_3\rangle$	$\langle\vec{\varepsilon}\rangle_{max}$
ROI 1	2.7×10^{-5}	-3.2×10^{-5}	3.3×10^{-5}
ROI 2	9.8×10^{-6}	-1.26×10^{-5}	1.7×10^{-5}
ROI 3	7.7×10^{-6}	-1.3×10^{-5}	3.3×10^{-5}

5.2.2 *Results of microscopic model*

The maximum principal strain and minimum principal strain distributions of the three ROIs under loading condition 1 are displayed in Figure 5.8 and Figure 5.9. The overall strain levels of collagen fibers are higher than the bone. And in all the three ROIs, strain concentration can be observed in the collagen rich region in both maximum principal strain and minimum principal strain, which means the collagen rich regions are subjected to large compression and tension at the same time. And in the fibrous regionregion around the osteon, high strain is not observed. The same phenomenon of strain concentration can be observed in the strain distribution of the three ROIs under loading condition 2 even though in a different strain level.

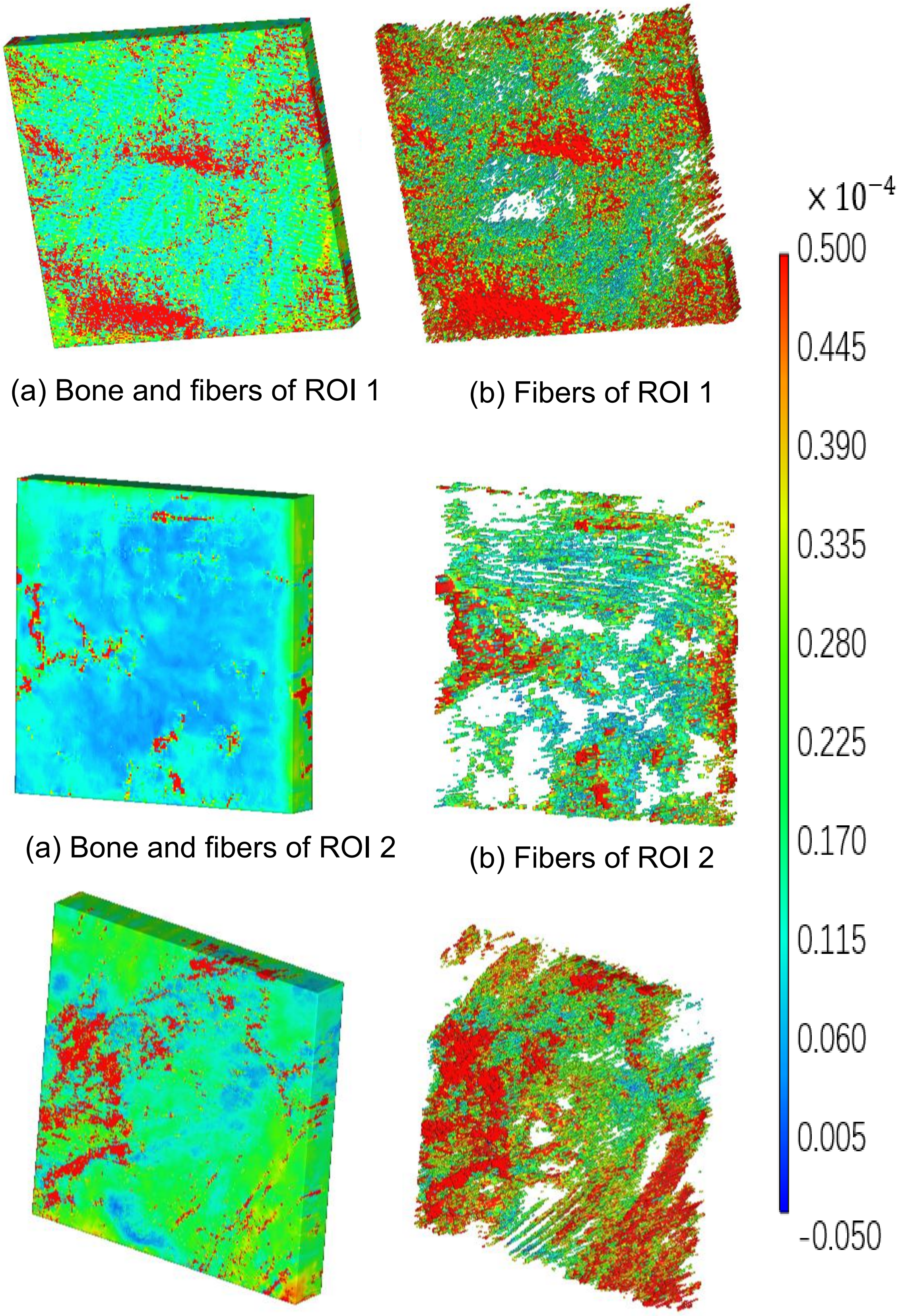

(a) Bone and fibers of ROI 1

(b) Fibers of ROI 1

(a) Bone and fibers of ROI 2

(b) Fibers of ROI 2

(a) Bone and fibers of ROI 3

(b) Fibers of ROI 3

Figure 5.8 Maximum principal strain of the three ROIs under loading condition 1

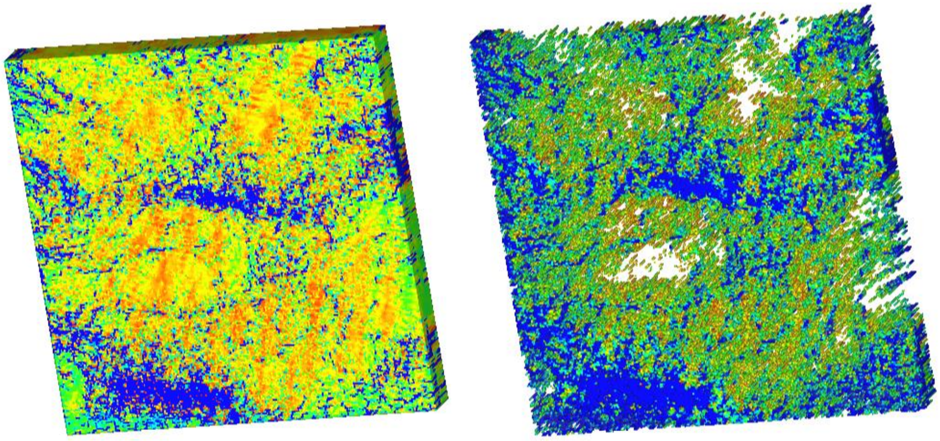

(a) Bone and fibers of ROI 1 (b) Fibers of ROI 1

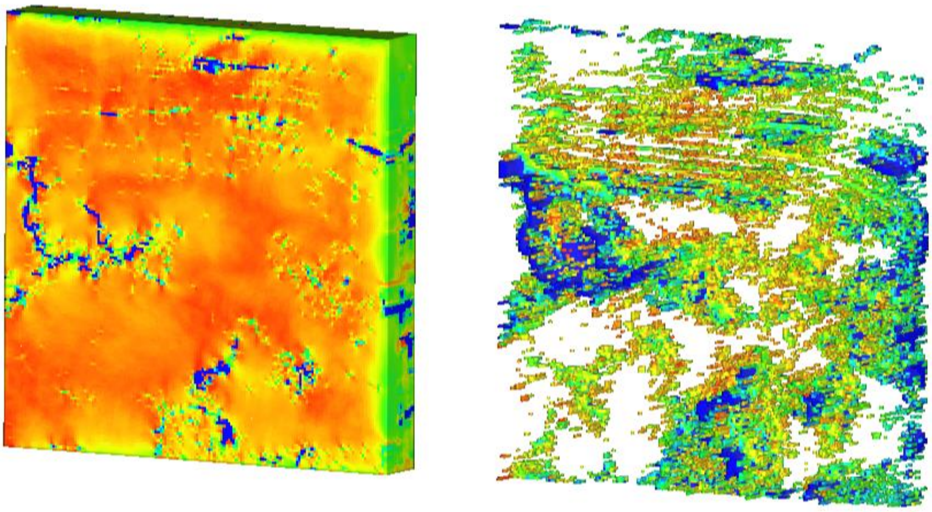

(a) Bone and fibers of ROI 2 (b) Fibers of ROI 2

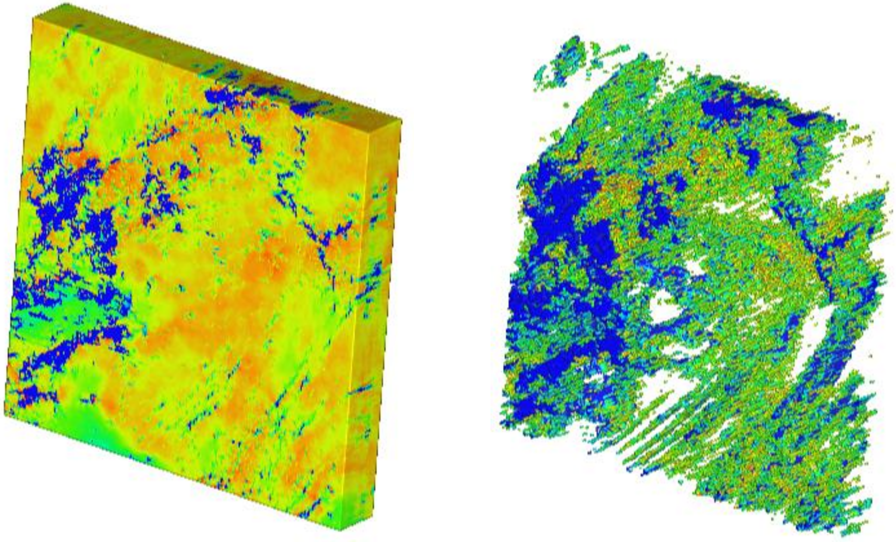

(a) Bone and fibers of ROI 3 (b) Fibers of ROI 3

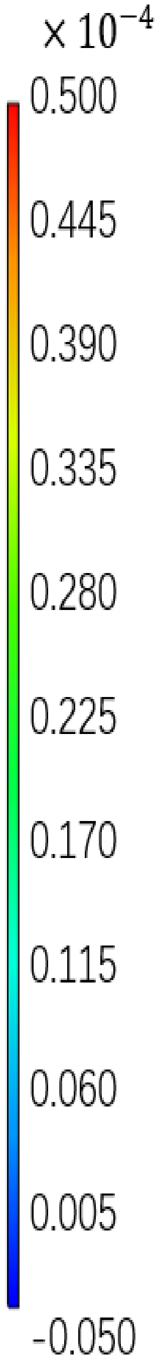

Figure 5.9 Minimum principal strain of the three ROIs under loading condition 1

To have a better view of the strain distribution of the fibers, cross-section views are taken to observe the strain distribution of collagen fibers in the three ROIs under loading condition 1 (Figure 5.10, Figure 5.11 and Figure 5.12). Because the thickness of the three ROIs are different, the intervals to take the cross-section are also different. For ROI 1, the thickness of the ROI is 0.06mm and the interval is 0.009mm. For ROI 2, the thickness is 0.08mm and the interval is 0.012mm. For ROI 3, the thickness is 0.1mm and the interval is 0.015mm.

In the cross-sections where small fiber volume fraction is observed such as cross-section 6 of ROI 3 (Figure 5.12), the strain values are relatively small. And In the cross-sections where high fiber volume fraction is observed such as cross-section 1 of ROI 1 (Figure 5.10), the strain levels are high. For the three ROIs under the loading condition 2, the same phenomenon can also be observed.

To study the strain level of microscopic models more quantitatively, the maximum strain values of collagen fibers in the three ROIs under both loading conditions are compared in Table 5-3. First of all, the maximum strain levels under loading condition 1 are all higher than loading condition 2 in the three ROIs. Under both loading conditions, both ROI 1 and ROI 2 are under shear stress meanwhile the maximum strain level of ROI 1 is about 3 times of ROI 2. Under macroscopic shear deformation, the maximum tensile and compressive strains are almost equal in ROI 1 and ROI 2. And the difference of strain level at macro scale and micro scale is consistent in ROI 1 and ROI 2. ROI 3 has the highest maximum strain level, which might result from the stress concentration at the implant bottom.

Table 5-3 Maximum strain values of collagen fibers of the maximum principal strain and minimum principal strain

Loading condition 1		
	ε_{1max}	ε_{3max}
ROI 1	2.19%	-2.17%
ROI 2	0.80%	-0.80%
ROI 3	2.46%	-2.92%
Loading condition 2		
	ε_{1max}	ε_{3max}
ROI 1	1.61%	-1.62%
ROI 2	0.69%	-0.76%
ROI 3	1.90%	-2.50%

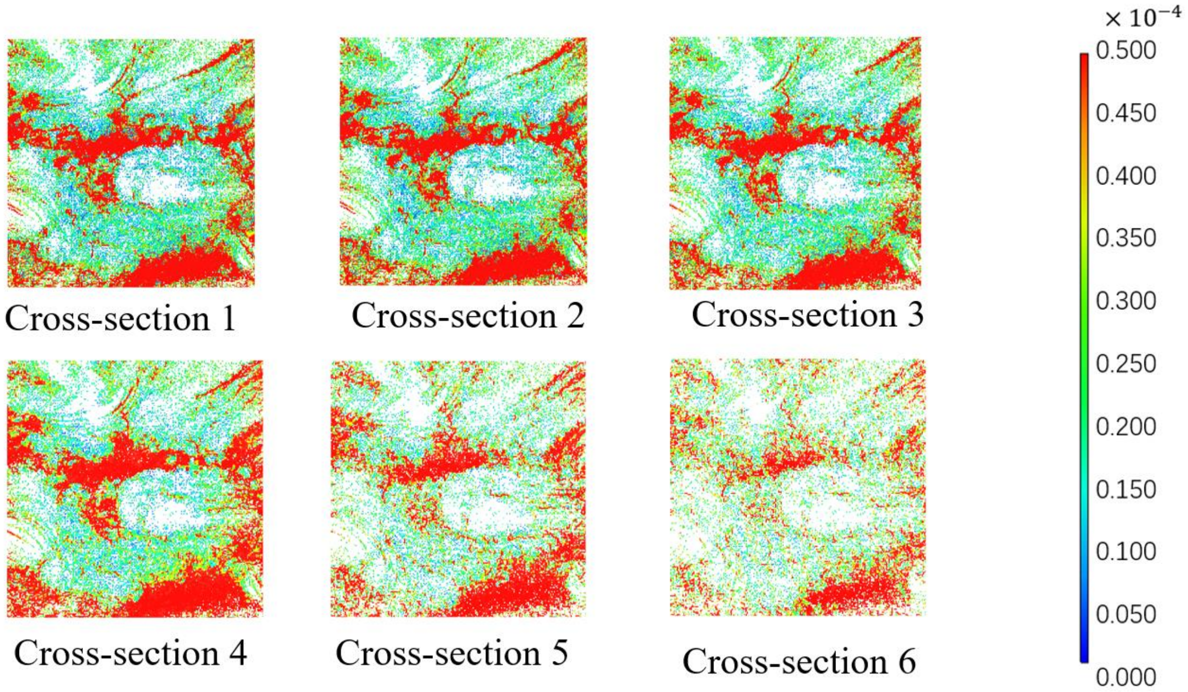
Cross-section 1 Cross-section 2 Cross-section 3

Cross-section 4 Cross-section 5 Cross-section 6

Figure 5.10 Cross-section view of Mises strain of collagen fibers of ROI 1 under loading condition 1. Interval of cross-section: 0.009mm

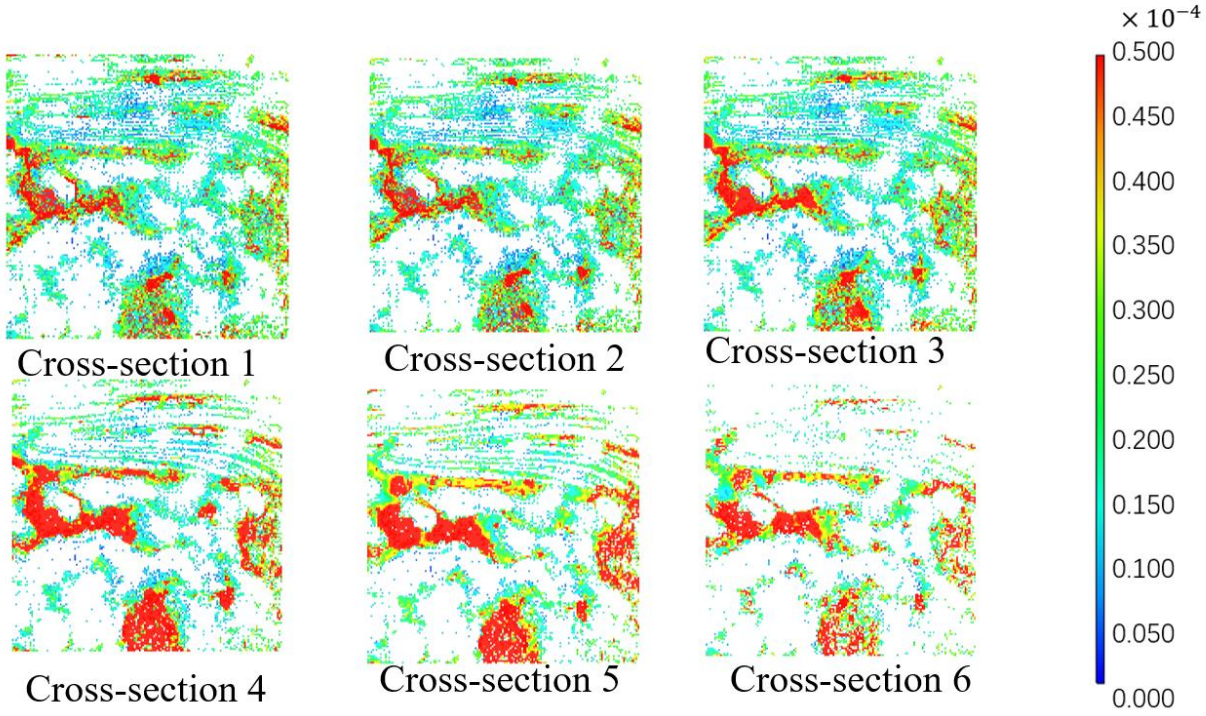
Cross-section 1 Cross-section 2 Cross-section 3

Cross-section 4 Cross-section 5 Cross-section 6

Figure 5.11 Cross-section view of Mises strain of collagen fibers of ROI 2 under loading condition 1. Interval of cross-section: 0.012mm

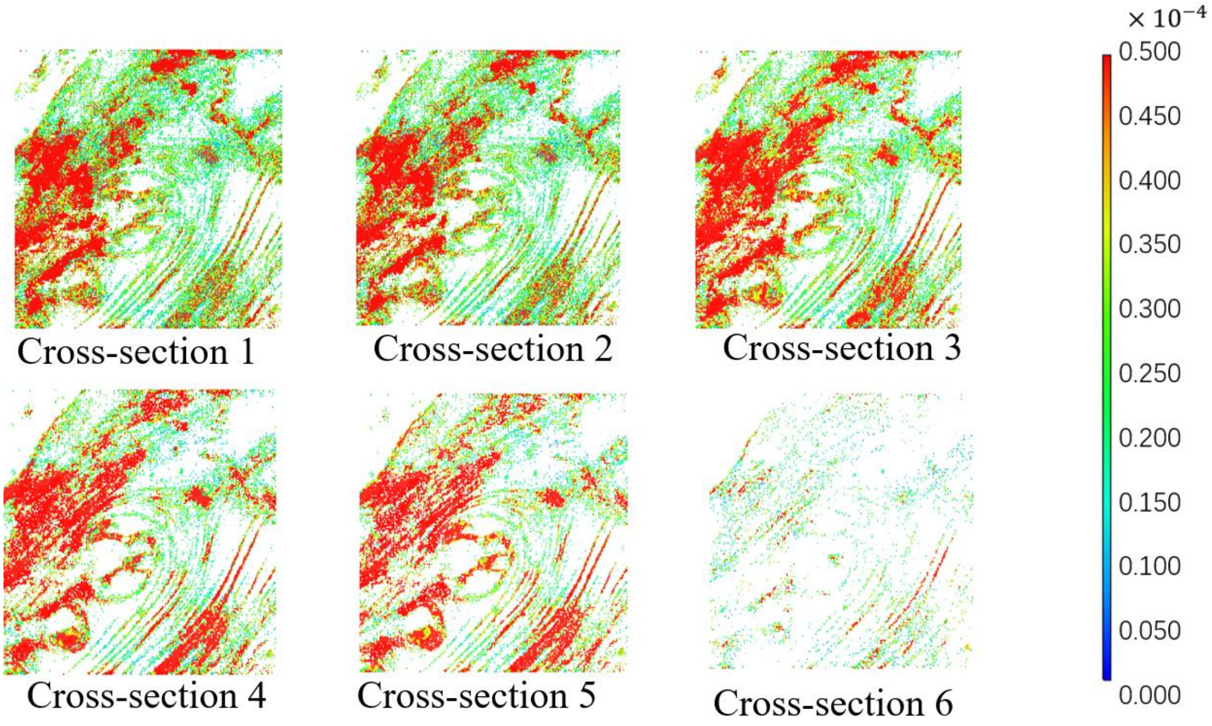

Figure 5.12 Cross-section view of Mises strain of collagen fibers of ROI 1 under loading condition 2. Interval of cross-section: 0.015mm

The maximum strain values are collected in Table 5-4. The maximum strain values of bone are about 50 times to 120 times smaller than the collagen fibers. The ROI 3 has the largest maximum strain values in both collagen fibers and bone under both loading conditions, which might result from the strain concentration near the bottom region. And ROI 1 has the higher maximum strain values in both collagen fibers and bone under both loading conditions than ROI 2, which results from the higher strain level in the left region of the implant.

Table 5-4 Maximum strain values of collagen fibers and bone in the three ROIs under both loading conditions

Maximum values of strain of collagen fibers			**Maximum values of strain of bone**		
	Loading condition 1	Loading condition 2		Loading condition 1	Loading condition 2
ROI 1	1.26%	0.91%	ROI 1	0.01%	0.01%
ROI 2	0.48%	0.39%	ROI 2	0.01%	0.01%
ROI 3	1.58%	1.31%	ROI 3	0.03%	0.03%

The strain direction of collagen fibers is also studied. The histogram of the angle between strain direction of collagen fibers and implant axis of the three ROIs under both loading conditions are shown in Figure 5.13, Figure 5.14, Figure 5.15 and Figure 5.16. In all the cases, the angle between strain directions and implant axis are mainly in the range from 63^0 to 117^0. Less than 10% of the fiber strain direction is in the implant axis direction. More than 50% of the fiber strain direction is close to be vertical to the implant axis in all the three ROIs under both loading conditions except the maximum principal strain of ROI 1 under loading condition 1.

The average difference factor is defined as Δ_{strain} to identify the amount of change in the histogram after changing the loading condition:

$$\Delta_{strain}=\frac{1}{n}\sum_{i}^{n}\frac{\left|P_{1,i}-P_{2,i}\right|}{\max\left(P_{1,i},P_{2,i}\right)} \tag{6.1}$$

where n is the number of ranges in the histogram. $P_{1,i}$ and $P_{2,i}$ are the percentages of ith range under loading condition 1 and loading condition 2.

The average difference factors of the maximum principal strain and minimum principal strain of the three ROIs are summarized in Table 5-5. The change of loading direction causes little change to the histogram of ROI 3 in both maximum principal strain and minimum principal strain. However, for ROI 2, the effect of changing loading condition on the minimum principal histogram is as small as the ROI 3 and relatively larger on the maximum principal strain. The strain directions of both maximum principal strain and minimum principal strain of ROI 1 are affected most significantly, which includes 50% of change in the maximum principal strain and 20% of change in the minimum principal strain. More specifically, for the maximum principal strain directions of fibers in the ROI 1, an increase of 30% is observed after changing loading directions.

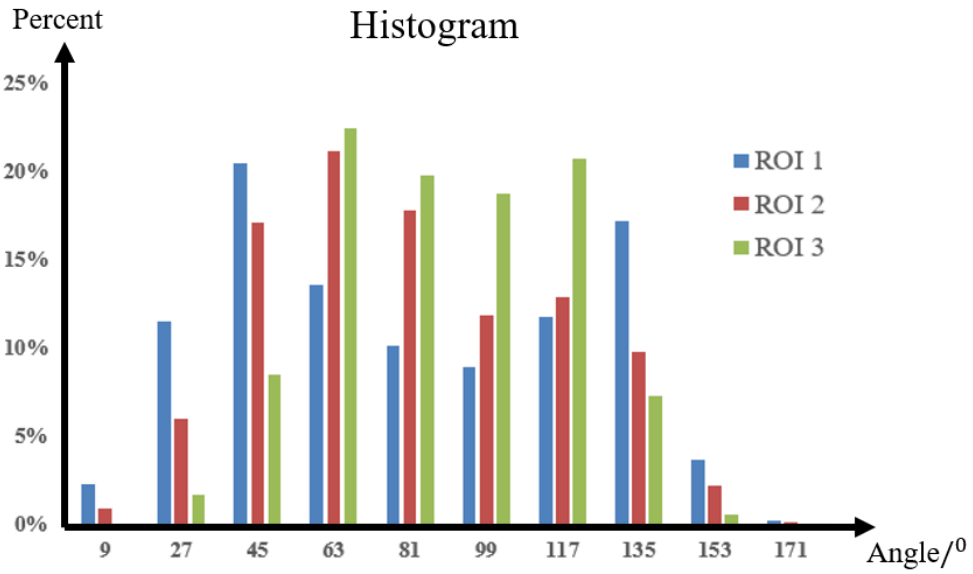

Figure 5.13 Histogram of the angle between the maximum principal strain direction of collagen fibers and implant axis direction (downward) under loading condition 1

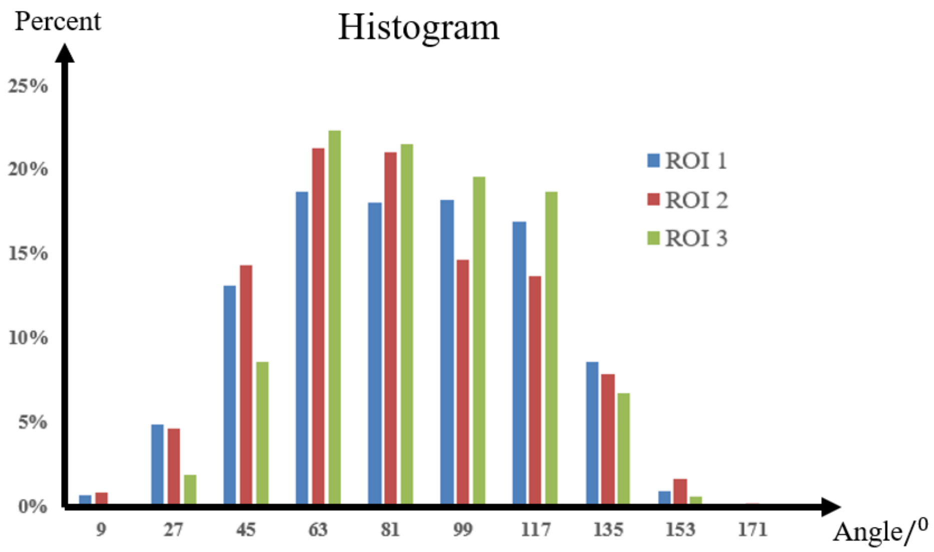

Figure 5.14 Histogram of the angle between the maximum principal strain direction of collagen fibers and implant axis direction (downward) under loading condition 2

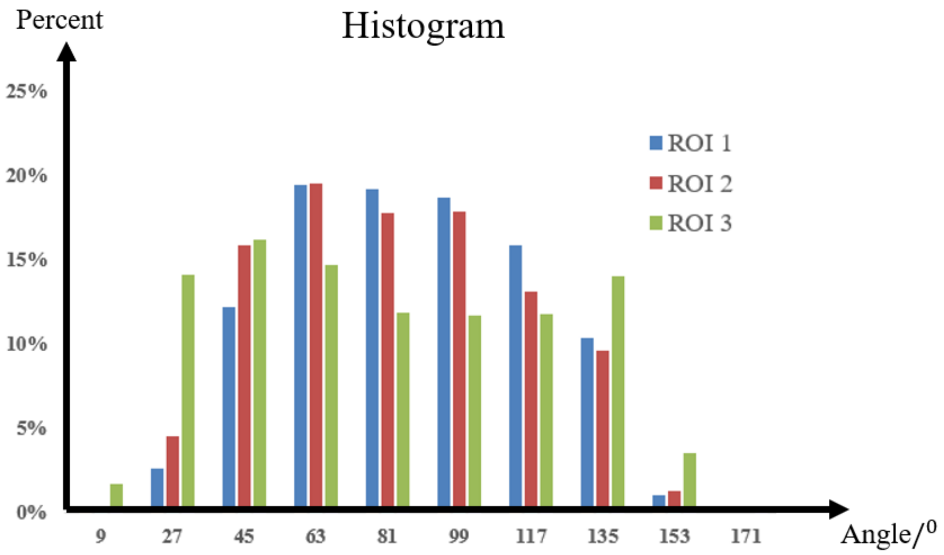

Figure 5.15 Histogram of the angle between the minimum principal strain direction of collagen fibers and implant axis direction (downward) under loading condition 1

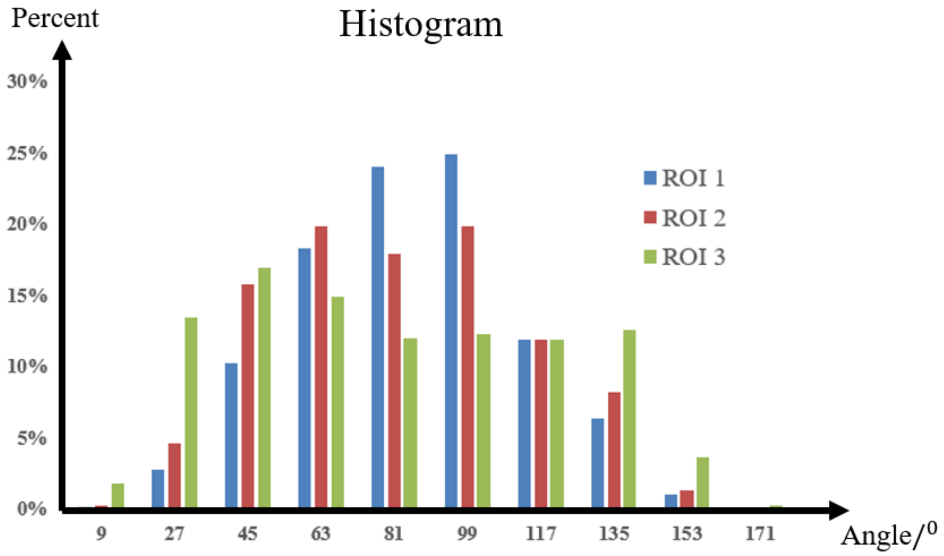

Figure 5.16 Histogram of the angle between the minimum principal strain direction of collagen fibers and implant axis direction (downward) under loading condition 2

Table 5-5 average difference factor of the three ROIs

	Maximum principal strain	Minimum principal strain
ROI 1	52%	20%
ROI 2	15%	7%
ROI 3	6%	6%

6 Discussion

6.1 Mesoscopic model

The mesoscopic is created to bridge the large gap between the resolution of SHG image and micro-CT images. It’s created based on the same micro-CT images as the macroscopic model however meshed with elements whose mesh size is 10 times smaller than the macroscopic model. Besides, to maintain the continuity of problem setting between the mesoscopic model and microscopic model, collagen fibers are filled in the mesoscopic model. Despite the difference in the problem setting, the comparison of the mesoscopic model and macroscopic model is straightforward to check the accuracy of the downscaling analysis when the scaling ratio is 10.

First of all, the structure information is lost in the macroscopic model. The image resolution of micro-CT image is $0.09 \times 0.09 \times 0.05\mathrm{mm}$ meanwhile the mesh size of the voxel element in the macroscopic model is $0.09 \times 0.09 \times 0.09\mathrm{mm}$ considering numerical errors and computational cost. Since the image resolution in the plane direction is the same as the macroscopic mesh size, the information is complete in the plane direction. The image information in the image-stacking direction is lost because the mesh size in the this direction is 1.8 times larger than the resolution. However, the mesh size of mesoscopic model is $0.009 \times 0.009 \times 0.009\mathrm{mm}$. In the image stacking direction, the resolution is more than 5 times larger than the mesoscopic mesh size so that in the ROI, the image information in the image-stacking direction is partially (completely when the mesh size can be divided evenly by the resolution) recovered. So in the mesoscopic model, more structural information is available. An example of comparison of mesoscopic mesh and macroscopic mesh is shown in Figure 6.1, where z direction is the image-stacking direction. The structural difference in the circled region is very obvious and more structural details are observed in the bone part of mesoscopic mesh.

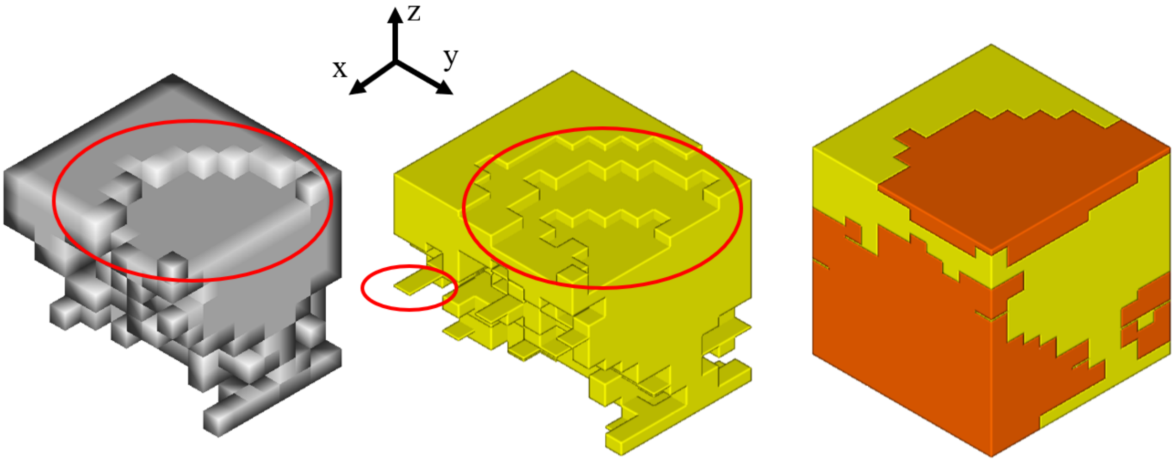

(a) Macroscopic mesh

(b) Bone part of mesoscopic mesh

(c) Complete mesoscopic mesh
Yellow: bone
Orange: collagen fibers

Figure 6.1 Mesh comparison of macroscopic mesh and mesoscopic mesh of ROI 3

The comparison of displacement between the macroscopic model and mesoscopic model can be used to ensure the correct set-up of boundary condition. Also the deformation mode of macroscopic model should match the mesoscopic model. The deformation of the bone in the macroscopic model and mesoscopic model are shown in Figure 6.2, Figure 6.3 and Figure 6.4. By observing the deformation shape, the deformation of macroscopic meshes matches the mesoscopic mesh, which is another proof of the correct set-up of boundary condition in the mesoscopic models of the three ROIs. Also, the deformation of ROI 1 is larger than ROI 2, which results from the larger strain level in the left region of implant analysed in 5.1.

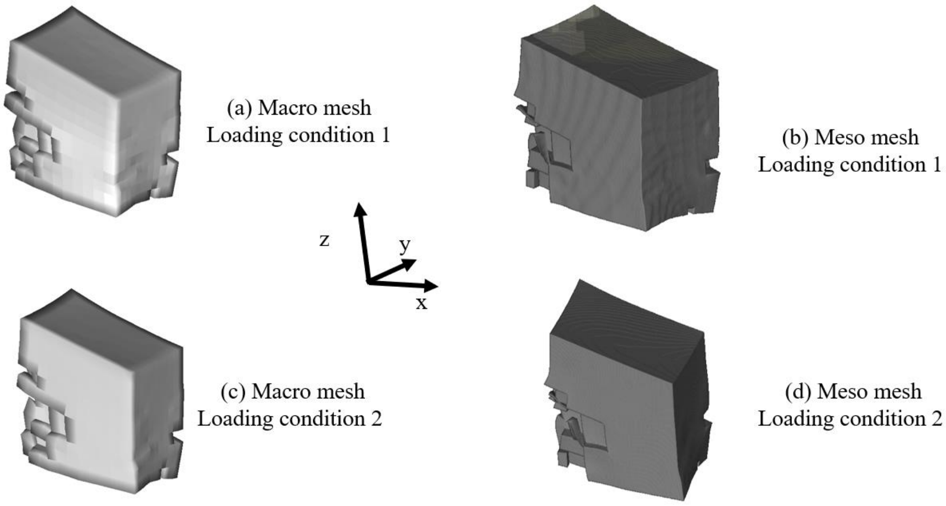

Figure 6.2 Deformation of macroscopic mesh and mesoscopic mesh of ROI 1 under both loading conditions

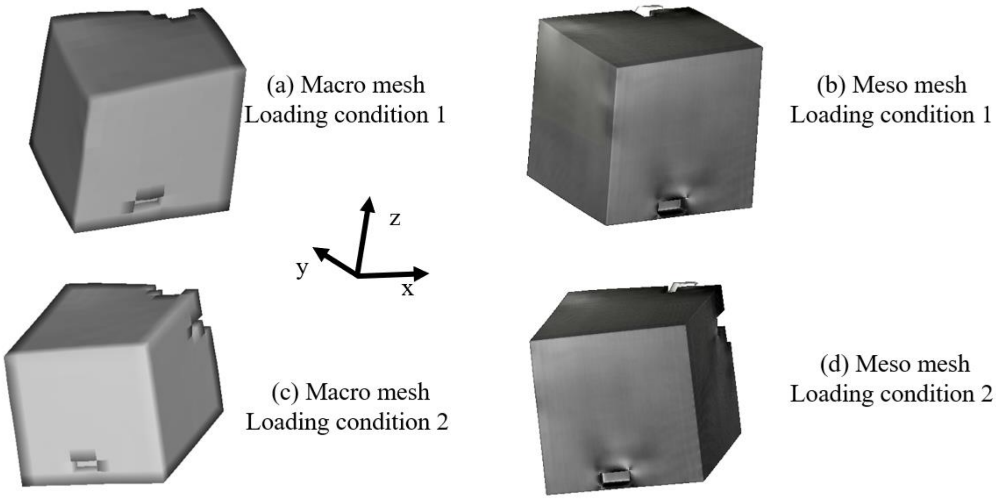

Figure 6.3 Deformation of macroscopic mesh and mesoscopic mesh of ROI 2 under both loading conditions

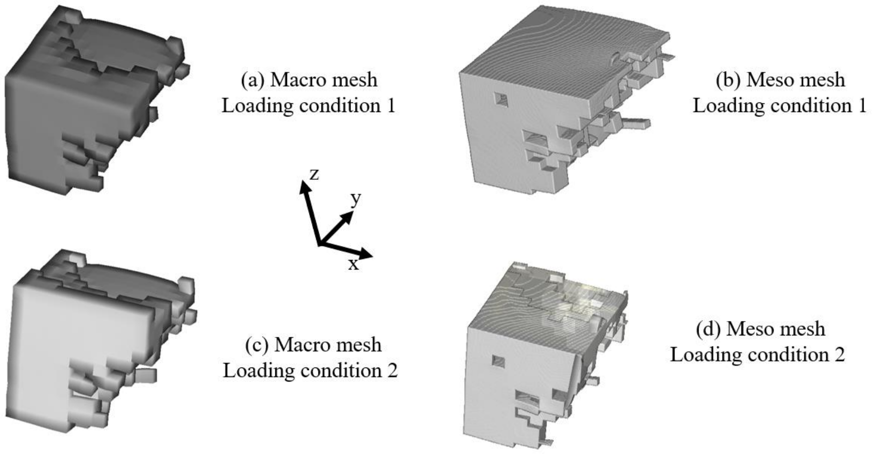

Figure 6.4 Deformation of the bone in the macroscopic mesh and mesoscopic mesh of ROI 3 under both loading conditions

To explore the specific deformation of the three ROIs, the histograms of the ratio between maximum principle strain and minimum principle strain in the mesoscopic models are plotted in Figure 6.5. When the ratio is between 0.7 and 1.3, the maximum principal strain is considered to be close to the minimum principal strain and the region is likely to be dominated by the shear stress. And when the ratio is smaller than 0.7, the compression dominates the region and if the ratio is larger than 1.3, the tension is considered to dominate the region. According to the histogram, All the three ROIs are dominated by the shear and compression mode under both boundary conditions, among which ROI 3 has the largest region under compression under both loading conditions and ROI 2 has the largest region under shear mode.

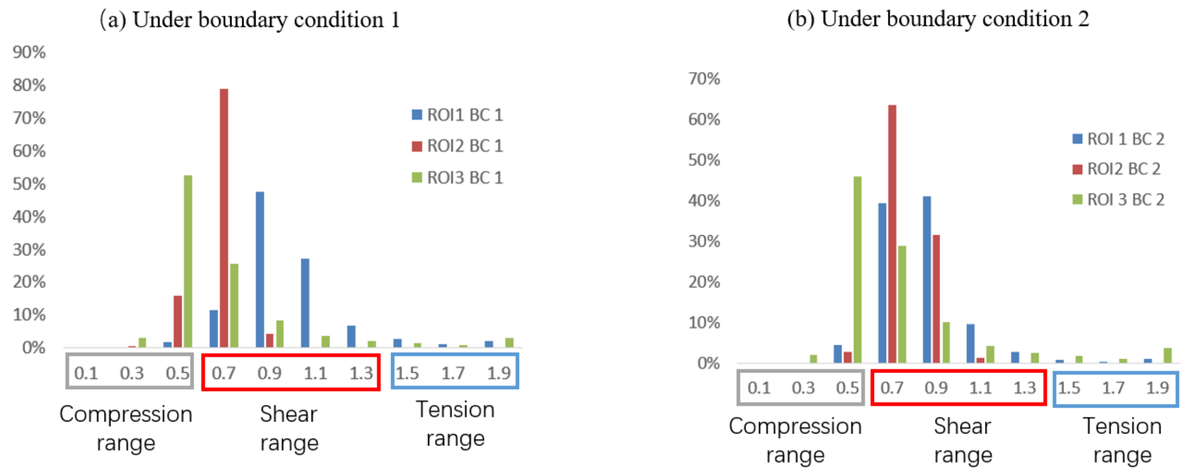

Figure 6.5 The histograms of the ratio between maximum principal strain and minimum principal strain in the mesoscopic model under both loading conditions

The strain distribution of the bone in the macroscopic mesh and mesoscopic mesh are also compared in Figure 6.6, Figure 6.7. The collagen fibers are hidden to show the complete view of the bone in the mesoscopic model. As it can be observed, in most regions, the macroscopic strain or stress have the similar distribution to the mesoscopic model even if the mesoscopic models have a smoother distribution. Also, stress and strain concentration can be observed in the mesoscopic model in the interface regions of bone and collagen fibers, in which no stress and strain concentration in the macroscopic model are observed in some cases. This indicates that the mesoscopic model can provide more information about the stress and strain distribution than the macroscopic model.

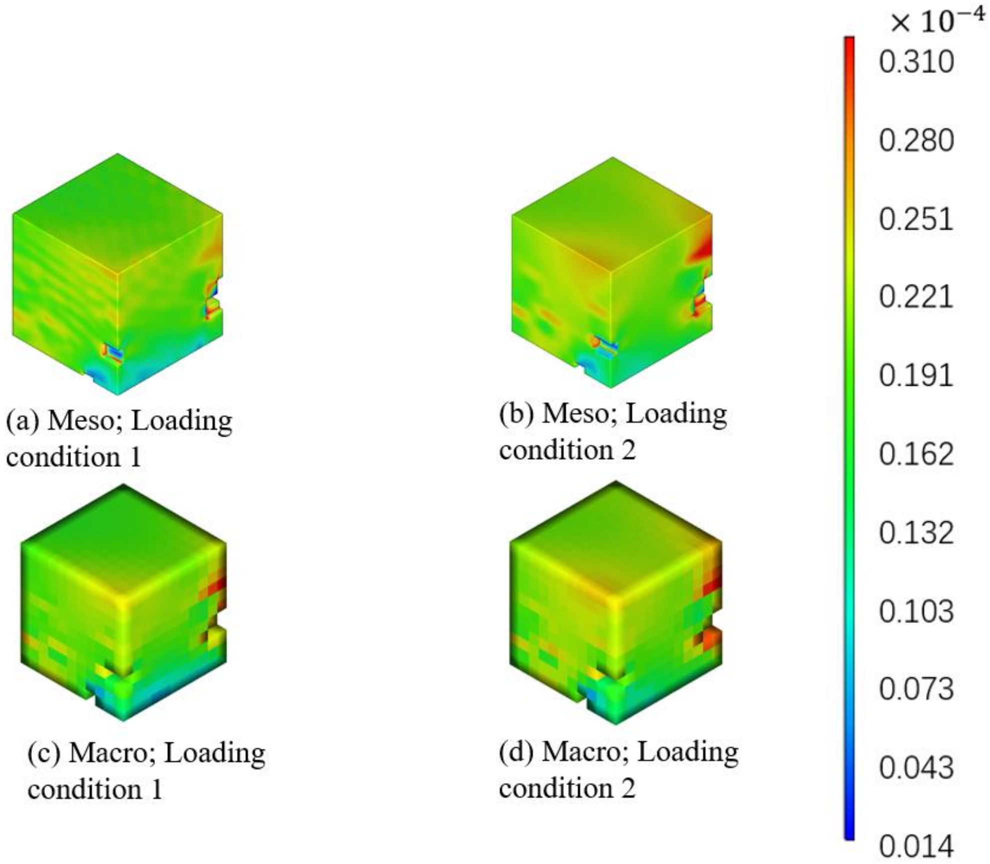

(a) Meso; Loading condition 1

(b) Meso; Loading condition 2

(c) Macro; Loading condition 1

(d) Macro; Loading condition 2

Figure 6.6 Von Mises strain of the bone in the macroscopic mesh and mesoscopic mesh of ROI 1 under both loading conditions

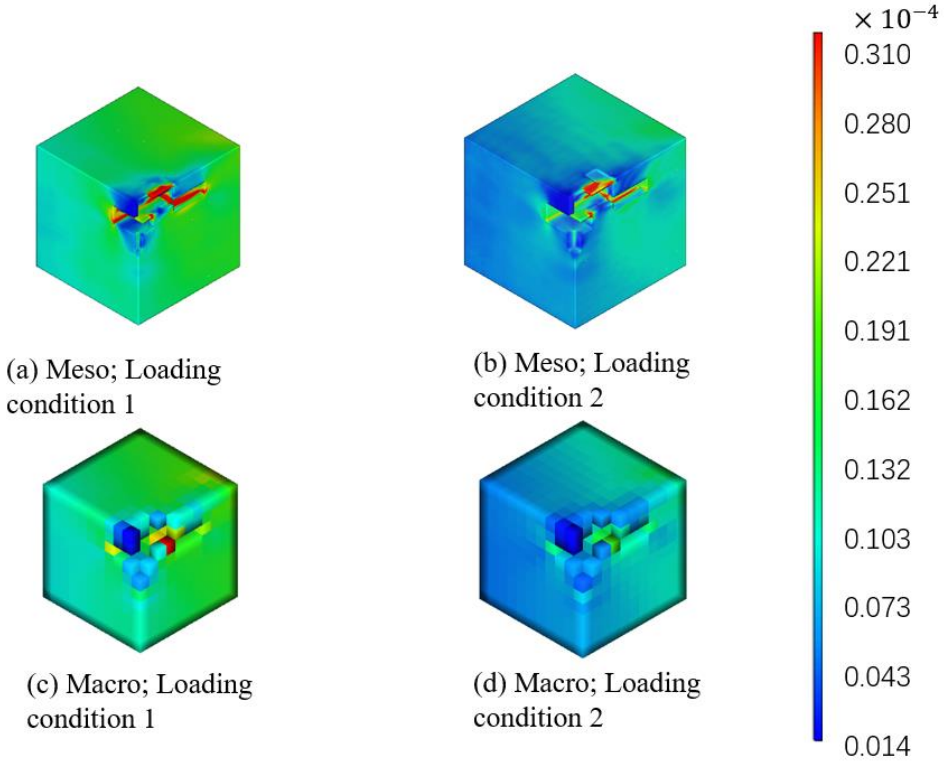

(a) Meso; Loading condition 1

(b) Meso; Loading condition 2

(c) Macro; Loading condition 1

(d) Macro; Loading condition 2

Figure 6.7 Von Mises strain of the bone in the macroscopic mesh and mesoscopic mesh of ROI 2 under both loading conditions

In short, the mesoscopic provides with more information about bone structure and strain distribution than macroscopic model, which allows us to bridge the large gap in the image resolution between the macroscopic model and microscopic model.

6.2 *Results of geometrical nonlinear analysis*

The loading curve of the geometrical nonlinear model is plotted in Figure 6.8. When the strain is below 0.2%, the difference of linear analysis and geometrical nonlinear analysis is less than 1%, which allows us to ignore the geotrical nonlinear effect.

And according to Table 5-4, in the microscopic models, the maximum values of collagen fibers of the three ROIs are all exceeding 0.2%. However, the volume of the three ROIs, whose maximum strain values exceeds 0.2%, are very small. Less than 1% of the strain values of collagen fibers exceeds 0.2% and the strain of more than 99% microscopic region is less than 0.2%. So to simplify the problem setting, geomtrical nonlinear effect is reasonable to neglect in the microscopic model.

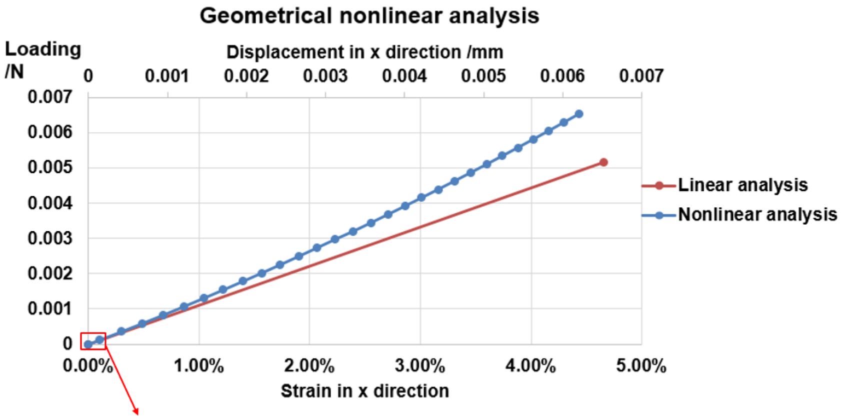

99% of the microscopic region
Difference of linear and nonlinear analysis: <1%

Figure 6.8 The loading curve of geometrical nonlinear model

6.3 *Result of verification example*

The stress concentration factors of the analytical solution, two macro models and the micro model at the stress concentration point are compared in Table 6-1. Also the numbers of elements in the three models are shown.

It can be observed that the macro model 1 has the smallest number of elements with lowest accuracy. The error of macro model 2 is reduced to 7.3 % however the number of elements is 1,000 times of macro model 1. For the micro model, the error is reduced to 12.7 % compared with macro model 1 and the number of mesh is about 1/60 of macro model 2. Also, the relative error between micro model and macro model

2 is about 6.5%, which results from the error of interpolation. But still the errors of all the three models are more than 7%, which is caused by the zig-zag meshing (Figure 6.9). The edge of the circle can’t be accurately described by the voxel elements.

Conclusion can be drawn that the downscaling method implemented in VOXELCON can improve the numerical accuracy and reduce computational cost to some extent. And the errors caused by the zig-zag mesh is inevitable.

Table 6-1 Comparison of stress concentration factor and number of elements

	Analytical solution	Macro model 1	Macro model 2	Micro model
Stress concentration factor	3	2.34	2.78	2.62
Number of elements	/	4,980	4,980,000	80,350
Errors: $\left\lvert\frac{\varepsilon_{FEM} - \varepsilon_{analytical}}{\varepsilon_{analytical}}\right\rvert$	/	22%	7.3%	12.7%

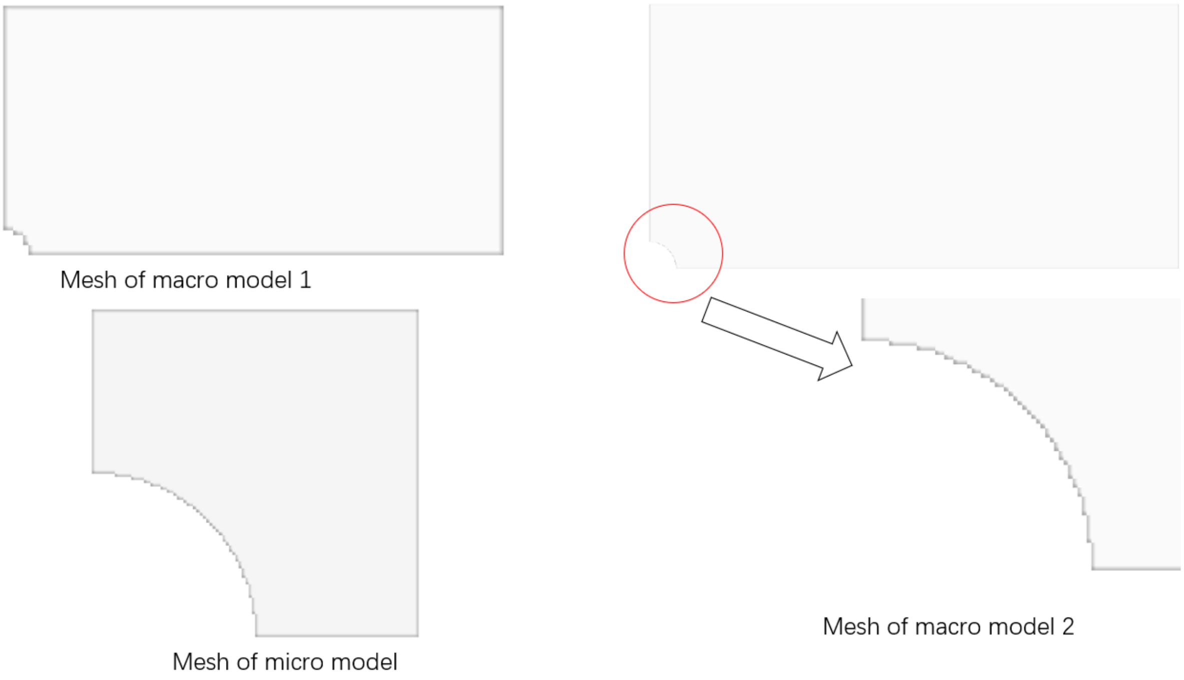

Mesh of macro model 1

Mesh of micro model

Mesh of macro model 2

Figure 6.9 Zig-zag mesh created by VOXELCON

7 Conclusion

This study is so far the first attempt to create a FEM model by combining both micro-CT images and SHG images to study the strain distribution of collagen fibers.

First of all, a system of three-scale analysis has been developed by the author to connect the micro-CT images and stitched SHG images. The models in three scales include macroscopic model, mesoscopic model and microscopic model. The macroscopic model is based on the micro-CT images, which includes the mandible and dental implant meanwhile the mesoscopic is a ROI from the bone part of macroscopic model, which is also based on the micro-CT images. The microscopic model is a ROI from the mesoscopic model and it includes the bone and collagen fibers, which is based on the stitched SHG images. Two types of angled prescribed displacement are used as loading conditions in macroscopic model. Interpolated displacements obtained from the macroscopic model and mesoscopic model are used for the boundary conditions of mesoscopic model and microscopic model. The interpolation, setup of boundary conditions for mesoscopic model and microscopic one and mesh generation based on the images are achieved automatically by the system written by python code.

The macroscopic results indicate that, under both loading conditions, in the left half bone region near the dental implant, the strain level is higher than the right region. Also, strain concentration can be observed in the region near the lingual side and implant’s bottom. Besides, under angled loading, the area of strain concentration is larger than the axial loading in the left bone region of dental implant. For the mechanical environment of the three ROIs, the loading conditions don’t change much the mechanical environment of ROI 1 and ROI 2 but the tension direction of ROI 3 is changed. ROI 1 and ROI 2 are under shear stress under both loading conditions and ROI 3 is under compression under both loading conditions. This matches previous study [19].

Meanwhile, the microscopic results indicate that, the overall strain levels of collagen fibers are higher than the bone. And in all the three ROIs, higher strain could be observed mainly in the collagen rich region. And in the fibrous region, the strain level is relatively lower than collagen rich region. And in the bottom region, the strain concentration occurs and ROI 3 has the highest maximum strain. For the fibrous region, the compression direction is almost parallel to fiber orientation in ROI 3. However the connection between fiber orientation and loading direction is not clearly observed in ROI 1 and ROI 2 under both loading conditions. For the collagen rich region, it has the isotropic mechanical properties because the collagen fibers are randomly distributed. Under macroscopic shear deformation, the maximum tensile and compressive strains are almost equal in ROI 1 and ROI 2. For ROI 3, the strain value is dependent on both macroscopic mechanical environment and microscopic morphology.

Moreover, the mesoscopic model provides with more information about bone structure and more smooth strain distribution than macroscopic model, which allows us to bridge the large gap in the image resolution between the micro-CT images and SHG images.

Finally, from the geometrical nonlinear analysis, the fiber volume fractions in the microscopic models whose strain exceed 0.2% is less than 1%. This allows us to neglect the neglect the geometrical nonlinear effect.

8 Future works

So far the computational method has been developed however there are still some limitations. The plan about the future works along with the limitations are concluded:

First of all, only two types of Dirichlet boundary conditions are imposed to the macroscopic model. The connection between the macroscopic loading condition and strain distribution of collagen fibers is still not clear. In the future, more angled prescribed displacement will be imposed to the macroscopic model and the strain distribution of microscopic model will be observed to explore the correlation. The collagen fibers distribution is not studied quantitatively, which requires image processing techniques. Some parameters such as fiber length, fiber orientation and fiber straightness have to be measured in the SHG images to make further comparison.

Secondly, only three typical ROIs near the dental implant are analyzed. The difference of strain distribution between ROIs is not clearly known. The database of microscopic results should be increased to obtain the understanding in the strain distribution of microscopic model. So the number of ROIs has to be increased.

Moreover, the strain values of fibers are computed but the validation is difficult to be achieved. There are several reasons. First of all, the specimen of collagen fibers are cut into thin slices for the imaging purpose. For the fibrous region, it’s possible to extract a single fiber and set up an experiment to measure the strain under uniaxial loading. But the material properties of collagen rich region is isotropic according to the dentists and the measurement of the strain in the collagen rich region is not available so far. So in the future, the validation of the measurement of the strain in the collagen rich region should be proposed.

In this study, the anisotropic mechanical properties of collagen fibers in the fibrous region are neglected and they are modelled as isotropic material. But in reality, the collagen fibers are close to transversely isotropic material, whose stiffness is large in the fiber axial direction and relatively smaller in the cross-section plane. In the future, the fiber anisotropy will be considered in the modelling. The fiber orientation will be measured in the fibrous region and anisotropic material model will be assigned to individual fibers.

The thickness of the specimen is 150$\mu\mathrm{m}$, which is small and all the ROIs are in the plate shape. In the future, a thicker specimen will be cut for imaging to obtain a ROI with larger thickness. And the resolution in the image stacking direction is 20$\mu\mathrm{m}$, which is much lower than the plane direction. Unsmooth structure might be caused and in the future the resolution in the image stacking direction will be improved.

To maintain the continuity of problem setting between the mesoscopic model and microscopic model, all the cavity in the mesoscopic model is filled with collagen fibers. However, the accuracy of this problem setting hasn’t been checked and in the future, verification will be made to confirm this problem setting.

Finally, in the image binarization process, only one color channel is considered, which results in the inaccurate structure of fibrous region. More specifically, all the black region is modelled as bone, which in reality might includes other material, such as non-fiber material, osteocytes etc. In the future, more color channel will be considered in the binarization to increase the accuracy of modelled structure.

References

[1] Brånemark, P. I., Chien, S., Gröndahl, H. G., & Robinson, K. (2005). *The osseointegration book: from calvarium to calcaneus* (pp. 24). Berlin: Quintessence.

[2] Chakravorty, N., Jaiprakash, A., Ivanovski, S., & Xiao, Y. (2017). Implant Surface Modifications and Osseointegration. *Biomaterials for Implants and Scaffolds* (pp. 107-131). Springer, Berlin, Heidelberg.

[3] Herbert F. Wolf; Klaus H. Rateitschak (2005). *Color atlas of dental medicine. Periodontology* (pp. 12). New York: Thieme Medical.

[4] Weiner, S., & Wagner, H. D. (1998). The material bone: structure-mechanical function relations. *Annual Review of Materials Science*, 28(1), 271-298.

[5] Rho, J. Y., Kuhn-Spearing, L., & Zioupos, P. (1998). Mechanical properties and the hierarchical structure of bone. *Medical engineering and physics*, 20(2), 92-102.

[6] Albrektsson, T., Brånemark, P. I., Hansson, H. A., & Lindström, J. (1981). Osseointegrated titanium implants: requirements for ensuring a long-lasting, direct bone-to-implant anchorage in man. *Acta Orthopaedica Scandinavica*, 52(2), 155-170.

[7] Traini, T., Degidi, M., Strocchi, R., Caputi, S., & Piattelli, A. (2005). Collagen fiber orientation near dental implants in human bone: do their organization reflect differences in loading?. *Journal of Biomedical Materials Research part B: Applied Biomaterials*, 74(1), 538-546.

[8] Tetè, S., Mastrangelo, F., Bianchi, A., Zizzari, V., & Scarano, A. (2009). Collagen fiber orientation around machined titanium and zirconia dental implant necks: an animal study. *The International journal of oral & maxillofacial implants*, 24(1), 52.

[9] Sasaki, N., Shirakawa, H., Nozoe, T., & Furusawa, K. (2013). Elastic properties of collagen in bone determined by measuring the Debye–Waller factor. *Journal of biomechanics*, 46(16), 2824-2830.

[10] Vercher-Martínez, A., Giner, E., Belda, R., Aigoun, A., & Fuenmayor, F. J. (2018). Explicit expressions for the estimation of the elastic constants of lamellar bone as a function of the volumetric mineral content using a multi-scale approach. *Biomechanics and modeling in mechanobiology*, 17(2), 449-464.

[11] Zoumi, A., Yeh, A., & Tromberg, B. J. (2002). Imaging cells and extracellular matrix in vivo by using second-harmonic generation and two-photon excited fluorescence. *Proceedings of the National Academy of Sciences*, 99(17), 11014-11019.

[12] Campagnola, P. J., & Dong, C. Y. (2011). Second harmonic generation microscopy: principles and applications to disease diagnosis. *Laser & Photonics Reviews*, 5(1), 13-26.

[13] Campagnola, P. J., Millard, A. C., Terasaki, M., Hoppe, P. E., Malone, C. J., & Mohler, W. A. (2002). Three-dimensional high-resolution second-harmonic generation

imaging of endogenous structural proteins in biological tissues. *Biophysical journal*, 82(1), 493-508.

[14] Strupler, M., Pena, A. M., Hernest, M., Tharaux, P. L., Martin, J. L., Beaurepaire, E., & Schanne-Klein, M. C. (2007). Second harmonic imaging and scoring of collagen in fibrotic tissues. *Optics express*, 15(7), 4054-4065.

[15] Chen, G., Chen, J., Zhuo, S., Xiong, S., Zeng, H., Jiang, X., Xie, S. (2009). Nonlinear spectral imaging of human hypertrophic scar based on two‐photon excited fluorescence and second ‐ harmonic generation. British Journal of Dermatology, 161(1), 48-55.

[16] Doras, C., Taupier, G., Barsella, A., Mager, L., Boeglin, A., Bulou, H., & Dorkenoo, K. D. (2011). Polarization state studies in second harmonic generation signals to trace atherosclerosis lesions. *Optics express*, 19(16), 15062-15068.

[17] Han, M., Giese, G., & Bille, J. F. (2005). Second harmonic generation imaging of collagen fibrils in cornea and sclera. *Optics express*, 13(15), 5791-5797.

[18] Matsunaga, S., Koresawa, K., Okudera, H., Suzuki, M., Yoshinari, M., Yajima, Y., Abe, S., (2018), Micro/nano structural characteristics of newborn compact bone surrounding impact, 48th Conf. *Japanese Society of Oral Implantology*, Osaka.

[19] Matsunaga, S., Shirakura, Y., Ohashi, T., Nakahara, K., Tamatsu, Y., Takano, N., Ide, Y. (2010). Biomechanical role of peri-implant cancellous bone architecture. *International Journal of Prosthodontics*, 23(4).

[20] Ohashi, T., Matsunaga, S., Nakahara, K., Abe, S., Ide, Y., Tamatsu, Y., Takano, N. (2010). Biomechanical role of peri-implant trabecular structures during vertical loading. *Clinical oral investigations*, 14(5), 507-513.

[21] Guedes, J., & Kikuchi, N. (1990). Preprocessing and postprocessing for materials based on the homogenization method with adaptive finite element methods. *Computer methods in applied mechanics and engineering*, 83(2), 143-198.

[22] Takano, N., Zako, M., & Ishizono, M. (2000). Multi-scale computational method for elastic bodies with global and local heterogeneity. *Journal of computer-aided materials design*, 7(2), 111.

[23] Yoshiwara, Y., Clanche, M., Basaruddin, K. S., Takano, N., & Nakano, T. (2011). Numerical study on the morphology and mechanical role of healthy and osteoporotic vertebral trabecular bone. *Journal of Biomechanical Science and Engineering*, 6(4), 270-285.

[24] Nakano, H., Takano, N., & Maki, K. (2016). Desktop micro-CT image-based dynamic FEM analysis of stress wave pathways between mandibular trabecular bone and cortical bone with comparisons to virtual models with eliminated materials on pathways. *Journal of Biomechanical Science and Engineering*, 11(3), 16-00313.

[25] Dutra, T. A., Ferreira, R. T. L., Resende, H. B., & Guimarães, A. (2019). Mechanical characterization and asymptotic homogenization of 3D-printed continuous carbon fiber-reinforced thermoplastic. *Journal of the Brazilian Society of Mechanical Sciences and Engineering*, 41(3), 133.

[26] Takano, N., Zako, M., & Okazaki, T. (2001). Efficient modeling of microscopic heterogeneity and local crack in composite materials by finite element mesh superposition method. *JSME International Journal Series A Solid Mechanics and Material Engineering*, 44(4), 602-609.

[27] Tsukino, M., Takano, N., Michel, A., & HAÏAT, G. (2015). Multiscale stress analysis of trabecular bone around acetabular cup implant by finite element mesh superposition method. *Mechanical Engineering Letters*, 1, 15-00354.

[28] Nakasumi, S., Suzuki, K., & Ohtsubo, H. (2008). Crack growth analysis using mesh superposition technique and X-FEM. *International journal for numerical methods in engineering*, 75(3), 291-304.

[29] Hirai, I., Wang, B. P., & Pilkey, W. D. (1984). An efficient zooming method for finite element analysis. *International Journal for Numerical Methods in Engineering*, 20(9), 1671-1683.

[30] Hirai, I., Uchiyama, Y., Mizuta, Y., & Pilkey, W. D. (1985). An exact zooming method. *Finite Elements in Analysis and Design*, 1(1), 61-69.

[31] Voleti, S. R., Chandra, N., & Miller, J. R. (1996). Global-local analysis of large-scale composite structures using finite element methods. *Computers & structures*, 58(3), 453-464.

[32] Tawara, D., Nagahata, M., Takano, N., Kinoshita, H., & Abe, S. (2015). Probabilistic analysis of mechanical behaviour of mandibular trabecular bone using a calibrated stochastic homogenization model. *Acta Mechanica*, 226(10), 3275-3287.

[33] Bou-Akl, T., Banglmaier, R., Miller, R., VandeVord, P. (2013). Effect of crosslinking on the mechanical properties of mineralized and non-mineralized collagen fibers. *Journal of Biomedical Materials Research Part A*, *101*(9), 2507-2514.

Bibliography

1 Orally present *Microscopic strain analysis in collagen fiber in peri-implant bone using micro-CT and stitched SHG images* in the Program of the 31 st Bioengineering Conference 2018 Annual Meeting of BED/ JSME. 14th December, 2018, Koriyama city, Japan.
2 Orally present *SHG image-based 3D finite element analysis of peri-implant mandibular bone considering collagen fiber* in the 6th International Conference on Computational and Mathematical Biomedical Engineering. 10th June, 2019, Sendai city, Japan